Transversity and Λ polarisation in polarised SIDIS

Andrea Moretti

Supervisor: Prof. Anna Martin

Co-Supervisor: Dott. Giulio Sbrizzai

Department of Physics
University of Trieste

Master Thesis

March 2017

Alla mia famiglia
e ai miei amici.

Abstract

Nell'ambito della Cromodinamica Quantistica, la descrizione al *leading order* della struttura del nucleone si basa sulle tre funzioni di distribuzione partoniche (PDFs) $f_1(x)$, $g_1(x)$ e $h_1(x)$. Da un punto di vista probabilistico, $f_1(x)$ è definita come la densità di quark che portano una frazione x del momento longitudinale del nucleone, mentre la distribuzione di elicità $g_1(x)$ è definita come la differenza delle densità di quark con polarizzazione parallela e antiparallela rispetto a quella del nucleone polarizzato e frazione x di momento. Entrambe queste distribuzioni sono ben note grazie alle misure di *deep inelastic scattering* (DIS) inclusivo non polarizzato e polarizzato longitudinalmente. La funzione di distribuzione $h_1(x)$, nota come trasversità, è l'analogo dell'elicità nel caso di un nucleone con polarizzazione trasversa: è definita come la densità di quark con polarizzazione parallela a quella del nucleone meno la densità di quark con polarizzazione antiparallela. La trasversità, non meno importante delle distribuzioni $f_1(x)$ e $g_1(x)$, è tuttavia meno conosciuta a causa della sua natura *chiral-odd* che non ne consente l'osservazione nel DIS inclusivo. Una possibilità per accedere alla trasversità è offerta dal meccanismo di trasferimento di spin che induce una polarizzazione trasversa negli iperoni Λ e $\bar{\Lambda}$ prodotti nel DIS su nucleoni polarizzati trasversalmente. Qui, le funzioni di frammentazione $H_1^{\Lambda/q}$ e $H_1^{\bar{\Lambda}/q}$, molto interessanti ma ancora non note, costituiscono le quantità *chiral-odd* che si legano alla trasversità per ristabilire la conservazione dell'elicità. Sfruttando il decadimento *self-analysing* delle Λ, la polarizzazione trasmessa può essere misurata dall'asimmetria angolare del barione di decadimento. Dunque la misura della polarizzazione della Λ fornisce informazioni sulla trasversità h_1 e sul meccanismo di trasferimento di spin nella produzione di iperoni, descritto dalla funzione di frammentazione $H_1^{\Lambda/q}$.

Scopo di questo lavoro di tesi è la prima misura della polarizzazione trasmessa dalla trasversità a particelle Λ e $\bar{\Lambda}$ sfruttando il set completo di eventi DIS raccolti dall'esperimento COMPASS usando un fascio di muoni ad alta energia e un bersaglio di protoni polarizzati trasversalmente. Questa misura, mai condotta prima, può dare informazioni importanti sulla struttura adronica e sul meccanismo di frammentazione.

Questo elaborato è organizzato nel seguente modo. Il capitolo 1 è dedicato ad una breve descrizione teorica della struttura del nucleone, dei processi DIS e dei meccanismi di

produzione e decadimento di particelle Λ e $\bar{\Lambda}$. L'ultima sezione offre una panoramica delle più importanti misure di DIS legate alla trasversità. Nel capitolo 2 viene presentato l'esperimento COMPASS con particolare attenzione ai rivelatori utilizzati in questa analisi. La selezione degli eventi DIS e dei candidati Λ e $\bar{\Lambda}$ ed il metodo per la misura della polarizzazione sono descritti nel capitolo 3 e costituiscono il cuore del lavoro svolto. I risultati sono descritti nel capitolo 4, che contiene anche conclusioni e prospettive future.

Abstract

The basic ingredients of the leading order QCD description of the nucleon structure are the three parton distribution functions (PDFs) $f_1(x)$, $g_1(x)$ and $h_1(x)$. Focusing on quarks, $f_1(x)$ is defined as the number density of quarks carrying a fraction x of the longitudinal momentum of the nucleon, while the helicity distribution function $g_1(x)$ is defined as the helicity asymmetry of quarks in a longitudinally polarised nucleon. They are both quite well known thanks to the measurements of unpolarised lepton-nucleon inclusive deep inelastic scattering (DIS) and longitudinally polarised lepton-nucleon DIS.

The transversity distribution function $h_1(x)$ is the analogous of the helicity PDF in case of transversely polarised nucleons: it is defined as the number density of quarks with polarisation parallel to that of the nucleon minus the number density of quarks with antiparallel polarisation. Transversity is as fundamental as $f_1(x)$ and $g_1(x)$, but is less known because of its chiral-odd nature, which prevents to access it in inclusive DIS. A possible way to access transversity is offered by the spin transfer mechanism that leads to a *transversity transmitted* polarisation of Λs and $\bar{\Lambda}$s produced in DIS off transversely polarised nucleons. Here, the fragmentation functions $H_1^{\Lambda/q}$ and $H_1^{\bar{\Lambda}/q}$, very interesting and still unknown, are the chiral-odd objects coupled with the transversity distributions. Taking advantage of the Λs and $\bar{\Lambda}$s self-analysing decay, the transmitted polarisation can then be measured by the angular asymmetry of the decay baryon. Thus the measurement of Λ and $\bar{\Lambda}$ polarisation gives information on both h_1 and the spin transfer mechanism in the hyperon production encoded in $H_1^{\Lambda/q}$. The aim of this thesis work is the first measurement of the transversity transmitted polarisation of Λs and $\bar{\Lambda}$s using the complete DIS dataset collected by the COMPASS Collaboration using a high energy muon beam and a transversely polarised proton target. Such measurement, never performed before, will give relevant information on the hadron structure and the fragmentation mechanism.

This thesis is organised as follows. Chapter 1 is dedicated to a short theoretical description of the nucleon structure, the DIS process and the mechanisms of Λ ($\bar{\Lambda}$) production and decay. The last section gives an overview of the most relevant DIS measurements related to transversity. In chapter 2 the COMPASS experiment is described, giving more details on the detectors relevant for the present measurement. The selection of the events and of the Λ

and $\bar{\Lambda}$ candidates and the method used to measure their polarisation are described in chapter 3 and constitute the core of the work done. The results are described in chapter 4, which includes conclusions and outlook and ends this thesis.

Contents

Chapter 1

Nucleon spin structure and transversity

1.1 Introduction

The atomic nucleus is made of protons and neutrons, generally called *nucleons*. Nucleons are not elementary particles: they themselves have an internal structure whose building blocks are the *quarks*, which are fermions. The role of hadronic physics is to understand the structure of the nucleons as well as the spectrum of all strongly-interacting hadrons, which are also made up of quarks.

A large part of our understanding of the hadrons comes from the *Quark Parton Model* (QPM), which is formulated in terms of constituent quarks and provides, *inter alia*, a simplified but good description of the hadron spectrum and a prediction of the magnetic moments of the baryons. In the QPM the internal structure of a baryon (i.e. a half-integer spin hadron) consists of three constituent quark, each of them possessing a mass of approximately one third of the baryon mass. In this model, the proton consists of two u (up) quarks with charge +2/3 e and one d (down) quark with charge -1/3 e; the neutron, symmetrically, consists of two d quarks and one u quark. A meson (integer-spin hadron) is described as a $q\bar{q}$ pair. In the QPM, the three quarks are in an S-state; the u quark has spin 1/2 upwards, while the d quark has spin 1/2 downwards. A full description of the hadronic spectrum requires indeed four more quark flavors, namely the strange (s), the charm (c), the bottom (b) and the top (t) quarks.

Our knowledge of hadron structure also relies on the non-abelian gauge theory called *Quantum Chromodynamics* (QCD). In QCD, the quarks are described as fundamental, point-like particles with no inner structure, whose strong interactions take place through the exchange of vector bosons, the *gluons*. The perturbative approach used to solve the QCD equations cannot be applied at small energies, where the coupling constant is of order unity

and where, for this reason, the QPM remains a useful model. In this framework, the issue of the nucleon spin appears particularly interesting.

The nucleon is a spin 1/2 particle. This value can be decomposed into the sum of several contributions:

$$\frac{1}{2} = \frac{1}{2}\Delta\Sigma + \Delta g + L_q + L_g \tag{1.1}$$

where:

- $\Delta\Sigma$ is the total number of quarks with spin parallel to that of the nucleus minus the number of quarks with their spin anti-parallel;
- Δg is the gluon contribution;
- L_q and L_g are the contributions from the orbital momentum of quarks and gluons.

The simplest QPM prediction about the spin of the nucleon foresees a $\Delta\Sigma = 1$ contribution, with $\Delta g + L_q + L_g = 0$; including relativistic corrections $\Delta\Sigma \sim 0.75$, with $\Delta g \sim 0.125$ and $L_q = L_g = 0$. The result of the EMC experiment in 1988 on a proton target, $\Delta\Sigma = 0.12 \pm 0.09 \pm 0.14$ [1, 2] came as a big surprise, since it contradicted these predictions. The *proton spin crisis* caused by the EMC result urged further intense experimental and theoretical investigations on spin. On the experimental side, a large number of experiments were performed at SLAC, DESY, JLAB and CERN to verify the EMC result, measure the neutron and improve the accuracy of the measurements. In particular, the first experiments (SMC at CERN and E142, E143, E154 and E155 at SLAC, and HERMES at DESY) confirmed the EMC result that the quarks carry only a small (about 0.25) fraction of the proton spin, and found out that the same holds true for the neutron. These findings clearly hinted at the necessity of setting up new experiments to measure Δg and possibly L_q and L_g, experimental effort which is still ongoing (COMPASS at CERN, RHIC at BNL and several Jefferson Lab experiments).

On the theoretical side a huge number of papers undertook a critical review [3] of the QCD description of the nucleon and a renewed attention was given to the transverse spin phenomena, previously essentially ignored.

1.1.1 First observations of transverse spin effects

Let's consider a high-energy particle moving on a straight line, that for simplicity we can take as the longitudinal direction. The spin four-vector s^μ of such particle can be decomposed into a component $s^\mu_\parallel$, parallel to the particle momentum p^μ, and a transverse component $s^\mu_\perp$, perpendicular to it:

$$s^\mu = s^\mu_\parallel + s^\mu_\perp = kp^\mu + s^\mu_\perp. \tag{1.2}$$

If the particle moves with a Lorentz factor γ, the transverse spin components turn out to be suppressed of a factor $1/\gamma$ with respect to the longitudinal one. This argument led, in the past, to the idea that transverse spin effects are always negligible, but this is in general not true.

The first extensive discussion of transverse spin effects in high-energy hadronic physics was triggered by the discovery, in 1976, that Λ hyperons produced in unpolarised pN interaction exhibit a surprisingly large transverse polarisation at high p_T [4]. Soon after, the E704 experiment at FNAL discovered large and unexpected left-right single spin asymmetries in inclusive pion production in the collision of transversely polarised proton on a hydrogen target, results essentially confirmed at RHIC at $\sqrt{s}$=200 GeV twenty years later. All these phenomena are forbidden at leading-twist QCD and can arise only as an $\mathcal{O}(1/p_T)$ effect. Indeed, in a famous paper [5] it was proven that in collinear perturbative QCD single transverse spin asymmetries are of the order of $\alpha_s(m_q/\sqrt{s})$ and therefore vanish in the limit of massless quarks. Large transverse spin effects in hadron reactions, on the contrary, are not suppressed and their interpretation required a generalisation of collinear QCD, as will be seen in the following.

1.1.2 QCD structure of the nucleon

At leading order the QCD structure of the nucleon is described by three distribution functions: the number density, or unpolarised distribution $f_1(x)$; the helicity, or longitudinal polarisation distribution $g_1(x)$; and transversity, or transverse polarisation distribution $h_1(x)$. The unpolarised and helicity distributions are well known objects, for which a simple probabilistic interpretation holds: $f_1(x)$ is the probability of finding a quark with a fraction x of the longitudinal momentum of the unpolarised parent hadron, independently of the quark spin orientation; for a longitudinally polarised nucleon, $g_1(x)$ is the number density of quarks with momentum fraction x and spin aligned to that of the parent hadron minus the number density of quarks with the same fraction of momentum but opposite helicity.

Let us indicate with the superscript $\pm$ the sign of the quark helicity with respect to that of the parent nucleon. One has:

$$f_1(x) = f_1^+(x) + f_1^-(x), \qquad g_1(x) = f_1^+(x) - f_1^-(x). \tag{1.3}$$

Also $h_1(x)$ has a probabilistic interpretation: in a transversely polarised hadron, it represents the number density of quarks with momentum fraction x and their spin parallel to that of the parent hadron minus the number density of quarks with the same momentum fraction and their spin antiparallel. If $\uparrow$ indicates the parent nucleon transverse polarisation,

$$h_1(x) = f_1^{\uparrow}(x) - f_1^{\downarrow}(x). \tag{1.4}$$

In the helicity basis, transversity appears as an interference term and this simple interpretation does not hold anymore. For non relativistic quarks, moreover, h_1 and g_1 are equal, thus any difference between them probes the relativistic nature of quarks. The transversity distribution $h_1(x)$ was introduced already in the 70's [6] to describe the $pp \to \mu^+\mu^- X$ Drell-Yan reaction, but it was nearly forgotten until the beginning of 90's, when Artru and Mekhfi [7] studied its QCD evolution and Jaffe and Ji [3] inserted it in a general classification of all leading-twist and higher-twist parton distribution functions.

The three PDFs are proportional to the imaginary part of quark-nucleon forward amplitudes $\mathscr{A}_{\Lambda\lambda,\Lambda'\lambda'}$, where Λ refers to the nucleon helicity and λ to the quark helicity. Quark and hadron helicities generally take on the values $\pm 1/2$. Due to helicity conservation, the sum rule $\Lambda + \lambda = \Lambda' + \lambda'$ applies. According to this rule, three independent sets of helicity amplitudes exist, namely:

$$+\frac{1}{2} \quad +\frac{1}{2} \longrightarrow +\frac{1}{2} \quad +\frac{1}{2} \tag{1.5}$$

$$+\frac{1}{2} \quad -\frac{1}{2} \longrightarrow +\frac{1}{2} \quad -\frac{1}{2} \tag{1.6}$$

$$+\frac{1}{2} \quad -\frac{1}{2} \longrightarrow -\frac{1}{2} \quad +\frac{1}{2} \tag{1.7}$$

where the first two are diagonal in the helicity basis, since the quark does not flip its helicity. The third, instead, requires a spin flip. These three sets of amplitudes can be grouped into the three PDFs according to the scheme:

$$f_1(x) \leftrightarrow \left(+\frac{1}{2} \quad +\frac{1}{2} \longrightarrow +\frac{1}{2} \quad +\frac{1}{2}\right) + \left(+\frac{1}{2} \quad -\frac{1}{2} \longrightarrow +\frac{1}{2} \quad -\frac{1}{2}\right) \tag{1.8}$$

$$g_1(x) \leftrightarrow \left(+\frac{1}{2} \quad +\frac{1}{2} \longrightarrow +\frac{1}{2} \quad +\frac{1}{2}\right) - \left(+\frac{1}{2} \quad -\frac{1}{2} \longrightarrow +\frac{1}{2} \quad -\frac{1}{2}\right) \tag{1.9}$$

$$h_1(x) \leftrightarrow \left(+\frac{1}{2} \quad -\frac{1}{2} \longrightarrow -\frac{1}{2} \quad +\frac{1}{2}\right). \tag{1.10}$$

As a consequence, $f_1(x)$ and $g_1(x)$ are chiral-even, whereas $h_1(x)$ is chiral-odd. From the probabilistic interpretation of the three PDFs, it is easy to derive two fundamental constraint on helicity and transversity:

$$|g_1(x)| = |f_1^+(x) - f_1^-(x)| \leq f_1(x) \tag{1.11}$$

$$|h_1(x)| = |f_1^\uparrow(x) - f_1^\downarrow(x)| \leq f_1(x). \tag{1.12}$$

A combination of boundary conditions on the three PDFs is on the basis of the Soffer bound [8], which must be satisfied at leading order:

$$f_1(x) + g_1(x) \geq 2|h_1(x)|. \tag{1.13}$$

An important property of the leading order PDFs is that their first moments correspond to the vector, axial and tensor charges:

$$\int_{-1}^{+1} dx f_1(x) = \int_0^1 dx \left[f_1(x) - \bar{f}_1(x)\right] = g_V, \tag{1.14}$$

$$\int_{-1}^{+1} dx g_1(x) = \int_0^1 dx \left[g_1(x) - \bar{g}_1(x)\right] = g_A, \tag{1.15}$$

$$\int_{-1}^{+1} dx h_1(x) = \int_0^1 dx \left[h_1(x) - \bar{h}_1(x)\right] = g_T. \tag{1.16}$$

The tensor charge, in particular, is a fundamental quantity since it gives the contribution of the quark electric dipole moment to the nucleon electric dipole moment, a sensitive probe of CP violation beyond the Standard Model. Tensor charges can be calculated in lattice QCD.

The three PDFs are all leading-twist functions. This means that there is no reason to expect *a priori* that transversity should be smaller that helicity, at least at low Q^2. Their QCD evolution is instead different: $h_1(x)$ has no gluonic counterpart in spin one-half hadrons since a gluon transversity distribution for nucleon would violate helicity conservation. For this reason, $h_1(x)$ does not mix with gluons in the evolution, so that its evolution equation is a simple non-singlet quantity.

When transverse quark momentum $k_\perp$ is taken into account, the number of leading-twist distribution functions, necessary to characterise the nucleon structure, raises to eight. These transverse-momentum-dependent (TMD) distribution functions describe the quark-gluon dynamics with all possible spin-spin and spin-orbit correlations. The eight TMD PDFs are reported in Tab. 1.1. The symbols U, L and T refer to unpolarised, longitudinally polarised and transversely polarised nucleons (N) and quarks (q) respectively.

Table 1.1 Leading twist TMD distribution functions, listed according to their probabilistic interpretation.

N \ q	U	L	T
U	f_1		$h_1^\perp$
L		g_1	$h_{1L}^\perp$
T	$f_{1T}^\perp$	$g_{1T}^\perp$	h_1 $h_{1T}^\perp$

The diagonal elements are the momentum dependent distribution functions $f_1(x,k_\perp)$, $g_1(x,k_\perp)$ and $h_1(x,k_\perp)$: they do not vanish after an integration over $k_\perp$ and simply reduce to the already encountered leading-twist PDFs $f_1(x)$, $g_1(x)$ and $h_1(x)$. On the contrary, the off-diagonal term vanish after $k_\perp$ integration. Among them, the most interesting TMD PDFs are the T-odd $f_{1T}^\perp$ and $h_1^\perp$, known as the Sivers and Boer-Mulders functions.

1.2 Access to the nucleon spin structure

The spin structure of the nucleon, and in particular the helicity contribution $\Delta\Sigma$ of the quarks to the global spin, can be studied through (inclusive) *deep inelastic scattering* (DIS), where two of the three PDFs enter in the cross section. Transversity, instead, due to its chiral-odd nature, cannot be accessed in inclusive DIS and other channels, like e.g. *semi-inclusive deep inelastic scattering* (SIDIS), must be chosen.

1.2.1 Deep inelastic scattering (DIS)

Deep inelastic scattering (DIS, Fig. 1.1) refers to the scattering of a high energy lepton ℓ off a nucleon N. The basic reaction is:

$$\ell N \to \ell' X \tag{1.17}$$

where X is a generic final hadronic state. If only the final lepton is observed, DIS is called *inclusive*; if, in coincidence with ℓ', X is observed also, DIS is said to be *semi-inclusive* (if X is partially observed) or *exclusive* (if X is completely reconstructed).

When the nucleon is at rest in the laboratory, the expression for its Lorentz vector is simply $P_\mu = (M,0,0,0)$, being M the nucleon mass, while the incoming lepton Lorentz vector (neglecting the lepton mass and taking its line of flight as z-axis) can be written as $\ell_\mu = (E,0,0,E)$. In the one photon exchange approximation, the scattering occurs via the exchange of a virtual photon, whose four-vector is the difference of the incoming and outgoing leptons: $q_\mu = \ell_\mu - \ell'_\mu = (E,0,0,E) - (E',0,E'\sin\theta, E'\cos\theta)$, being θ the scattering angle.

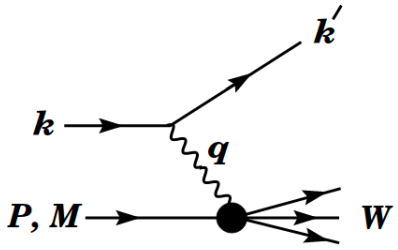

Figure 1.1 Kinematic quantities for the description of deep inelastic scattering. Note that here the lepton momenta are indicated as k and k'.

In inclusive DIS only two independent Lorentz invariants can be constructed. They can be chosen to be the invariant mass of the virtual photon

$$Q^2 = -q^2 \tag{1.18}$$

and the Bjorken variable

$$x = \frac{Q^2}{2P \cdot q}. \tag{1.19}$$

Q^2 is also indicated as the resolution of the electromagnetic probe: high values of Q^2 correspond to a deeper investigation of the nucleon inner structure. In the QPM framework, and in particular in the so-called *infinite momentum frame*, where the nucleon moves with infinite momentum, x is interpreted as the fraction of the nucleon momentum carried by the quark which, at the elementary level, absorbs the virtual photon. In terms of Q^2 and x, DIS can be defined as the limit $Q^2 \to \infty$ with x fixed.

Other useful kinematic variables that can be introduced to describe DIS reactions are:

$$\nu = \frac{P \cdot q}{M}, \qquad y = \frac{P \cdot q}{P \cdot k}, \qquad W^2 = (P+q)^2 \tag{1.20}$$

where ν corresponds to the photon energy in the laboratory frame, y is the inelasticity and W is the final state hadron mass. Both x and y range between 0 and 1 and they are related to Q^2 through the relation:

$$xy = \frac{Q^2}{s - M^2}. \tag{1.21}$$

where s is the center of mass energy.

The differential DIS cross section, to detect the outgoing lepton in the solid angle $d\Omega$ and in the energy range $(E', E' + dE')$ in the laboratory frame, can be calculated as the

contraction of a leptonic tensor $L_{\mu\nu}$ and a hadronic tensor $W^{\mu\nu}$:

$$\frac{d^2\sigma}{dE'd\Omega} = \frac{\alpha^2}{2MQ^4}\frac{E'}{E}L_{\mu\nu}W^{\mu\nu} \tag{1.22}$$

where $\alpha = 1/137$ is the electromagnetic coupling constant. The leptonic tensor $L_{\mu\nu}$ is function of the incoming and outgoing lepton momenta and spins (ℓ, ℓ', s_ℓ, $s_{\ell'}$ respectively) but, since the final lepton spin is in general not observed, we can sum over it. $L_{\mu\nu}$ can then be decomposed into two terms, the first symmetric and independent on s_ℓ, the second antisymmetric and dependent on s_ℓ:

$$L_{\mu\nu}(\ell,\ell',s_\ell) = L^{(S)}_{\mu\nu}(\ell,\ell') + L^{(A)}_{\mu\nu}(\ell,\ell',s_\ell). \tag{1.23}$$

An analogous separation into symmetric and antisymmetric part (the former independent on the nucleon spin S, the latter dependent on it) is possible also for the hadronic tensor:

$$W^{\mu\nu}(P,q,S) = W^{\mu\nu}_{(S)}(P,q) + W^{\mu\nu}_{(A)}(P,q,S) \tag{1.24}$$

with the *caveat* that, while the leptonic tensor can be exactly computed in QED, this is not true for the hadronic tensor, due to the unknown nucleon inner structure. A necessary hadronic tensor parametrisation is then performed introducing two structure functions for the symmetric part (F_1 and F_2) and two for the antisymmetric part (g_1 and g_2).

The contraction of a symmetric tensor with an antisymmetric one is zero, so that the spin-independent cross section can be extracted from the contraction of the symmetric parts of $L_{\mu\nu}$ and $W^{\mu\nu}$, while the spin-dependent cross section comes from the contraction of their antisymmetric parts:

$$\frac{d^2\sigma}{dE'd\Omega} = \frac{4\alpha^2E'^2}{Q^4}\left[\frac{2F_1(x,Q^2)}{M}\sin^2\frac{\theta}{2} + \frac{F_2(x,Q^2)}{\nu}\cos^2\frac{\theta}{2}\right] \tag{1.25}$$

$$\frac{d^2\Delta\sigma}{dE'd\Omega} = \frac{4\alpha^2E'}{Q^2M\nu E}\left[(E+E'\cos\theta)g_1(x,Q^2) - \frac{Q^2}{\nu}g_2(x,Q^2)\right] \tag{1.26}$$

where $\Delta\sigma$ expresses the difference in the cross section for the nucleon spin parallel and antiparallel with respect to the beam spin direction. In the light of the QPM, the structure functions can be written in terms of the f_1 and g_1 PDFs as:

$$F_1(x,Q^2) = \frac{1}{2}\sum_q e_q^2\left[f_1^q(x,Q^2) + \bar{f}_1^q(x,Q^2)\right] \tag{1.27}$$

$$F_2(x,Q^2) = x\sum_q e_q^2 \left[f_1^q(x,Q^2) + \bar{f}_1^q(x,Q^2)\right] \tag{1.28}$$

$$g_1(x,Q^2) = \frac{1}{2}\sum_q e_q^2 \left[g_1^q(x,Q^2) + \bar{g}_1^q(x,Q^2)\right] \tag{1.29}$$

while $g_2(x,Q^2)$ has not a simple QPM interpretation.

The correlation between F_1 and F_2 is given by the Callan-Gross relation, which is a consequence of the fermionic nature of quark: $F_2(x,Q^2) = 2xF_1(x,Q^2)$.

Unpolarised and polarised DIS are privileged frameworks in which the unpolarised distribution function and helicity distribution function can be studied. This is not true for the transversity distribution function that must be associated to a second chiral-odd object to provide an observable quantity. Such an object can be found, for instance, in SIDIS.

1.2.2 Semi-inclusive deep inelastic scattering

Let's consider the process:

$$\ell N \to \ell' hX \tag{1.30}$$

where the hadron h is observed in coincidence with the scattered lepton ℓ'. The projection of the hadron momentum along the virtual photon momentum, estimated in the photon-nucleon center of mass frame, usually indicated as $p_\parallel^*$, can reach at maximum the value of $W/2$. It is then useful to introduce a new variable, the Feynman x or x_F, defined as the ratio:

$$x_F = \frac{2p_\parallel^*}{W} \Rightarrow -1 \leq x_F \leq 1. \tag{1.31}$$

In this frame the quark which absorbed the virtual photon has $p_\parallel^* > 0$, whereas the other quarks, that continue in the initial nucleon direction, have $p_\parallel^* < 0$. In a simplified model, then, hadrons with $x_F > 0$ come from the hadronisation of the quark which absorbed the virtual photon (kinematic region of *current fragmentation*, CFR) and those with $x_F < 0$ come from the *target fragmentation* (TFR) region. As a matter of fact, the separation of the two regions is not so sharp, and usually further requirement on the hadron energy are applied to select the CFR.

The ratio of the hadron energy E_h to the virtual photon energy ν is indicated as z. This quantity governs the probability for a quark q to fragment into a hadron h with energy $z\nu$, described by fragmentation functions (FFs), which depend only on z and on Q^2. SIDIS FFs are chiral-odd objects and, then, they can couple to transversity.

The SIDIS cross section for the production of a specific hadron in the final state is an example of application of the factorisation theorem, according to which it is possible to

separate the perturbatively calculable part of the cross section from the non perturbative one. In SIDIS, the non perturbative term usually corresponds to FFs, so that the factorisation theorem schematically reads:

$$\sigma^{\ell N \to \ell h X} = \hat{\sigma} \otimes PDF \otimes FF \tag{1.32}$$

where $\hat{\sigma}$ denotes the perturbatively calculable cross section for the elementary subprocess $\ell q \to \ell' q'$. Generally speaking, the FFs describe how the color-carrying quarks and gluons transform into color-neutral particles such as hadrons or photons. While (leading-order) PDFs can be seen in the QPM as probability densities for finding partons, with a given momentum, inside color-neutral particles, the FFs are probability densities for finding color-neutral particles inside partons.

The simplest FF, and also the best known, is denoted by $D_1^{h/q}(z)$ and describes the fragmentation of an unpolarised parton of type q into an unpolarised hadron h, where the hadron carries the fraction z of the parton momentum. $D_1^{h/q}(z)$ is also known as collinear, or integrated, FF: the transverse momentum $\vec{k}_T$ of the hadron relative to the parton is integrated over. In addition to $D_1^{h/q}(z)$, one can extend the set of FFs by considering the spin of the parton, that of the produced hadron and the transverse momentum of the hadron relative to the parton [9]. The two most common classes of FFs are:

- Integrated FFs: $D_1^{h/q}(z)$ with its two spin-dependent counterparts $G_1^{h/q}(z)$ and $H_1^{h/q}(z)$ that, unlike $D_1^{h/q}(z)$, take into account the hadron when it is polarised, respectively longitudinally and transversely with respect to its momentum. These three FFs are leading-twist (twist-2) objects.

- Transverse-momentum-dependent (TMD) FFs: they depend on the hadron transverse momentum $\vec{k}_T$ and they are needed to probe the transverse momentum dependence of the parton distribution functions, as well as the transversity PDF.

The FFs are listed in Tab. 1.2 according to their probabilistic interpretation. The columns indicate the quark polarisation (unpolarised-U, longitudinally polarised-L, transversely polarised-T). The rows indicate the hadron polarisation. They depend on both z and on $\vec{k}_T$.

The integrated FFs can be obtained by integrating the TMD FFs: for instance,

$$D_1^{h/q}(z) = z^2 \int d^2\vec{k}_T D_1^{h/q}(z; z^2\vec{k}_T^2). \tag{1.33}$$

Table 1.2 TMD fragmentation functions, listed according to their probabilistic interpretation.

H \ q	U	L	T
U	$D_1^{h/q}$		$H_1^{\perp h/q}$
L		$G_1^{h/q}$	$H_{1L}^{\perp h/q}$
T	$D_{1T}^{\perp h/q}$	$G_{1T}^{h/q}$	$H_1^{h/q}$ $H_{1T}^{\perp h/q}$

1.2.3 Measurement of transversity

The FFs are assumed to be process-independent: they describe the quark hadronisation in all the different processes, namely in SIDIS, e^+e^- annihilation and pp hard scattering. In these cases, using QCD factorisation, the cross sections are schematically written as:

$$\sigma^{e^+e^-\to hX} = \hat{\sigma} \otimes FF \tag{1.34}$$

$$\sigma^{\ell N\to \ell' hX} = \hat{\sigma} \otimes PDF \otimes FF \tag{1.35}$$

$$\sigma^{pp\to \ell' hX} = \hat{\sigma} \otimes PDF \otimes PDF \otimes FF \tag{1.36}$$

where $\hat{\sigma}$ indicates the process-dependent partonic cross section calculated in perturbative theory. This is a very important point, since it states that information on the FFs from, for instance, e^+e^- annihilation can be used to extract PDFs from SIDIS. In particular, this is the case for $H_{1T}^{\perp,h/q}$, called the *Collins function*. In SIDIS it couples with the chiral-odd transversity PDF giving a well defined transverse spin asymmetry, the so called *Collins asymmetry*. Simultaneous use of the SIDIS and e^+e^- data allows for the extraction of the transversity and the Collins FFs, as described in Sect. 1.4.

To access transversity another important process is the SIDIS production of spinless hadron pairs. In this case a new FF has been introduced, the so-called *DiFF* (Di-hadron Fragmentation Function) $H_1^{\sphericalangle}$, which can also be accesses in $e^+e^- \to$ hadrons. Recently, experimental investigations however gave hints for a common origin of the $H_{1T}^{\perp}$ and $H_1^{\sphericalangle}$ FFs [10]. Also, a Monte Carlo implementation of the $^3P_0$ model can describe simultaneously the asymmetries in one hadron and two hadrons production in the fragmentation of a transversely polarised quark.

Of particular interest for the present work are the FFs describing the production of the spin one-half Λ or $\bar{\Lambda}$ hyperons. $G_1^{\Lambda/q}(z)$ shows up in SIDIS off longitudinally polarised nucleons ($\ell\vec{p} \to \ell'\vec{\Lambda}X$) and in $\vec{p}p \to \vec{\Lambda}X$ [9]. Specific for the measurement of the transversity PDF is $H_1^{\Lambda/q}(z)$ to which it couples in the process $\ell p^\uparrow \to \ell'\Lambda^\uparrow X$ and $pp^\uparrow \to \Lambda^\uparrow X$, still unknown.

The measurement of the transverse polarisation of Λs and $\bar{\Lambda}$s produced in SIDIS off transversely polarised nucleons has always been indicated as a promising channel to access

transversity [11–14]. It is the subject of this thesis and will be treated in detail in the next section.

The basic idea is that, if transversity is different from zero, the polarisation of the fragmenting quark is transferred to the Λ according to $H_1^{\Lambda/q}$, so that the Λ is polarised and its polarisation can be measured from the angular distribution of the proton produced in the decay $\Lambda \to p\pi^-$.

The semi-inclusive production of a Λ hyperon is shown in Fig. 1.2. The incoming lepton (here, a muon μ) emits a virtual photon γ^*, which interacts with the nucleon N to give the Λ and other products X, not observed. The incoming and outgoing muons μ and μ' define the *scattering plane*; the photon γ^* and the Λ define the *production plane* and the two decay products (proton p and pion π^-) form the *decay plane*.

The two processes, Λ production and decay, are described in the next section.

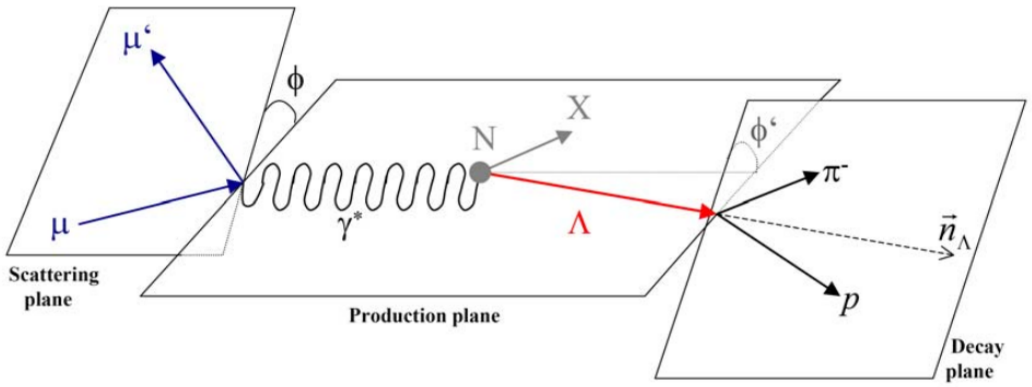

Figure 1.2 Λ production and decay in SIDIS.

1.3 Λ production and decay

Of particular interest is the semi-inclusive deep inelastic process $\ell N^{\uparrow} \to \ell' hX$, where an unpolarised lepton ℓ interacts with a valence quark of the transversely polarised nucleon $N^{\uparrow}$ and the struck quark fragments into a hadron h of spin one-half. If at least part of the initial transverse polarisation is transferred to the hadron in the fragmentation, this polarisation should be detectable. A possibility is offered in this sense by the hyperon self-analysing decay, as will be discussed in the following section. In this section we first consider the transfer of transverse polarisation from the target nucleon to the Λ hyperon, and then the measurement of the transverse Λ polarisation.

1.3.1 Transmitted transverse polarisation

A simple explanation of the polarisation transfer is given in Ref. [15]. If $\vec{P}_N$ is the nucleon transverse polarisation, the initial quark inherits part of it according to the relation:

$$\vec{P}_q = \frac{h_1^q(x)}{f_1^q(x)} \vec{P}_N, \tag{1.37}$$

where h_1^q and f_1^q are the transversity and the number density PDFs. $\vec{P}_q$ gets lowered and rotated in the hard scattering process with the lepton. In the lepton-quark center of mass frame:

$$\vec{P}'_q = D_{NN} R \vec{P}_q, \tag{1.38}$$

where D_{NN} is the *depolarisation factor* and R is the rotation about the normal to the scattering plane that transforms the initial quark direction into the final one. From QED one gets

$$D_{NN} = \frac{2(1-y)}{1+(1-y)^2} \tag{1.39}$$

and R essentially is a reflection about the y-z plane which brings the direction of spin of the initial quark into that of the final one. Also the final hadron inherits part of the outgoing quark polarisation, with a probability given by the ratio between the transversely polarised and unpolarised fragmentation functions:

$$\vec{P}_q^h = \frac{H_1^{h/q}(z)}{D_1^{h/q}(z)} \vec{P}'_q. \tag{1.40}$$

Summing over the quark species, we get:

$$\vec{P}_h = \frac{\sum_q e_q^2 h_1^q(x) H_1^{h/q}(z)}{\sum_q e_q^2 f_1^q(x) D_1^{h/q}(z)} D_{NN} R \vec{P}_N \tag{1.41}$$

where now R is the rotation about the normal to the scattering plane that transforms the initial nucleon's direction into the final hadron's one.

The Λ polarisation is calculated in γ^*-nucleon center of mass (GNS frame, Fig. 1.3) in Ref. [16] working with a transversely polarised nucleon. In the GNS, the z-axis is given by the photon direction, the xz plane is the scattering plane and the y-axis is parallel to the normal to the scattering plane. The components of the Λ polarisation are :

$$P_y = S_y \frac{\sum_q h_1^q(x) H_1^{h/q}}{\sum_q f_1^q(x) D_1^{h/q}} D_{NN}, \qquad P_x = -S_x \frac{\sum_q h_1^q(x) H_1^{h/q}}{\sum_q f_1^q(x) D_1^{h/q}} D_{NN}. \tag{1.42}$$

where S_x and S_y are the x and y components of the nucleon spin vector $\vec{S}$.

To observe the predicted baryon transverse polarisation, an interesting possibility is offered by the hyperons *self-analysing decay*, that will be investigated in the following section.

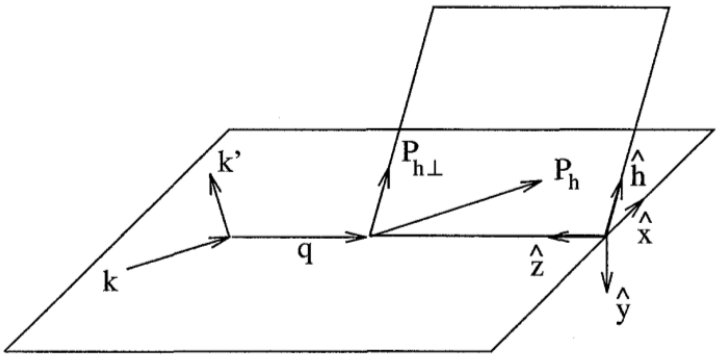

Figure 1.3 Coordinate system in the GNS frame.

1.3.2 Hyperon self-analysing decay

A natural choice to investigate the *transversity transmitted* polarisation, expected in semi-inclusive leptoproduction of spin one-half hadrons, is to study events with hyperons in the final state. The hyperons are in fact self-analysing, that is they reveal their polarisation

through the angular dependence of their non-leptonic decay products, like e.g.:

$$\begin{array}{lll} \Lambda^0 \to p\pi^- & \Sigma^+ \to p\pi^0 & \Xi^0 \to \Lambda^0\pi^0 \\ \Lambda^0 \to n\pi^0 & \Sigma^+ \to n\pi^+ & \Xi^- \to n\pi^- \\ & \Sigma^- \to n\pi^- & \end{array}$$

The most easily accessed process is the weak decay $\Lambda^0 \to p\pi^-$ (correspondingly $\bar{\Lambda}^0 \to \bar{p}\pi^+$) which has branching ratio is 63.9 %. On one side, this decay channel is the most favourable in terms of statistics; on the other hand, however, only part of the observed Λs come from direct production, since they can also appear as decay products of heavier hyperons. In this thesis we will ignore this second possibility.

Like all hyperon non-leptonic decays, Λ decay is characterised by the presence of two spin-1/2 baryons (one in the initial state as decaying particle, the other as decay product) and of a spin-0 meson. The most general Lorentz-invariant amplitude for this process can be written as [17]:

$$\mathscr{M} = G_F m_\pi^2 \bar{u}_f (A - B\gamma_5) u_i \tag{1.43}$$

where G_F is the Fermi constant, m_π is the pion mass, u_i and u_f are Dirac spinors for the initial and final baryons respectively, and A and B are dimensionless constants. The parity violation is induced by the presence of the γ_5 matrix. Starting from the expression in Eq. 1.43, the angular distribution of the final baryon in the rest frame of the decaying one can be calculated. Let's then fix the expression for u_i and u_f introducing the Dirac bispinors χ_i and χ_f:

$$u_i = \begin{pmatrix} \chi_i \\ 0 \end{pmatrix}, \qquad u_f = \left(\frac{E_f + m_f}{2m_f}\right)^{\frac{1}{2}} \begin{pmatrix} \chi_f \\ \frac{\vec{\sigma}\cdot\vec{p}_f}{E_f+m_f}\chi_f \end{pmatrix} \tag{1.44}$$

where E_f, m_f and $\vec{p}_f$ indicate the final baryon energy, mass and momentum and $\vec{\sigma}$ is the vector of Pauli matrices. Thus, inserting u_i and u_f in Eq. 1.43,

$$\mathscr{M} = G_F m_\pi^2 \left(\frac{E_f + m_f}{2m_f}\right)^{\frac{1}{2}} \left(A\chi_f^\dagger \chi_i + B\chi_f^\dagger \frac{\vec{\sigma}\cdot\vec{p}_f}{E_f+m_f}\chi_i\right). \tag{1.45}$$

where γ_5, acting on χ_i, introduces a change of sign. To simplify the notation, let us define:

$$\hat{p}_f = \frac{\vec{p}_f}{|\vec{p}_f|}, \qquad a = A, \qquad b = \frac{B|\vec{p}_f|}{E_f + m_f} \tag{1.46}$$

$$\Rightarrow \mathscr{M} = G_F m_\pi^2 \left(\frac{E_f + m_f}{2m_f}\right)^{\frac{1}{2}} \left(\chi_f^\dagger (a + b\vec{\sigma}\cdot\hat{p}_f)\chi_i\right). \tag{1.47}$$

The transition probability will then be proportional to:

$$\begin{aligned}\mathscr{R} \propto |\chi_f^\dagger(a+b\vec{\sigma}\cdot\hat{p}_f)\chi_i|^2 &= \chi_f^\dagger(a+b\vec{\sigma}\cdot\hat{p}_f)\chi_i\chi_i^\dagger(a^*+b^*\vec{\sigma}\cdot\hat{p}_f)\chi_f \\ &= \mathrm{Tr}\left[\left(\frac{1+\vec{\sigma}\cdot\hat{\omega}_f}{2}\right)(a+b\vec{\sigma}\cdot\hat{p}_f)\left(\frac{1+\vec{\sigma}\cdot\hat{\omega}_i}{2}\right)(a^*+b^*\vec{\sigma}\cdot\hat{p}_f)\right]\end{aligned} \tag{1.48}$$

where $\hat{\omega}_i$ and $\hat{\omega}_f$ are unit vectors in the directions of initial and final baryon spins, respectively. The expression for the two spin density matrices substitute the products $\chi_i\chi_i^\dagger$ and $\chi_f\chi_f^\dagger$ and a trace must be evaluated to get the correct expectation value. Since our concern is initial state polarisation, we can sum over all possible $\hat{\omega}_f$ states to get a quantity proportional to:

$$\mathrm{Tr}\left[(a+b\vec{\sigma}\cdot\hat{p}_f)\,(1+\vec{\sigma}\cdot\hat{\omega}_i)\,(a^*+b^*\vec{\sigma}\cdot\hat{p}_f)\right]. \tag{1.49}$$

The product of all terms inside the trace yields:

$$|a|^2(1+\vec{\sigma}\cdot\hat{\omega}_i)+(ab^*+a^*b)(\vec{\sigma}\cdot\hat{p}_f)(1+\vec{\sigma}\cdot\hat{\omega}_i)+|b|^2(1+(\vec{\sigma}\cdot\hat{p}_f)(\vec{\sigma}\cdot\hat{\omega}_i)(\vec{\sigma}\cdot\hat{p}_f)). \tag{1.50}$$

Now, recalling that the trace of a sum is equal to the sum of the traces, that $\mathrm{Tr}(\vec{\sigma}\cdot\vec{v})=0$ always and that $(\vec{\sigma}\cdot\vec{p})(\vec{\sigma}\cdot\vec{q})=(\vec{p}\cdot\vec{q})I+i\vec{\sigma}\times\vec{\sigma}$,

$$\mathscr{R} \propto |a|^2+|b|^2+2\mathrm{Re}(ab^*)(\hat{\omega}_i\cdot\hat{p}_f) \tag{1.51}$$

so that, introducing the weak decay parameter:

$$\alpha = \frac{2\mathrm{Re}(ab^*)}{|a|^2+|b|^2} \tag{1.52}$$

the decay rate $\mathscr{R}$ can be written as:

$$\mathscr{R} \propto 1+\alpha\hat{\omega}_i\cdot\hat{p}_f. \tag{1.53}$$

which means that, in the hyperon rest frame, the transition rate shows a dependence on the angle between the hyperon spin direction and the final baryon momentum. This transition rate asymmetry reflects on the number of baryons emitted per solid angle and, integrating over the azimuthal angle, we are left with the expression:

$$\frac{dN}{d\cos\theta} \propto (1+\alpha\cos\theta) \tag{1.54}$$

The α parameter for Λ decay has been measured to be $\alpha = 0.642 \pm 0.013$ [18], with an opposite sign in the case of $\bar{\Lambda}$: the deviation from an isotropic emission is remarkable. Eq. 1.54 describes the angular distribution in a frame where the axis, with respect to which the angle θ is defined, is chosen along the spin of the hyperon. In an experimental measurement it is not always possible to realise such a frame and it becomes necessary to introduce a quantization axis. The angle θ must then be redefined with respect to the new axis and the angular asymmetry takes the more general form:

$$\frac{dN}{d\cos\theta'} \propto 1 + \alpha P^H \cos\theta'. \tag{1.55}$$

where the *intrinsic* weak decay polarisation, induced by α only, substituted by a more suitable αP^H term that strongly depends on the chosen polarisation axis.

The general formula for the angular dependence of the emitted baryons can be obtained in another way, tailored to the case of Λ decay. Such alternative derivation [19] stresses the role of parity and angular momentum in the decay and, considering the contribution of s and p waves (the first parity-violating, the second parity-conserving), gives again Eq. 1.54.

To summarise, if for Λ ($\bar{\Lambda}$) production in SIDIS off a transversely polarised nucleon we choose as polarisation axis the direction of the spin of the struck quark and we measure the angular distribution of the proton (antiproton) produced in the Λ ($\bar{\Lambda}$) rest frame, it is:

$$\frac{dN^{p(\bar{p})}}{d\cos\theta} \propto 1 \pm \alpha P^{\Lambda(\bar{\Lambda})} \cos\theta. \tag{1.56}$$

where

$$P^{\Lambda(\bar{\Lambda})} = S_N \frac{\sum_q h_1^q(x) H_1^{h/q}}{\sum_q f_1^q(x) D_1^{h/q}} D_{NN} \tag{1.57}$$

with S_N the nucleon transverse polarisation.

1.4 Experimental overview

In this section, a brief overview of the most important experimental results concerning transversity are reported. As previously stressed, SIDIS is a unique tool to access it. Measurements of transversely polarised pp hard scattering would also be important but in the Drell-Yan process transversity of the valence quarks are convoluted with transversity of the sea antiquarks giving rise to very small transverse spin asymmetries, while in hadron inclusive production, where transverse spin effects have been measured at high energy by the RHIC experiments, the Collins effect is mixed to the Sivers effect, preventing a clear access to transversity. Only very recently signals of the transversity distribution have been seen by looking at hadron distributions inside the jets. The cleanest process would be transversely polarised proton-antiproton Drell-Yan process which would allow to measure the convolution of the two transversity functions, and the measurements have been proposed at the FAIR facility at GSI [20, 21]. Unfortunately the feasibility of polarised antiproton beams has still to be proven and these experiments will not be performed in the near future.

Today, all the knowledge on transversity is coming from the SIDIS results produced by the HERMES and the COMPASS collaborations about the Collins asymmetry and the two-hadron asymmetry [22]. They are shown in the next sections of this chapter, together with the preliminary COMPASS results on Λ transmitted transverse polarization.

Collins and dihadron asymmetries

The Collins effect consists in a left-right asymmetry, with respect to the plane defined by the quark momentum and quark spin, in the azimuthal distribution of hadrons produced in the hadronisation of transversely polarised quarks. Its amplitude is encoded in the $H_{1T}^{\perp}$ FF, the so-called Collins function. When coupled to the transversity distribution in SIDIS off transversely polarised nucleons, it gives a specific $\sin\Phi_C$ modulation in the cross section. The azimuthal Φ_C angle, the Collins angle, is defined as $\Phi_C = \phi_h + \phi_S - \pi$ where ϕ_h and ϕ_S are the azimuthal angles of the hadron transverse momentum and of the nucleon transverse spin in the GNS reference frame. The amplitude of the modulation allows to measure the so-called Collins asymmetry given by:

$$A_{Coll} \sim \frac{\sum_q e_q^2 h_1^q(x) \otimes H_1^{\perp,h/q}}{\sum_q e_q^2 f_1^q(x) \otimes D_1^{h/q}}. \tag{1.58}$$

The symbol $\otimes$ indicates a convolution over transverse momenta which can be only solved assuming specific dependences (typically Gaussian dependences) of the PDFs and the FFs

on the corresponding transverse momenta. In order to perform flavor separation the Collins asymmetry has been measured with transversely polarised deuterons (COMPASS [23, 24]) and proton (COMPASS [25, 26] and HERMES [27]) and for charged and identified final state hadrons. The results are shown in Fig. 1.4 and Fig. 1.5.

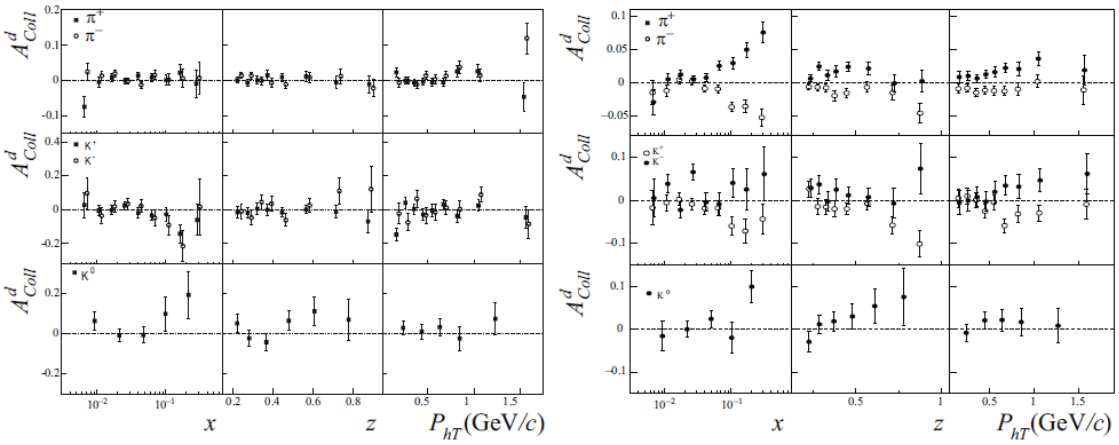

Figure 1.4 COMPASS measurement of the Collins asymmetries for charged pions, charged kaons and K^0s on deuterons (left) and on protons (right) as function of x, z and the hadron transverse momentum in the GNS P_{hT}.

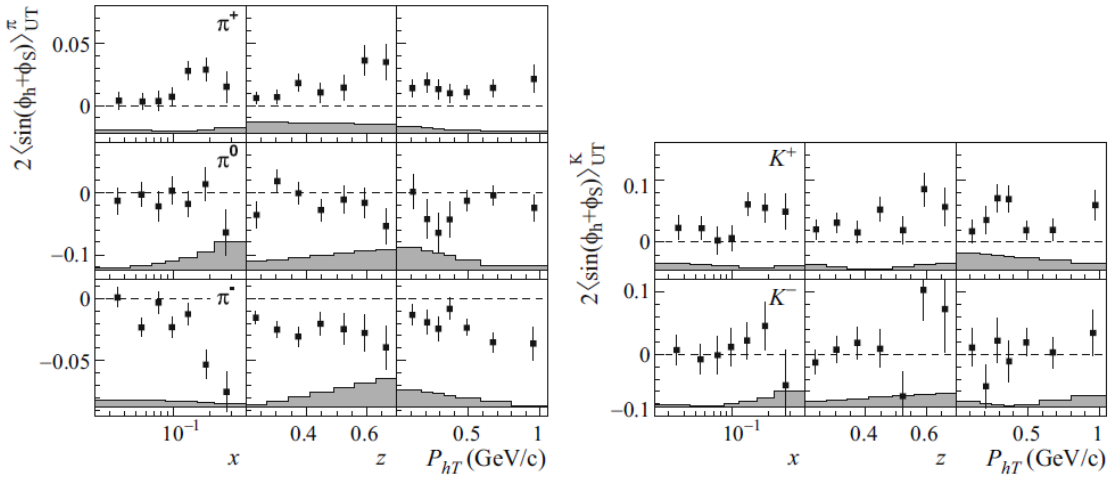

Figure 1.5 HERMES measurement of Collins asymmetries on protons for pions (left) and kaons (right) as function of x, z and the hadron transverse momentum in the GNS P_{hT}.

As can be seen the asymmetries for deuteron are small and compatible with zero, while they are clearly different from zero for proton data, in particular in the case of charged pions. The sign is opposite for positive and negative pions and the absolute values are quite

close and increase in the quark valence region ($x > 0.1$). The agreement between the two experiments is very good once the different sign convention for Φ_C is taken into account, in spite of the different lepton beam energies (27 GeV at HERMES, 160 GeV at COMPASS). The first HERMES result and the COMPASS result constituted the first evidence that both the transversity and the Collins functions are different from zero and persist at high energies too. Recently, measurements with a n target have been performed at lower energy at Jefferson Lab [28].

The di-hadron asymmetry has been measured soon later both at HERMES (p) and COMPASS (p and d) from the same data used to extract the Collins asymmetry. It is the amplitude of the modulation in $\sin\Phi_{RS}$ in the cross section, where $\Phi_{RS} = \phi_R + \phi_S - \pi$, with ϕ_R the azimuthal angle of the relative transverse momentum of the oppositely charged hadrons in the pair. The asymmetry can be written as:

$$A_{RS} \sim \frac{\sum_q e_q^2 h_1^q(x) H_1^{\sphericalangle,2h/q}(Z)}{\sum_q e_q^2 f_1^q(x) D_1^{2h/q}(Z)} \tag{1.59}$$

where $Z = z_1 + z_2$ is the sum of the z values of the two hadrons.

The COMPASS results are shown in Fig. 1.6. Again, with the deuteron target the asymmetry is compatible with zero, while for proton it shows a clear signal in the case of the highest statistics pion pair measurement, similar to that of the Collins asymmetry for positive pions. The fact that the x dependence is very close in the two cases is expected, since it is due to the transversity x dependence. The same sign and the absolute value is well explained assuming that the convolution over transverse momenta is not relevant and that the Collins effect is responsible for both asymmetries as already stressed.

All these data have been used by several groups to extract transversity, together with the corresponding measurements performed in $e^+e^- \to$ hadrons giving independent information on the spin dependent FFs. The results have large uncertainties, in particular for the d quark transversity due to the low statistics of the deuteron data set, but the results are in good agreement. Some of the results are shown in Fig. 1.7 [29]. There the points are the u and d quark transversity functions obtained directly from the COMPASS proton and deuteron data for the Collins asymmetry using the analyzing power extracted from the Belle e^+e^- data [30] at the Q^2 of the COMPASS experiment, ranging from 1.4 to about 25 GeV^2/c^2 in the different x bins. In this analysis the transversity function for the sea quarks has been obtained to be compatible with zero. The curves in Fig. 1.7 show the result from a simultaneous fit [31] of the COMPASS, HERMES and Belle data. The error bands refer to $Q^2 = 10$ GeV^2/c^2. The solid line and the dashed line show the central values at $Q^2 = 10$ GeV^2/c^2 and $Q^2 = 10$

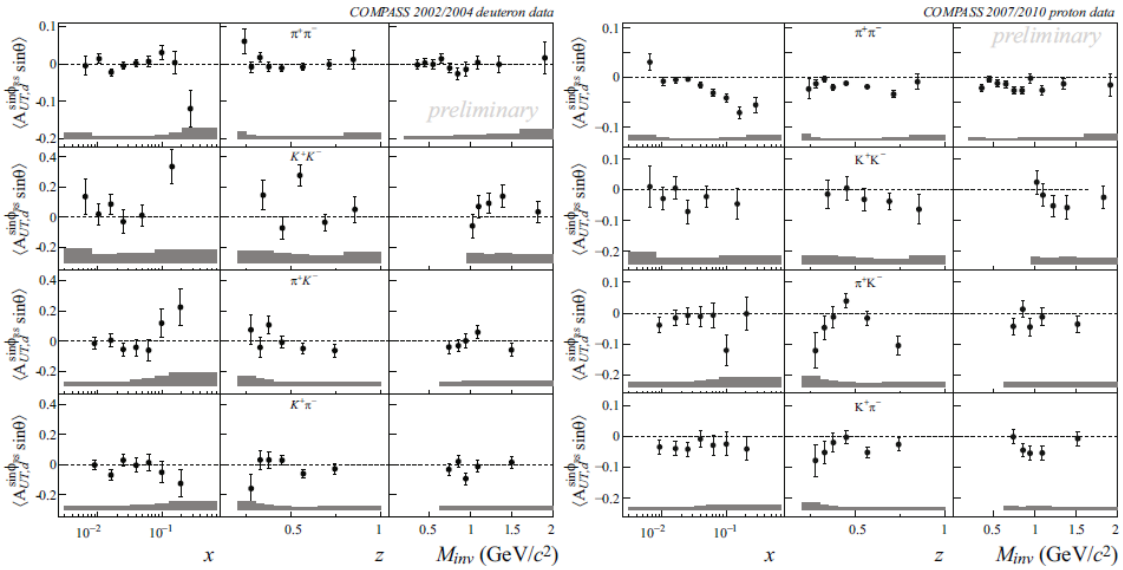

Figure 1.6 COMPASS measurement of the two identified hadron asymmetries, for different combinations of pions and kaons, on deuterons (left) and on protons (right) as function of x, Z and the invariant mass.

GeV^2/c^2, respectively. In both cases the uncertainties are statistical only. As can be seen, the results of the two extraction methods are in good agreement.

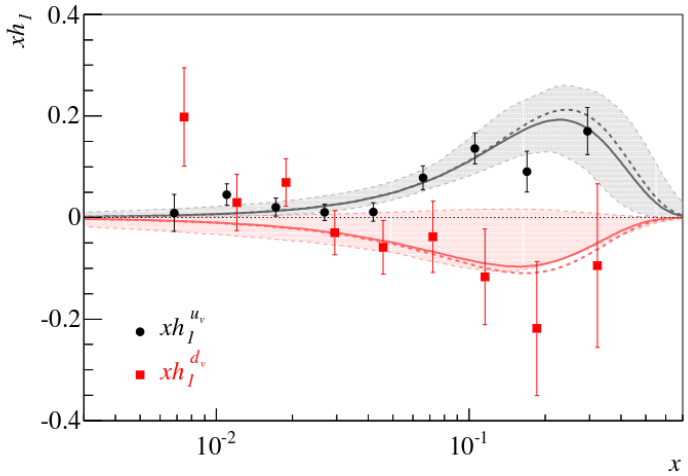

Figure 1.7 Transversity distribution for u and d valence quarks, extracted from Collins asymmetries. The figure is from Ref. [29].

Λ polarisation

The first measurements of the Λ transmitted transverse polarisation have been performed in COMPASS using the methods described in the previous sections and all the data collected with the transversely polarised deuteron target. The preliminary (still unpublished) results are shown in Fig. 1.8 [32]. The measured polarisation was different from zero for $\bar{\Lambda}$s, but with a large background and poor statistic inside the mass peak.

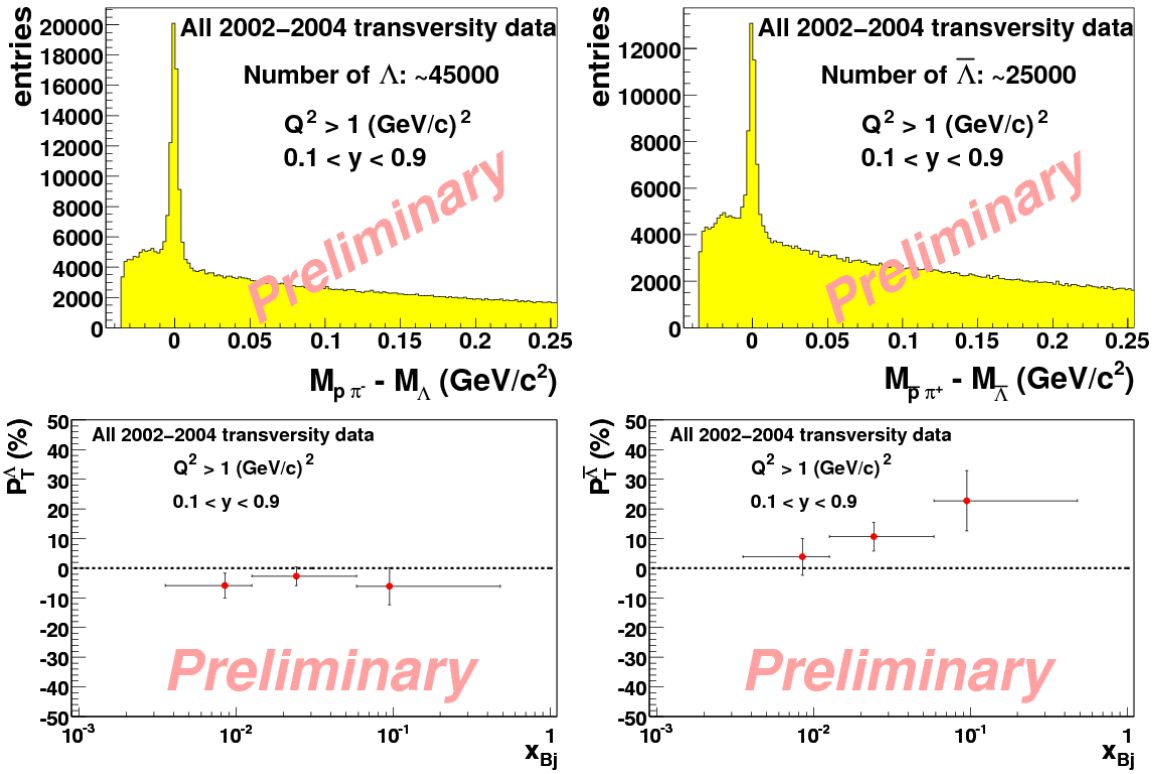

Figure 1.8 COMPASS preliminary results on Λ (left) and $\bar{\Lambda}$ (right) transmitted transverse polarisation from deuteron data. The top plots show the invariant mass distributions; the bottom plots the measured polarisations vs x. The bars show the statistical errors.

The same analysis was performed using the proton target data collected in 2007 [33]. The major improvement in analysis was the use of the RICH information for particle identification in the selection of the Λ candidates. As can be seen in Fig. 1.9, top plots, the background in the invariant mass distribution is much lower. Still the statistics is marginal and the polarisations compatible with zero both in x and in z bins (Fig. 1.9, bottom plots). No attempt has been done to extract transversity from those measurements, because of the fact that the relevant FFs are unknown and not yet measured in the e^+e^- annihilation channel and because

the statistical uncertainties on the results are large. Still predictions for the FFs exist, and calculations have been performed in different models.

In Ref. [34] the transversity induced Λ polarization in SIDIS has been calculated assuming the transversity distribution of the u and d quarks saturating the Soffer bound and in three different scenarios for the fragmentation process:

1. all the Λ spin is carried by the s quark, as from the SU(3) non relativistic quark model. Since h_1^s is assumed to be zero, no polarization is expected;

2. the contribution of the u quark to the Lambda polarization is -20% that of the s quark, as suggested by SU(3) flavor symmetry. In this case the Λ polarization at $x \simeq 0.2$ is about -0.10;

3. all the light quarks give the same contribution to the Λ polarization. This is the most favorable model, and gives a Λ polarization of about +0.20 at $x \simeq 0.2$.

The transverse spin transfer to the Λ, namely the ratio $H_1^{\Lambda/q}/D_1^{\Lambda/q}$ has also been calculated using models. In particular, in reference [35] predictions for the s and u quark $H_1^{\Lambda/q}/D_1^{\Lambda/q}$ have been obtained in the framework of the diquark model. The transverse spin transfer for the s quark increases with z up to $z = 0.5$ and then has a constant value of about 0.75, while for the u quark it increases almost linearly with z assuming a value of about 0.1 at $z = 0.5$.

Of course testing these predictions and giving more input for future calculations has high relevance and constitutes the motivation of this work. COMPASS collected more SIDIS data with the transversely polarised proton target in 2010, corresponding to about twice the 2007 statistics. The analysis of those data, not used yet to measure the Λ and $\bar{\Lambda}$ polarisation, will allow to reduce the final statistical uncertainty by a total factor close to two with respect to the released 2007 results alone.

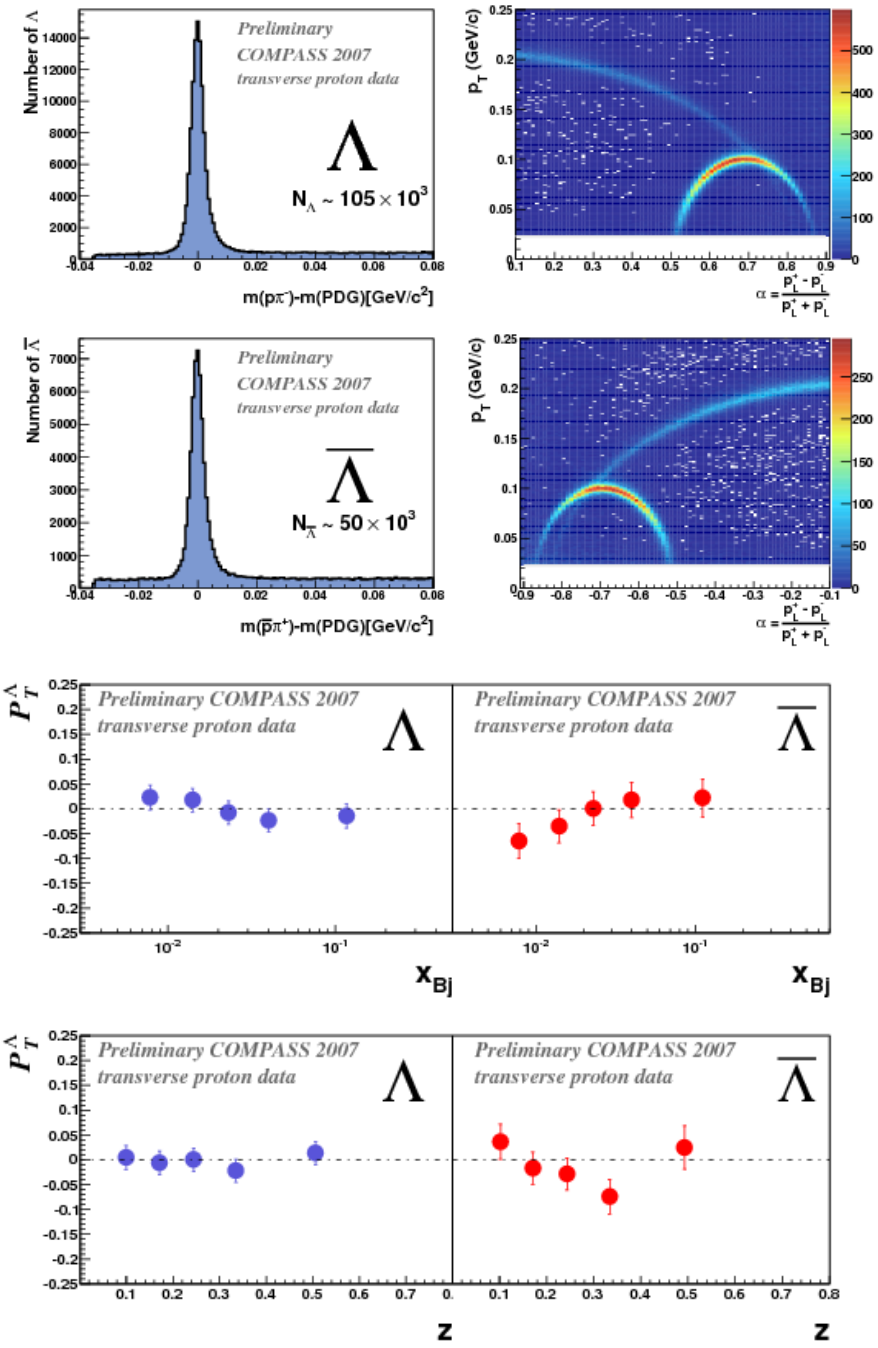

Figure 1.9 COMPASS preliminary results on Λ and $\bar{\Lambda}$ transmitted transverse polarisation from 2007 proton data . The plots in the first row show the invariant mass distributions for the Λ candidates (left) and the corresponding Armenteros plot (right). The second row plots are the same for $\bar{\Lambda}$. The third (bottom) row plots give the Λ and $\bar{\Lambda}$ as function of x and z.

Chapter 2

COMPASS spectrometer

2.1 General overview

COMPASS (*COmmon Muon and Proton Apparatus for Structure and Spectroscopy*) [36, 37] is a fixed target experiment located at the M2 beamline at the *Super-Proton-Synchrotron* (SPS) at CERN in Geneva, Switzerland. Approved in 1997, one of its main physics topics is the investigation of the nucleon structure by using a high energy muon beam and polarised proton and deuteron targets.

Currently, 14 countries with 33 institutes take part at the COMPASS collaboration with a total of about 220 researchers.

The COMPASS spectrometer (Fig. 2.1) is equipped with two dipole magnets, SM1 and SM2, located downstream of the target. Their integrated field strengths are 1.0 Tm and 4.4 Tm respectively and they divide the spectrometer into two main parts. The first one is built around SM1 and is called *Large Area Spectrometer* (LAS). Its design has been studied to detect particles with small momenta and large polar angles to the best. This stage also contains the *Ring Imaging Cherenkov* (RICH) detector for hadron identification. The second stage is called *Small Angle Spectrometer* (SAS) and is located around SM2. Each stage is equipped with trackers which allow to measure charged particles from the maximum acceptance to the beam line, electromagnetic and hadron calorimeters as well as muon walls.

In the first data taking period in 2002–2004 a 160 GeV/c muon beam was scattered off a ^{6}LiD (deuterium) target, which was longitudinally or transversely polarized. In 2005, taking advantage of an SPS shutdown, a general upgrade was performed. The target geometric acceptance was increased by installing a new solenoid magnet; moreover, the two-cells target was replaced by a three-cells target. In parallel, the RICH detector was equipped with new photomultipliers in the central region and new front-end readout electronics for the outer part to improve the particle identification. After the upgrade, in 2006, data were taken with a

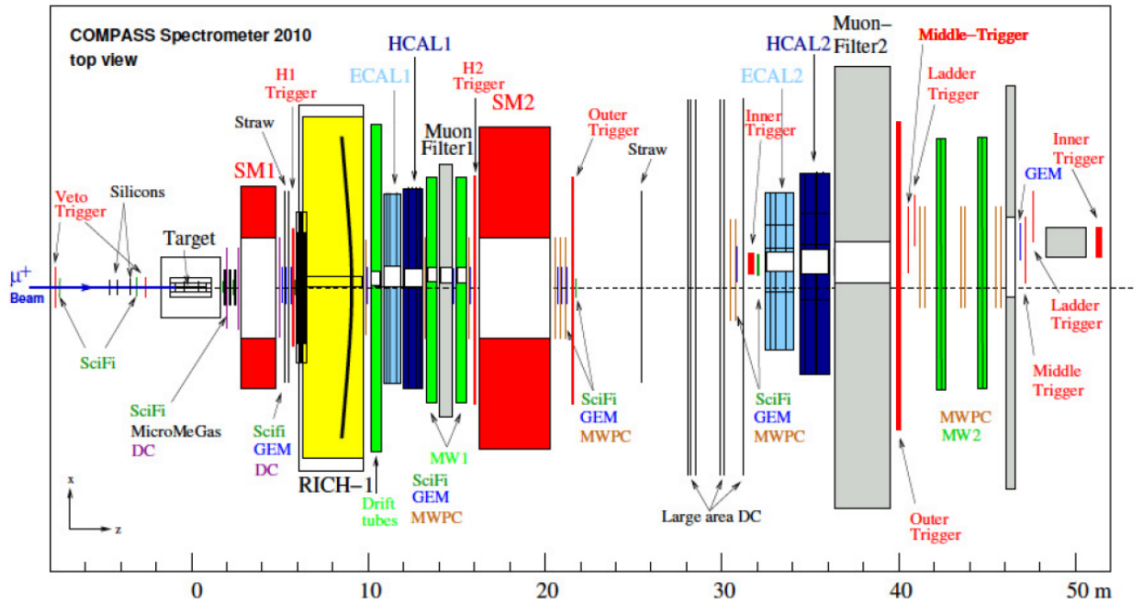

Figure 2.1 COMPASS spectrometer in 2010 setup.

longitudinally polarized ^{6}LiD (deuteron) target. A NH_3 (proton) target was used in 2007, when the running time was equally shared between longitudinal and transverse spin physics, and in 2010, when the NH_3 target was transversely polarised during the whole beamtime. For this analysis, the data collected in 2007 and 2010 with the transversely polarised proton target are used and in the following the experimental setup of the year 2010, very similar to that of 2007, will be described.

Fig. 2.1 schematically shows the COMPASS setup: the laboratory reference frame is defined having the z-axis along the muon beam line entering from the left side, the x-axis and y-axis are on the transverse plane, with the y-axis pointing upward.

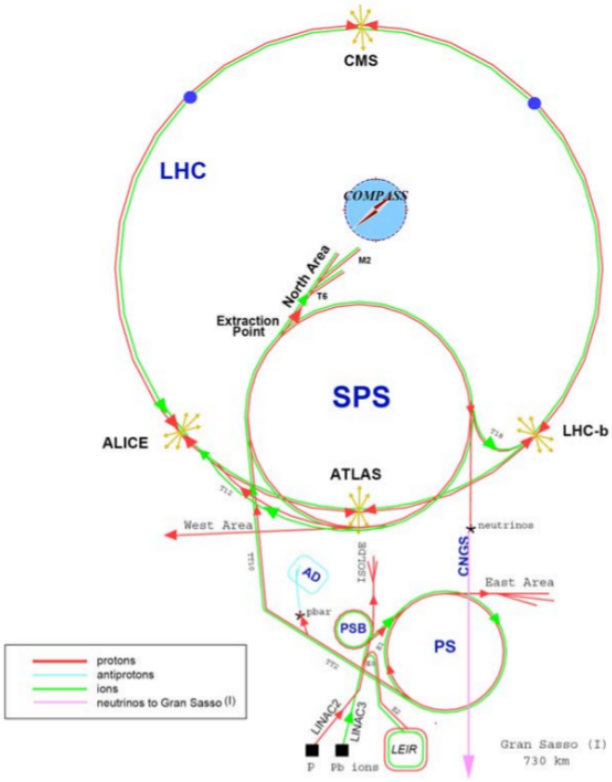

Figure 2.2 The accelerator complex at CERN. The location of the M2 beam line is also indicated.

2.2 Polarised muon beam

The SPS M2 beam line can provide COMPASS with a high intensity μ^+ beam with a momentum up to 200 GeV/c.

The very first stage in the production of the muon beam is the acceleration of a primary proton beam in the *Proton-Synchrotron* (PS in Fig. 2.2) up to a nominal momentum of 14 GeV/c. The produced beam is then injected in the SPS, where its momentum is raised up to 400 GeV/c. The extracted beam is guided onto a 500 mm thick Beryllium production target, named T6. In 2010 the extraction time, called spill, was about 13 seconds with a 9.6 seconds flat top, corresponding to a flux on T6 of around $2.4 \cdot 10^{13}$ protons per spill. The secondary beam coming from the Beryllium target mainly consists of pions. The beam goes through a 600 m long decay tunnel, in which pions can decay into a muon and a muonic neutrino:

$$\pi^+ \to \mu^+ + \nu_\mu . \tag{2.1}$$

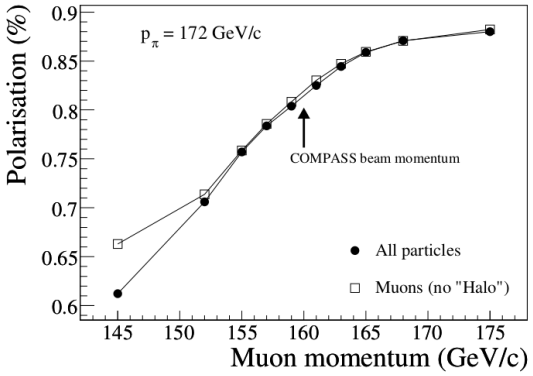

Figure 2.3 The muon beam polarisation (absolute value) as a function of the central muon momentum, assuming a central hadron momentum of 172 GeV/c. [36]

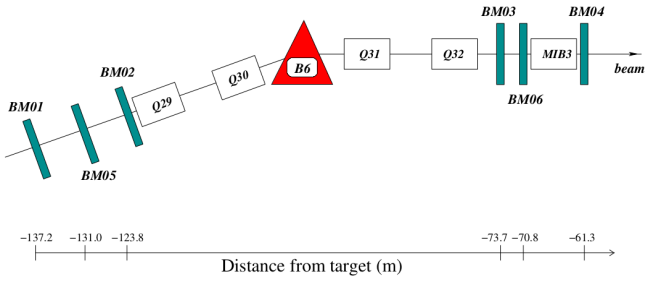

Figure 2.4 Layout of the Beam Momentum Station for the COMPASS muon beam. [36]

Since this decay is parity violating, the muons are naturally longitudinally polarised with a mean polarisation value of -80% in the laboratory system. In general, however, the level of muon polarisation depends on the fraction of the parent hadron momentum carried by the decay muon (Fig. 2.3).

At the end of the decay tunnel the hadronic component of the beam is removed by Beryllium hadron absorbers; each of the nine Beryllium blocks is 1.1 m thick. The desired muon beam momentum is selected by an array of magnetic dipoles and collimators and bent to the horizontal by three dipole magnets (B6).

Before entering the target area the beam is detected by the *Beam Momentum Stations* (BMSs), which consist of four hodoscopes (BM01-BM04) made of scintillating stripes, and two scintillating fibre planes (BM05 and BM06), as shown in Fig. 2.4. The BMS achieves a time resolution of 0.3 ns, a reconstruction efficiency greater than 90% and a momentum resolution better than 1%. Around the muon beam there is a halo, which is made up of muons not properly deflected or absorbed. Within a range of 15 cm from the beam line, the *near* halo accounts for $\sim$16% of the beam intensity; outside this region, the *far* halo still account for

$\sim$7% of the beam intensity. These two components are rejected using a scintillator counter veto system, while the muons in the central region are detected by telescopes of scintillating fibers placed in front of the target.

At last, the beam is focused and steered on the target where it comes with a flux of 3.7 $\cdot 10^{17}$ μ/s, corresponding to about $4 \cdot 10^8$ muons per spill.

2.3 Polarised target

The polarised target is a very important part of the COMPASS experiment since it allows to study the spin structure of the nucleon. It is a solid state target operating in a frozen spin mode and it is the largest in the world having a total length of 120 cm. The target is mainly composed by the polarising magnet, the refrigerating system and the three (or two) cells containing the target material (Fig. 2.5) which can be polarised either on a perpendicular or parallel direction with respect to the beam. The particular design of the target allows for the simultaneous polarisation of the different cells in opposite directions. Moreover, the polarisation state can be periodically reversed: both aspects are particularly useful to reduce systematic effects.

As target material, COMPASS has used ^{6}LiD (polarised deuteron) and NH_3 (polarised proton). The ^{6}LiD target had a dilution factor, that is the scale factor weighing for the non-polarisable components of the target, of $f \sim 0.38$ and a maximum polarisation of $P_T \sim 50\%$. The NH_3 target has a dilution factor $f \sim 0.15$ and an achievable polarisation of $P_T \sim 90\%$. The diameter of the cells is 4 cm; the two outer cells have a length of 30 cm, the inner cell is 60 cm long and they are separated by two 5 cm gaps. The polarisation of the outer cells is the same, and opposite to the one of the inner cell.

The polarization is built up using the technique of the *Dynamic Nucleon Polarization* (for a review see e.g.[38]; for the measurement of polarisation at COMPASS see [39]). The target material is placed inside a microwave cavity in which a microwave frequency modulation is applied at a temperature of 200 mK to 300 mK (Fig. 2.5). The irradiation of the target with microwaves slightly below or above the electron spin (Larmor) resonance frequency transfers to the nucleon the high electron polarisation, obtainable in a magnetic field. This transfer process is called *resonant absorption of microwaves*.

To reach the high polarization needed for the measurement, a strong longitudinal magnetic field of 2.5 T along the beam direction is generated by a superconducting solenoid and the target material must be kept cooled down to a temperature of $\sim$60 mK using a ^{3}He-^{4}He dilution refrigerator. For running the target in transverse mode, i.e. with a nucleon polarisation transverse to the beam direction, a dipole field of $\sim$0.5 T is applied after the polarization is

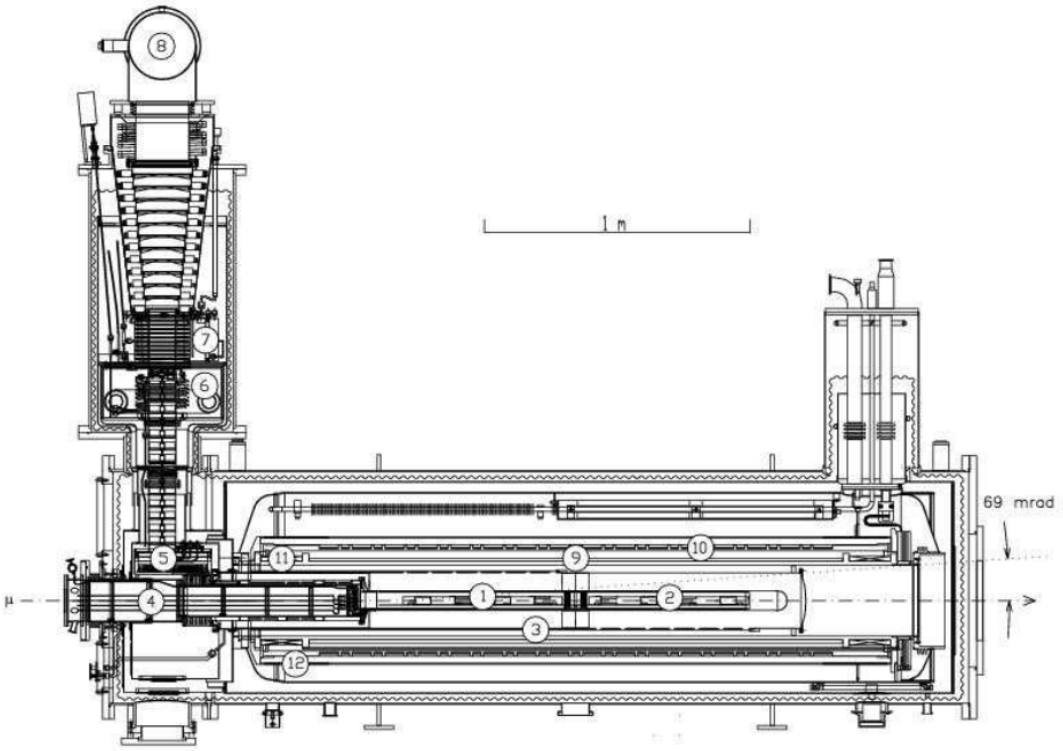

Figure 2.5 Side view of the COMPASS polarised target: (1) upstream target cell and (2) downstream target cell inside mixing chamber, (3) microwave cavity, (4) target holder, (5) still (^{3}He evaporator), (6) ^{4}He evaporator, (7) ^{4}He liquid/gas phase separator, (8) ^{3}He pumping port, (9) solenoid coil, (10) correction coils, (11) end compensation coil, (12) dipole coil. The muon beam enters from the left.

built up. This field bends the direction of the charged particles passing through the target. As a consequence, the reversal of the target polarisation cannot be done by rotating the dipole field, because then the particle tracks would get bend in the other direction and differences in the spectrometer acceptance would increase systematic uncertainties. Therefore, the polarization in transverse mode has to be destroyed and rebuilt again. Reaching a polarization of 90% takes approximately three days and therefore the reversal is only done every five to seven days.

Until 2005, a solenoid was used inherited from the SMC experiment. Its angular acceptance was $\pm$ 70 mrad. In 2005 a new superconducting solenoid magnet was implemented with an angular acceptance of $\pm$180 mrad.

2.4 Tracking system

Different tracking detectors are used to measure particle coordinates in the plane transverse to the beam direction. They are placed along the full length of the spectrometer ($\sim$ 50 m) and have to cope with different working conditions. Near the beam axis the tracking stations have to deal with high particle fluxes and must feature a good time and position resolution. Away from the beam, a larger surface is needed in order to cover the whole region defined by the magnet acceptance, but the requirements on the spatial resolution are less strong. The tracking detectors can be split up in three main classes, depending on the covered angular range: *Very Small Area Trackers* (VSAT), *Small Area Trackers* (SAT) and *Large Area Trackers* (LAT).

2.4.1 Very Small Area Trackers (VSAT)

The tracking stations along the beam axis measure the tracks of the incoming and scattered muon and the particles deflected at very small polar angles up to a radial distance of 2.5 cm. To have a precise reconstruction of the primary vertex coordinates inside the target, ten scintillating fibre (SciFi) stations and three silicon detectors are used.

During the 2010 three SciFi stations were placed in front of the target, while two were placed just behind the target and five inside the spectrometer. Each station consists of at least two planes measuring the X and Y coordinate of the particle track. To guarantee a high efficiency in each plane, the scintillating fibres are stacked in overlapping layers (Fig. 2.6) with the fibres of one column forming one detector channel. The number of layers ranges from two up to seven and the diameter of the fibres used is 0.5, 0.75 or 1 mm, depending on the station. The active area is between 3.9 x 3.9 cm^2 and 12.3 x 12.3 cm^2 . The generated scintillation light is guided to Multi-Anode Photomultiplier Tubes (MaPMTs). The spatial resolution achieved by the SciFis ranges between 130 and 210 μm, depending on the fibre diameter. The time resolution is generally better than 400 ps.

The silicon stations are characterised by a higher spatial resolution. The silicon microstrip stations have an active area of 5 x 7 cm^2 with a spatial resolution of 10 μm and a time resolution of about 2.5 ns. They have a double-sided readout, where the strips on the front are perpendicular to those on the backside: so, one silicon wafer is sufficient for a two-dimensional positioning.

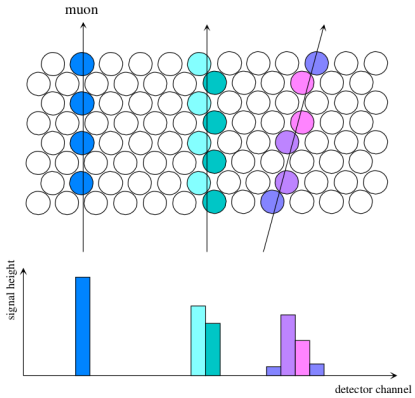

Figure 2.6 Cross section of a typical SciFi plane (top) and signal distribution for different muon incident positions and angles (bottom). One fibre row (e.g. blue) gives one detector channel.

2.4.2 Small Area Trackers (SAT)

The SAT group covers the intermediate region at a radial distance from 2.5 to 40 cm and consists of two types of detectors: MICROMEGAS (*MICROMEsh GAseous Structure* [40]) detectors and GEMs (*Gas Electron Multipliers* [41]). Both detectors have a central dead zone of 5 cm in diameter to avoid high occupancy in the high flux area.

MICROMEGAS is a gaseous detector based on a parallel plate electrode structure and a set of microstrips for readout. The special feature of this detector is the presence of a micromesh which separates the gaseous volume into two regions, the *conversion gap* where ionisation takes place and the *amplification gap* where the avalanche is produced. The field configuration prevents the ions from the avalanche from drifting back into the conversion gap, stopping most of them on the mesh. The ions drift over a maximum distance of 100 μm, corresponding to a time of 100 ns at most. The MICROMEGAS achieve a time resolution of 9 ns with a spatial resolution of 90 μm.

The GEM is a composite grid consisting of two metal layers separated by a thin insulator, etched with a regular matrix of open channels. A GEM grid with the electrodes kept at a suitable difference of potential, inserted in a gas detector on the path of drifting electrons, allows to pre-amplify the charge drifting through the channels. Coupled to other devices, multiwire or microstrip chambers, it permits to obtain higher gains. As in the MICROMEGAS case, the separation of sensitive and detection volumes offers, besides a built-in delay, a strong suppression of photon feedback. Multiple GEM grids assembled in the same gas volume allow to obtain large effective amplification factors in a succession of steps.

The time resolution of the GEMs is 12 ns and the space resolution is 70 μm.

2.4.3 Large Area Trackers (LAT)

The detectors of the LAT cover the region from a radial distance of 15 cm around the beam axis up to the total geometrical acceptance of the experiment. Due to the reduced particle flux in this outermost regions Drift Chambers (DC) [42], Straw Tube chambers [43] and MultiWire Proportional Counters (MWPC) [44] are used.

Four DCs are installed around SM1 and have an active area of 180 x 127 for DC1-DC3 and of 248 x 208 cm^2 for DC4. The central zone, deactivated to avoid high occupancy, has a diameter of 30 cm. The spatial resolution is better than 190 μm. Six drift chambers are installed around SM2 to detect particles deflected at large angles. The covered area is 500 x 250 cm^2 with a large central dead zone of 50 - 100 cm in diameter. The spatial resolution of these drift chambers is 500 μm.

In both stages of the spectrometer straw drift tube detectors are installed. They are made of two layers of thin plastic films; the inner, that consists of a carbon loaded Kapton foil, is glued to the outer one, made of aluminised Kapton. The anode wires are made of gold-plated tungsten and are centered in the tubes. As a fast counting gas a mixture of Ar-CO_2-CF_4 is used. The straw tube chambers cover an overall area of 280 x 323 cm^2 and provide a spatial resolution of 190 μm.

Particle tracking at large angles is mainly done with eleven MWPC stations which have an active area of 178 x 120 cm^2 and reach a spatial resolution of 1.6 mm.

2.5 Particle identification

The COMPASS experiment features several detector types to ensure an efficient identification of the detected particles. A *Ring Imaging Cherenkov* (RICH) counter in the LAS is used to determine the velocity of the particles and to separate them into pions, kaons and protons, covering a momentum range from the Cherenkov threshold (2.5 GeV/c for pions) up to 50 GeV/c. Each stage of the spectrometer is also equipped with an electromagnetic calorimeter (ECAL), a hadron calorimeter (HCAL) and a muon detector.

2.5.1 Calorimeters

Both hadron Calorimeters are placed in front of the muon filters (see Fig. 2.1) and serve two purposes: to measure the energy of the hadrons which are produced in the target material during the scattering process and to trigger on semi-inclusive muon scattering events. The HCALs are sampling calorimeters built with stacks of iron and plastic scintillator plates. Through interactions inside the steel, cascading interactions are produced and detected as hadronic showers in the plastic scintillators.

The electromagnetic calorimeter ECAL2 is positioned just in front of HCAL2 and is made up of 3000 lead glass modules, each corresponding to 16 radiation lengths. A high-energy gamma ray or an electron crossing the lead glass gets fully absorbed, making possible a measurement of its energy. Because of their large interaction lengths, hadrons can not be detected with an electromagnetic calorimeter.

The calorimeters have not been used in this analysis. Still, due to the large amount of material, their presence is quite relevant.

2.5.2 Muon detectors

Identification of the scattered muons is performed using two dedicated muon filters. Each filter includes an absorber layer, preceded and followed by tracker stations (Muon Walls) with moderate space resolution. The absorber is thick enough to stop incoming hadrons. Muons are positively identified when a track can be reconstructed in both sets of trackers placed upstream and downstream of the absorber.

The first Muon Wall (MW1) is located at the downstream end of LAS, in front of SM2. It consists of two stations of squared drift tubes, each with an active area of 4.8 x 4.1 m^2. An iron wall, 60 cm thick, is placed between the two stations; the average tracking efficiency is of $\sim 91\%$ per station.

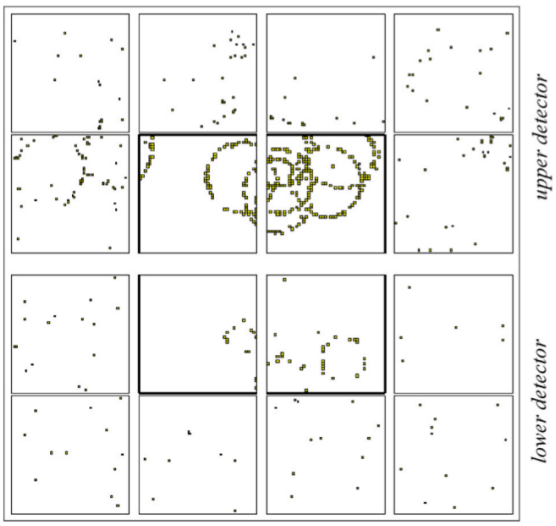

Figure 2.7 A typical RICH event display: many photon rings are visible. The 16 squares represent the photon detector frames. In the central part, equipped with PMTs, there are more photons per ring and the background is lower ([45]).

The second Muon Wall (MW2) is installed at the very end of the spectrometer. The absorber is a 2.4 m thick concrete wall. The charged particle trajectory upstream of the concrete wall is reconstructed by the SAS trackers, while downstream of it there are two dedicated stations of steel drift tubes with an active surface of 4.5 x 2.0 m^2 each. The average tracking efficiency is 82 % per station.

2.5.3 RICH detector

To determine the mass and therefore the type of the hadrons from the momentum measured by the spectrometer the RICH detector (*Ring Imaging CHerenkov*, [45]) is used. The RICH identification is based on the Cherenkov effect: a particle, moving through a medium with a velocity larger than the velocity of light in the same medium, emits photons in a cone symmetric to its direction (Fig. 2.7) [46]. The emission angle of this Cherenkov light, the Cherenkov angle θ_{Ch}, is given by:

$$\cos\theta_{Ch} = \frac{1}{\beta n} \tag{2.2}$$

where n is the refractive index of the medium and $\beta = v/c$. In order to minimise the total amount of material (the RICH is followed by electromagnetic and hadronic calorimeters and by the SAS), a C_4F_10 radiator with n = 1.00153 was chosen. Particles cross 3 m of radiators. The gas pressure and its transparency in a wide wavelength range down to the UV domain,

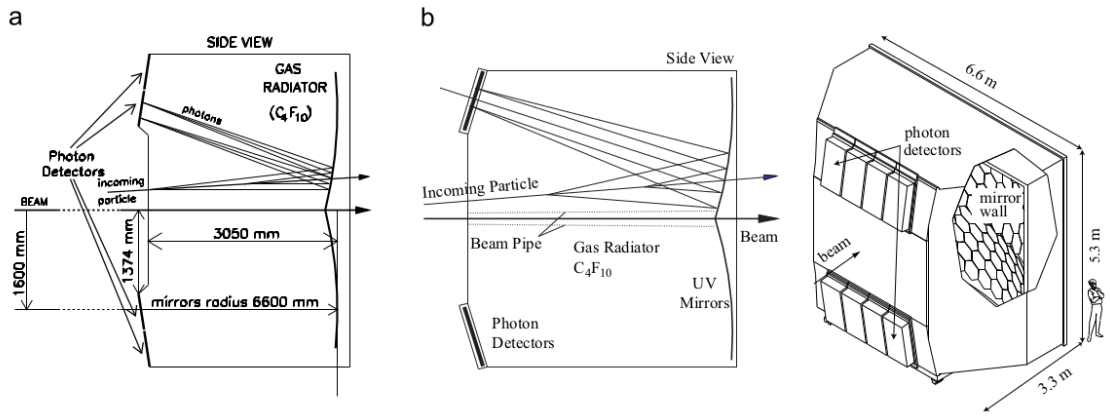

Figure 2.8 A scheme of principle and an artist view of the COMPASS RICH detector.

required by the photon detectors used, are crucial parameters. The radiator gas system [47] allows to keep the pressure constant within 10 Pa and ensures its transparency by continuous filtering.

The threshold momentum required to have Cherenkov emission is obtained from the condition $\beta > 1/n$:

$$\beta_{thr} = \frac{p_{thr}}{\sqrt{p_{thr}^2 + m^2}} = \frac{1}{n} \Longrightarrow p_{thr} = \frac{m}{\sqrt{n^2 - 1}}. \tag{2.3}$$

For pions, kaons and protons the threshold values are about 2.5 GeV/c, 9.5 GeV/c and 20 GeV/c respectively.

The emitted photons are reflected by two spherical mirror systems and focussed on the photon detectors, positioned in the focal plane, resulting in a ring image (Fig. 2.8). The mirror wall has a surface of 21 m^2 and is formed by a mosaic arrangement of 116 spherical UV mirror elements [**?**]. From the radius of this ring the Cherenkov angle and the corresponding velocity are extracted.

In the years 2001-2004 multi-wire proportional chambers (MWPCs) equipped with CsI photocathodes were used as photon detectors. After the 2005 upgrade in the central region of the RICH the use of Multi-Anode Photomultipliers (MAPMT) replaced both the detection and the read-out system, leading to a suppression of the uncorrelated background signals due to the high time-resolution (< 1 ns) of the MAPMTs. In the external part of the RICH the existing read-out of the MWPCs was replaced by APV chips leading also to an improved time-resolution.

2.6 Trigger system

The task of the trigger system is to select physical event candidates in a high rate environment with very fast decision and low dead time and provide a read-out signal to the front-end electronics of the detectors [48].

The COMPASS trigger system is based on the detection of the scattered muon. It consists of four scintillating hodoscope stations covering different kinematic regions (“inner” (IT), “middle” (MT), “ladder” (LT) and “outer” (OT)), two scintillating veto stations upstream of the target and uses the hadronic calorimeters. The position of the trigger components is shown in Fig. 2.9.

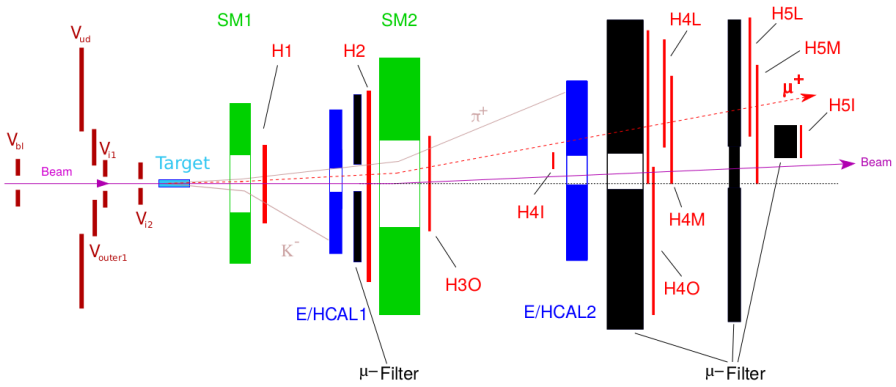

Figure 2.9 Position of the trigger elements: LAST (H1, H2), IT (H4I, H5I), MT (H4M,H5M), LT (H4L, H5L), OT (H3O, H4O), Vetos and the hadron calorimeters.

To cover the different kinematic regions of the COMPASS physics program, different trigger concepts are applied. For triggering events from the high Q^2 region ($Q^2 > 1$ (GeV/c)^2), the muon scattering angle in the non-bending plane is measured with the “ladder” and “outer” hodoscopes and compared in coincidence matrices to ensure that the muon is coming from the target region (Fig. 2.10). Additionally, the veto system is used to identify muons coming from the beam halo. The trigger signal coming from the coincidence matrix is also put in coincidence with the calorimeter signals and a trigger signal ("semi-inclusive trigger") is generated if the energy loss is above a certain threshold.

In 2010, starting with period W31, a fifth hodoscope trigger station was integrated into the system. The so-called Large Angle Spectrometer Trigger (LAST) consists of two hodoscopes installed in the LAS, the first one in front of the RICH, the second one behind Muon Filter 1. The LAST extends the existing muon trigger acceptance towards large Q^2.

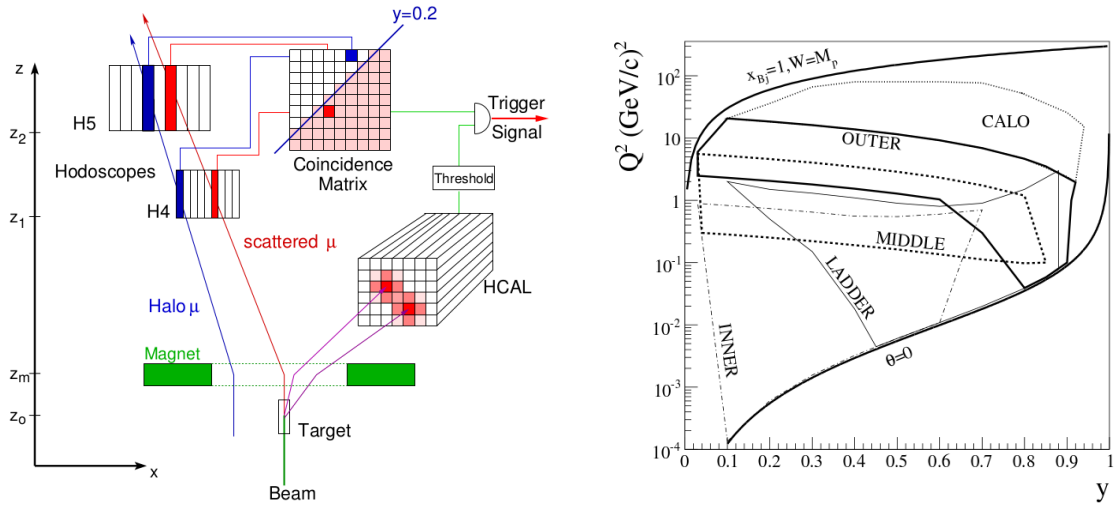

Figure 2.10 Left: basic scheme of the trigger decision. The scattered muon leads to a coincidence in the activated area of the coincidence matrix; the halo muon fails to do so because its track do not point back to the target. Right: the kinematic coverage in y and Q^2 for the four hodoscope trigger subsystems and the standalone calorimetric trigger.

2.7 Data acquisition system and event processing

At COMPASS the Data Acquisition (DAQ) [49] system has to handle the information of more than 250000 detector channels with a typical event size of 45 kB at a trigger rate of about 10kHz. Moreover, the trigger signals are mainly created by hodoscope signals at the downstream end of the spectrometer. Therefore, a special pipeline and a nearly dead-time free readout scheme is necessary developed.

A schematic view is shown in Fig. 2.11.

The pipeline concept consists of digitising and buffering all signals close to the respective recording detectors. The data registration is performed by the Front-End (FE) boards. In this procedure a time delay is created which allows the trigger to decide whether the signal is interesting or not. This basis procedure is the same for all detectors expect for the calorimeters, which send their signal through long delay cables until the trigger decision is received. The signal is digitised over the CATCH (*Compass Accumulate Transfer and Control Hardware*) readout modules. The CATCHs use the trigger signals generated by the Trigger Control System (TCS) to build local subevents and also provide the TCS timing signal to the connected FE-boards. From the CATCHs the signals are transferred to readout buffer via optical fibres, where the data are stored on spill-buffer PCI cards. In the break between two spills the data are processed in the Event Builder (EB). The events are written to multiple 1 GB large files (chunks) labelled by the run number and their consecutive chunk

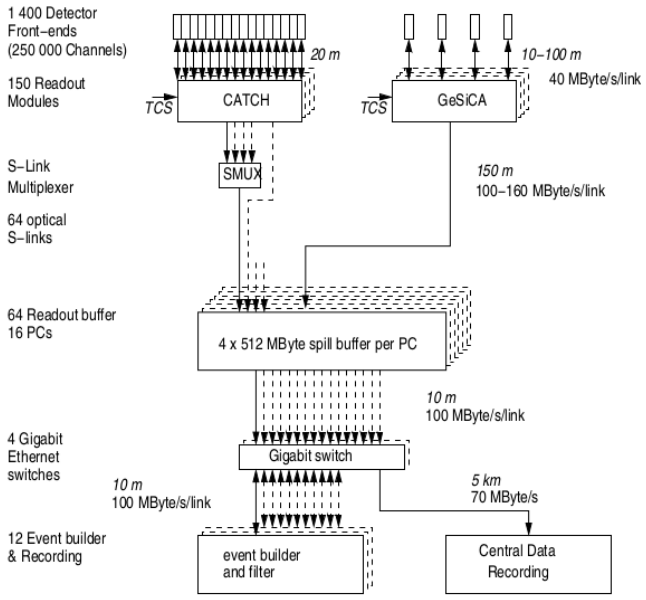

Figure 2.11 Schematic view of the COMPASS DAQ system. The data of the detector front-ends are readout by CATCH and GeSiCA modules, buffered and sent to the event builders. The files containing the final events are transferred afterwards to the CERN computer center.

number. These files are transferred to the CERN central data recording system to be finally stored on tape at the CERN Advanced STORage system (CASTOR).

As soon as the configuration information (calibrations, alignment) of each detector is available, the raw data can be processed. CORAL (COmpass Reconstruction and Anaysis Framework) decodes the recorded data and provides additional information such as vertex positions, particle tracks and RICH information. The additional information also allows the further reduction of data volume based on physics quantities, thus, the data can afterwards be processed faster. The processed data are stored in a mDST (mini Data Summary Tape) format. The investigation of physics signatures of the mDST's is conducted with the PHAST (PHysics Analysis Software and Tools) software package. Both CORAL and PHAST have been developed by the COMPASS collaboration.

Chapter 3

Data analysis

3.1 Data sample and stability

The aim of the present work is the measurement of the tranversity transmitted polarisation of the Λ ($\bar{\Lambda}$) produced in SIDIS off transversely polarised protons using the 2010 data. Since some aspects of the analysis are new, the 2007 data have also been analysed. For both datasets the mDST filtered for the measurement of the K^0_s Collins and Sivers asymmetries [50] have been used in order to reduce required storage space and CPU time. The same data selection, based on data quality and stability, has been done: in particular, the same bad spills and bad runs have been excluded. They are defined by looking at the time stability of several quantities like the average number of primary vertices, beam tracks, secondary tracks, the number of tracks associated with the primary vertex and the number of secondary vertices. As will be clear in the following, the stability of the spectrometer performance is an essential requirement to avoid systematic effects and the applied data selection is the result of studies performed since a long time.

In the next section the selection of the DIS events and of the Λ candidates will be described. The last section of this chapter is dedicated to the measurement of the Λ polarisation. All the plots have been produced using the 2010 data and are very similar to the ones obtained from 2007 data.

3.2 Selection of DIS events

The DIS events are selected with a standard procedure. The first requirement is the presence of a primary vertex (PV) defined by at least one incoming and one outgoing muon tracks. Further requirements are the following:

- The reduced χ^2 of the incoming and outgoing muon tracks satisfies $\chi^2_{red} < 10$;
- The incoming muon momentum is in the range: 140 GeV/c < $beam_{mom}$< 180 GeV/c and artifacts (momenta artificially put to 160 GeV/c when badly reconstructed) are rejected;
- The incoming muon track crosses all the target cells: this ensures that the flux is the same for all cells;
- The outgoing muon traverses 30 radiation lengths ($X/X_0 > 30$, where X depends on the atomic and mass numbers of the crossed material) and its first hit is in front of SM1 ($Z_{first} < 350$ cm). The first condition cannot be satisfied by hadrons; the second is necessary to have a good track reconstruction;
- The PV reconstructed position is inside one of the target cells (Fig. 3.1).

The cuts on the reconstructed kinematic variables are:

- The squared momentum transfer must satisfy the condition $Q^2 > 1$ (GeV/c)^2;
- The Bjorken variable x lays in the range (0.003,1);
- The final state hadronic mass W must be larger than 5 GeV/c^2 to reject hadron resonances and to be in the DIS region;
- The energy transfer ratio y must be in the range $0.1 < y < 0.9$. Events with low y are outside the DIS domain and, being small the difference of the incoming and outgoing muon energies, they suffer from poor reconstruction efficiency. On the other hand, events with large y are affected by radiative effects: since their systematic is too large to be included, they are discarded.

3.3 Selection of Λ and $\bar{\Lambda}$ candidates

The Λ hyperon, being a neutral particle, can not be directly detected in the spectrometer. It is identified by the detection of the charged particles produced in its weak non-leptonic decay $\Lambda \longrightarrow p\pi^-$ which has a branching ratio $BR = 63.9\%$ [18].

The mean life of the Λ particle is $\tau = (2.632 \pm 0.020) \cdot 10^{-10}$ s, thus in the majority of the cases the decay position (secondary vertex, SV) is far enough from the production vertex (primary vertex, PV). The Λ shows up as a pair of opposite charged particles "created" in a position downstream the PV with no track connecting the SV to the PV, namely as a "V^0".

For each DIS event, the Λ candidates selection is performed in three steps:

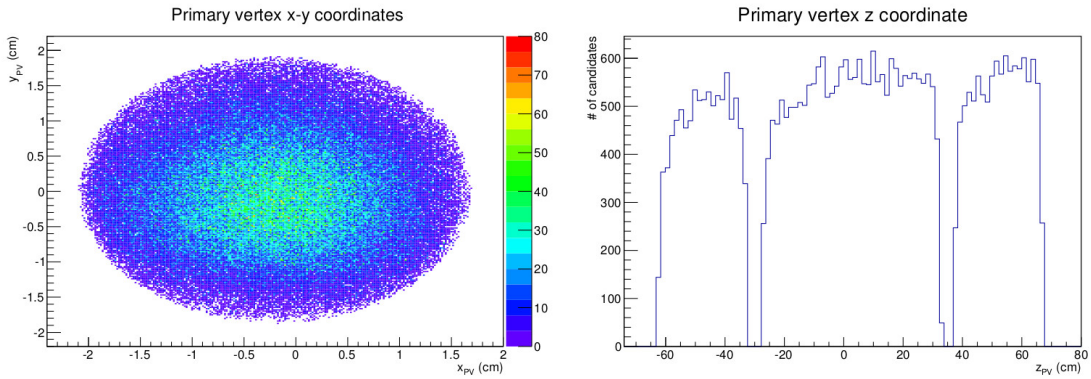

Figure 3.1 On the left: the *x*-*y* coordinates of the primary vertex: the asymmetry is due to the magnetic field that bends the incoming muon track. On the right: z position of the primary vertex, inside the three cells.

- Background rejection with kinematic cuts;
- Background rejection using the RICH detector;
- Mass cut to select only Λ candidates inside a proper invariant mass interval,

described in the following.

3.3.1 Kinematic cuts

To select Λ candidates, the following cuts have been applied to the reconstructed V^0s:

- The number of outgoing particles is 2 and they have opposite charge;
- Both outgoing tracks are not associated to any primary vertex. This is not the same as asking that the tracks come from a secondary vertex, since the reconstruction algorithm can in principle associate each of them to several primaries;
- The secondary vertex must be downstream of the primary vertex ($z_{SV} > z_{PV}$);
- The outgoing particles must be hadrons, i.e. the radiation lengths associated to their tracks must be $X < 10X_0$;
- The reduced χ^2 for both tracks satisfies $\chi^2_{red} < 10$;
- Both tracks do not cross the yoke of SM2, where the magnetic field is not implemented in CORAL;

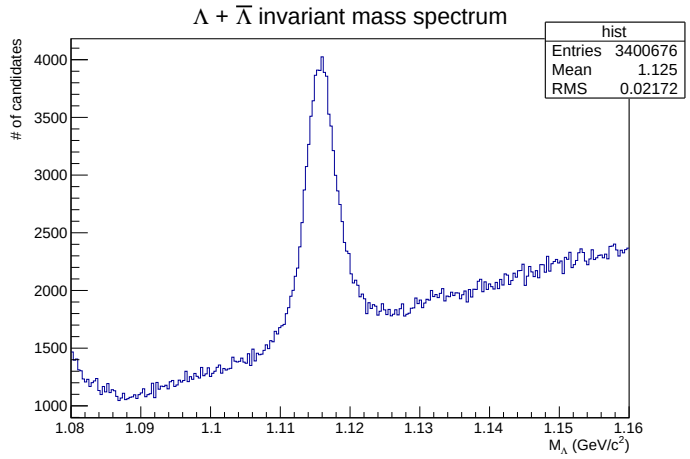

Figure 3.2 First reconstructed $\Lambda + \bar{\Lambda}$ invariant mass spectrum: a large background still present.

- The momenta of both decay particles must be larger than 1 GeV/c to have an adequate track and vertex reconstructions;
- The last measured hit of both tracks has a z coordinate larger than 350 cm and smaller than 3300 cm, i.e. between SM1 and SM2. This ensures that the momenta of the decay particles are reconstructed with sufficiently high resolution.

After these cuts, a large background is still present in the sample. This is clear when looking at the invariant mass distribution of the pair of particles from V^0, shown in Fig. 3.2 and defined as:

$$M_{inv} = \sqrt{(E_1 + E_2)^2 - (\vec{p}_1 + \vec{p}_2)^2} \tag{3.1}$$

where E_i and $\vec{p}_i$ ($i = 1, 2$) are the energy and momentum of the daughter particles. Energies are calculated from the measured momenta and under the hypotheses that both the daughter particles are pions (K^0_s case) or assuming them to be a proton-pion pair ($\Lambda/\bar{\Lambda}$ case). For each V^0, both options are taken into account.

Two further kinematic cuts are applied. The first one is a cut on the *collinearity angle* θ_{coll}, defined as the angle between the reconstructed Λ candidate direction $\vec{p}_\Lambda$ and the vector $\vec{v}$ linking the primary and the secondary vertices:

$$\theta_{coll} = \arccos\left(\frac{\vec{p}_\Lambda \cdot \vec{v}}{|\vec{p}_\Lambda||\vec{v}|}\right) \tag{3.2}$$

and illustrated in Fig. 3.3.

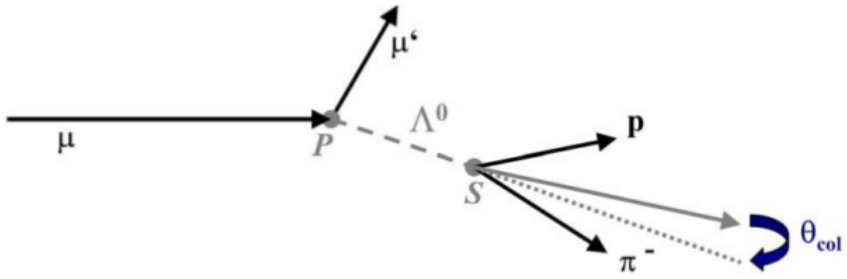

Figure 3.3 The collinearity angle, defined upon the decay particles momenta and the vector linking primary and secondary vertices.

The collinearity angle distributions, for $\theta_{coll} < 350$ mrad and $\theta_{coll} < 20$ mrad are reported in Fig. 3.4. The requirement θ_{coll}<7 mrad favours the selection of V^0s stemming from the primary vertex.

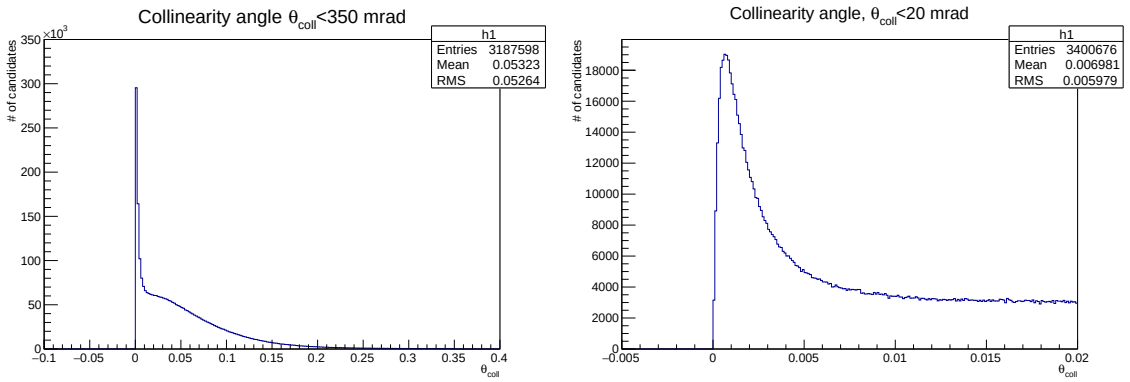

Figure 3.4 Collinearity angle distributions for the two cases: $\theta_{coll} < 350$ rad (left) and $\theta_{coll} < 20$ mrad (right). Note the different scales.

The second requirement is on the transverse momentum p_T of the positive decay particle with respect to the V^0 momentum, that has to be larger than 23 MeV/c in order to remove a large background due to the photon conversion $\gamma \to e^+e^-$. The p_T spectrum, obtained after the collinearity cut, shows the contributions of background and Λs. On a first sight, it seems that the request for p_T to be larger than 50 MeV/c could eliminate the largest part of background, but such cut would be too much severe. The p_T vs M_{inv} scatter plot (Fig. 3.5, right), in fact, allows to recognise that the separation line between the Λ branch and the background band from which it emerges clearly lays at 23 MeV/c. A cut at 50 MeV/c would reject background events outside the Λ invariant mass interval, as well as too many good Λ candidates.

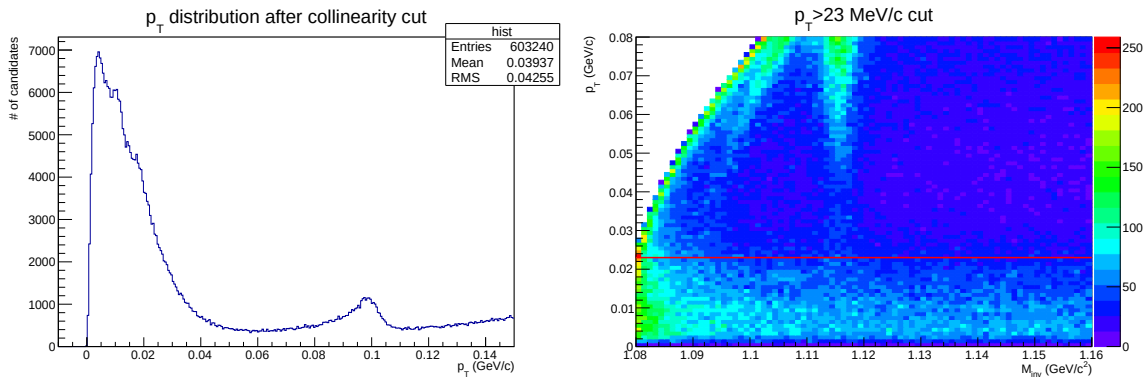

Figure 3.5 Left: p_T distribution after the collinearity cut: the background contribution at small p_T and the Λ-K^0_s superposition region at $p_T \sim 100$ MeV/c are well visible. Right: p_T vs M_{inv} scatter plot: Λs lay on the vertical branch and a red line indicates the cut value. Also the K^0_s branch can be recognised on the left of the Λ branch.

The effect on the reconstructed invariant mass spectrum of the collinearity and p_T cuts is clear looking at Fig. 3.6, where the spectra obtained before and after their application are compared. A further improvement of the analysis is guaranteed by the construction of the Armenteros plot, thanks to which the sample composition can be studied.

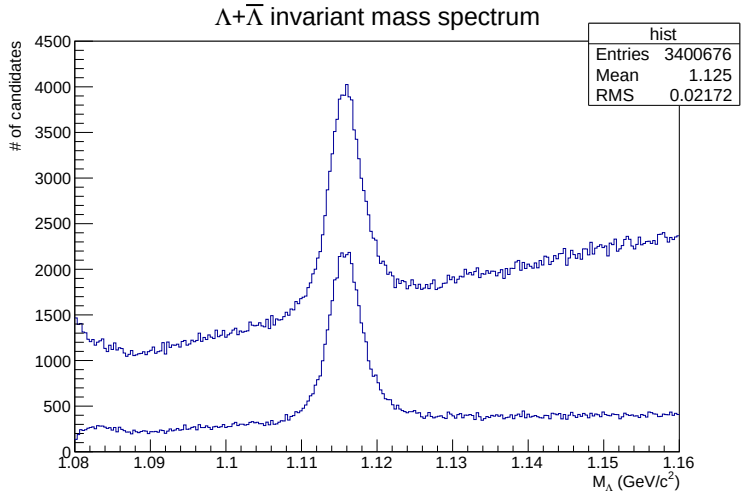

Figure 3.6 Effects on the reconstructed $\Lambda + \bar{\Lambda}$ invariant mass spectrum of the cuts on θ_{coll} and on p_T: a large amount of background events gets removed.

3.3.2 Armenteros-Podolanski plot

The Armenteros-Podolanski plot [51, 52] is a powerful tool introduced in the 50's to analyse and recognise V^0 particles. We indicate with M the mass of the V^0 particle and with $\vec{P}$ its momentum in the laboratory reference system; the vectors $\vec{p}_i$ and m_i, with $i = 1,2$, are the momenta in the laboratory reference system and the masses of the daughter particles, being m_1 the mass of the positive one. The variables considered in the Armenteros construction are two: the transverse momentum p_{iT} of one of the two daughter particle with respect to $\vec{P}$ and the asymmetry in the longitudinal momentum component of both, commonly indicated as α:

$$\alpha = \frac{p_{1L} - p_{2L}}{p_{1L} + p_{2L}}. \tag{3.3}$$

With reference to Fig. 3.7, θ is the emission angle of particle 1, while $\vec{p}^*$, E_1^* and E_2^* are the momenta and energies of the decay particles in the center of mass system (CMS).

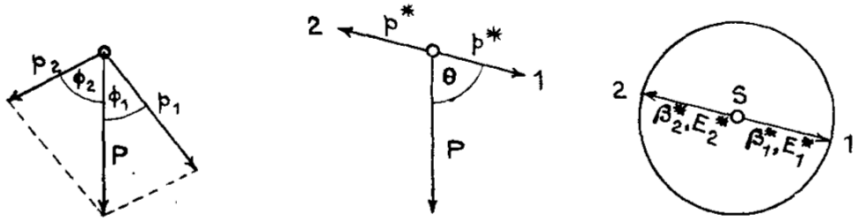

Figure 3.7 Left: decay in the laboratory system. Center and right: decay in the CMS.

After a Lorentz transformation from the laboratory to the CMS, the longitudinal and transverse components of the daughters momenta are given by:

$$\begin{aligned} p_{1L} &= \gamma p^* \cos\theta + \beta\gamma E_1^*, \qquad & p_{1T} &= p_T = p^* \sin\theta; \\ p_{2L} &= -\gamma p^* \cos\theta + \beta\gamma E_2^*, \qquad & p_{2T} &= p_T = p^* \sin\theta. \end{aligned} \tag{3.4}$$

where $\beta = v/c$ and $\gamma = 1/\sqrt{1-\beta^2}$. Introducing the quantity $\alpha^* = (E_1^* - E_2^*)/M$, the longitudinal asymmetry can be written as:

$$\alpha = \frac{p_{1L} - p_{2L}}{p_{1L} + p_{2L}} = \frac{2\gamma p^* \cos\theta + \beta\gamma(E_1^* - E_2^*)}{\beta\gamma M} = \frac{2p^* \cos\theta}{\beta M} + \alpha^*. \tag{3.5}$$

A simple rearrangement of the terms leads to:

$$p^* \cos\theta = \frac{\beta M}{2}(\alpha - \alpha^*) = \frac{\beta\gamma M}{2\gamma}(\alpha - \alpha^*) = \frac{\alpha - \alpha^*}{2\sqrt{1/P^2 + 1/M^2}}. \tag{3.6}$$

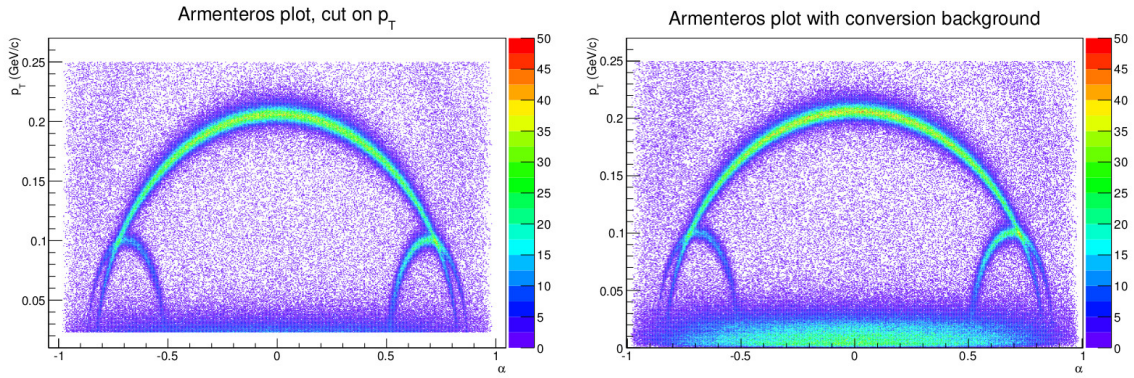

Figure 3.8 Armenteros plots for the Λ candidates without (left) and with (right) the cut $p_T > 23$ MeV/c used to reject background from $\gamma \to e^+e^-$

This equation, once squared and summed to $p_T^2 = p^{*2}\sin^2\theta$, yields the equation of an ellipse:

$$p_T^2 + \frac{(\alpha-\alpha^*)^2}{4(1/M^2)} = p^{*2} \tag{3.7}$$

when assuming $1/P \sim 0$, which is a good approximation in high-energy regimes. The expression for p^* is fixed by the values of the three masses:

$$p^* = \frac{1}{2M}\left[M^2-(m_1+m_2)^2\right]^{1/2}\left[M^2-(m_1-m_2)^2\right]^{1/2}, \tag{3.8}$$

thus, different V^0s lay on ellipses of different shapes: this is a major result, since their identification gets strongly simplified. Note that, if $m_1 = m_2$, $\alpha^* = 0$ and the center of the ellipse is (0,0) on the (α,p_T) plane, while if $m_1 \neq m_2$ the center has coordinates (0,α^*). Thus, while K_s^0s lay on a centered elliptical distribution, Λ and $\bar{\Lambda}$ ellipses are mirrored with respect to the $\alpha^* = 0$ axis, the former on the right part of the Armenteros plane, the latter on the left. This can be seen rewriting the α^* quantity in the following way:

$$\alpha^* = \frac{E_1^*-E_2^*}{M} = \frac{(E_1^*-E_2^*)(E_1^*+E_2^*)}{M(E_1^*+E_2^*)} = \frac{m_1^2+p^{*2}-m_2^2-p^{*2}}{M^2} = \frac{m_1^2-m_2^2}{M^2} \tag{3.9}$$

which is greater than zero if the positive particle is also the heaviest, that is the case for Λs, while the reverse apply to $\bar{\Lambda}$s.

The Armenteros plot, after all the kinematic cuts described in the previous section, is shown in Fig. 3.8 (left). As can be seen, the V^0 sample consists in K_s^0s, Λs and $\bar{\Lambda}$s. The effect of the cut $p_T > 23$ MeV/c is clear when looking at Fig. 3.8 (right) obtained without this cut. The $\gamma \to e^+e^-$ background shows up as the band at small p_T.

A cut on $\alpha > 0$ or $\alpha < 0$ selects the region in the Armenteros plot where Λs or $\bar{\Lambda}$s are expected. In this way, the invariant mass spectrum shown in Fig. 3.6 can be split into two contributions, according to the sign of α (Fig. 3.9).

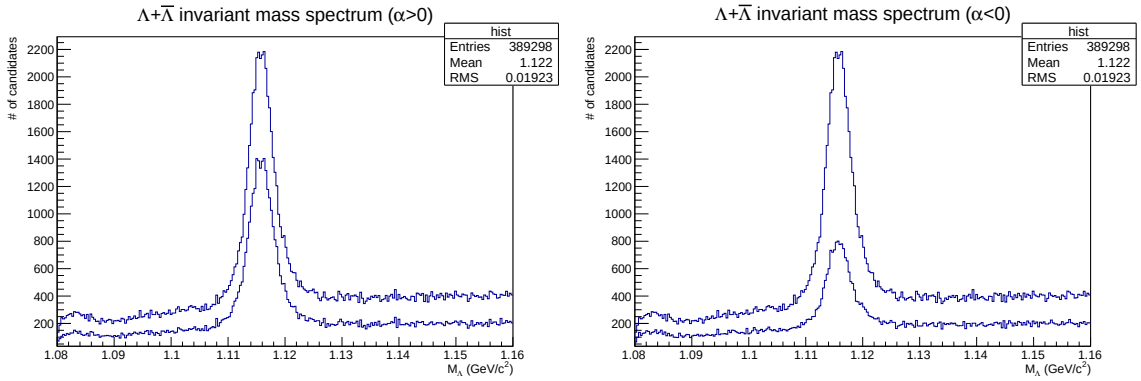

Figure 3.9 The invariant mass spectrum after all kinematic cuts (p_T and θ_{coll} included), split in the complementary cases: $\alpha > 0$ (left) and $\alpha < 0$ (right).

As shown in Fig. 3.8 and more effectively in Fig. 3.10, the Λ and $\bar{\Lambda}$ elliptic branches and the background K^0_s events overlap at $p_T \sim 100$ MeV/c. At first sight, a cut on α and p_T seems to be a good solution to select only the interesting V^0s. Unfortunately, this cut would not remove the background in the Λ mass peak and make the parametrisation of its shape more complicated, as can be seen in Fig. 3.10 (right). This selection method will then be avoided.

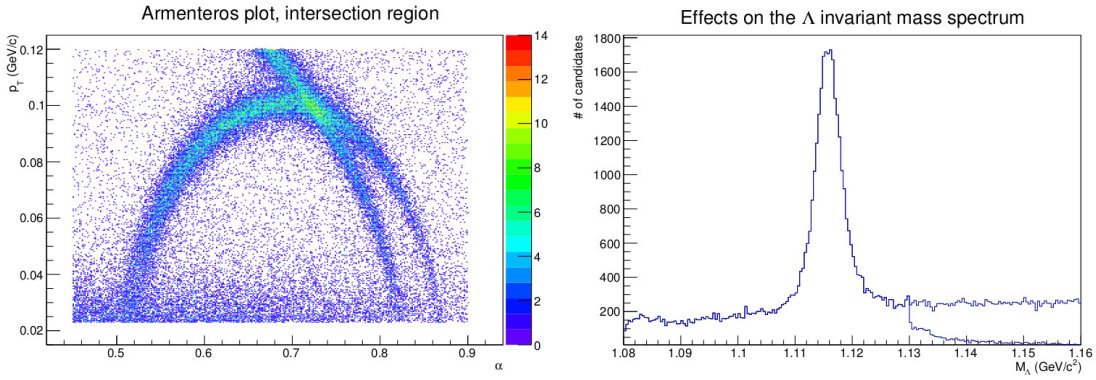

Figure 3.10 Left: the superposition region at $p_T \sim 100$ MeV/c. Right: the effect on the invariant mass spectrum of a cut on the Armenteros p_T, α plane.

The plots in Fig. 3.10 give an insight into the correlation between high transverse momenta and high reconstructed Λ masses. To investigate such correlation, an useful possibility is offered by a *mass extension* of the Armenteros plots, where the reconstructed Λ or K^0_s are reported on the third axis.

The three quantities p_T, α and the invariant mass define a surface, always symmetric with respect to the $\alpha = 0$ vertical plane (Fig. 3.11). The K^0_s contribution to the Λ invariant mass is more pronounced for high p_T, where the number of K^0_s candidates is larger: for this reason, a cut on p_T removes high Λ invariant masses, while the K^0_ss at smaller p_T, contributing to small masses, are kept.

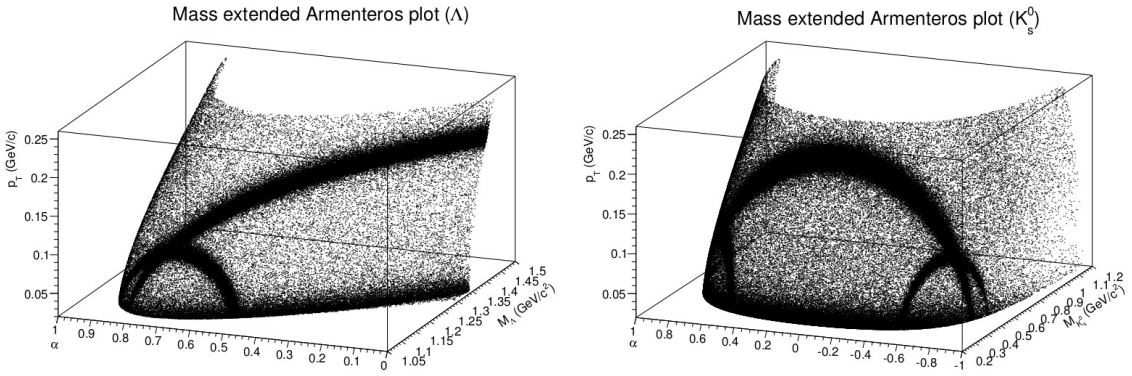

Figure 3.11 *Mass extended* Armenteros plots for Λ ($\alpha > 0$, on the left) and for K^0_s (on the right).

The selection of an interval of p_T values on the *mass extended* plots results in a symmetric shape in the K^0_s case and in a double, rotated parabolic shape for Λs. This means that a cut on the Λ invariant mass selects asymmetric arcs on the Armenteros ellipses (Fig. 3.12).

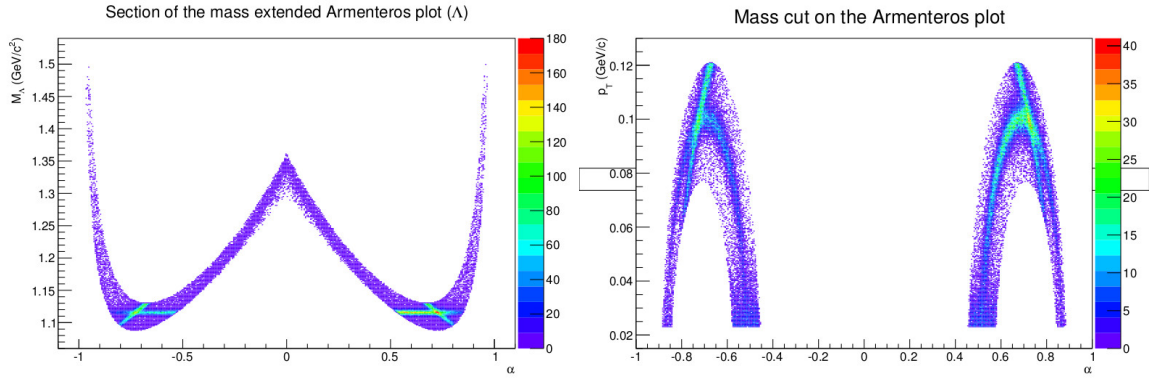

Figure 3.12 Left: section at 50 MeV/c<p_T<100 MeV/c of the Λ *mass extended* Armenteros plot. Right: effects of a cut on the reconstructed Λ mass: two elliptic arcs with asymmetric widths survive.

In order to eliminate the K^0_s background while not imposing too strict limitations on the Λ and $\bar{\Lambda}$ signal sample, the RICH detector has been used. The procedure will be described in the following section.

3.3.3 Use of the RICH detector

The RICH detector allows to identify electrons, pions, kaons and protons in a momentum range from threshold ($\sim$ 10 MeV/c, 2.5 GeV/c, 9.5 GeV/c and 17 GeV respectively) to 50 GeV/c, where the Cherenkov angles of pions and kaons become nearly independent on momentum and a reliable distinction between them is no more possible (Fig. 3.13).

To identify the Λ candidates among the V^0s, it seems convenient to look for the decay protons (correspondingly, antiprotons for $\bar{\Lambda}$): searching for pions as daughter particles, in fact, would not remove the K_s^0 background. However, a direct proton identification would drastically reduce the available statistics because of its high Cherenkov threshold. For this reason, the usual strategy consists in the rejection of all those V^0 events in which an electron, a pion or a kaon has been identified, while a proton was expected.

The particle identification (PID) is performed using an algorithm based on the maximum likelihood method, briefly described in the following. If the particle momentum p and the refractive index n are known, for a particle of mass M, the expected Cherenkov angle is given by:

$$\cos\theta_M = \frac{1}{\beta n} = \frac{\sqrt{p^2+M^2}}{np}. \tag{3.10}$$

The (extended) likelihood function for each mass hypothesis M is written as [45]:

$$\mathscr{L}_M = \exp[-(S_M+B)] \prod_{j=1}^{N} f_M(\theta_j,\phi_j) \tag{3.11}$$

where N is the number of photons and θ_j and ϕ_j are the polar and azimuthal photon angles. The function f_M is made up of a signal and of a background term:

$$f_M(\theta,\phi) = s_M(\theta,\phi) + b \tag{3.12}$$

and s_M has a gaussian shape of the kind:

$$s_M(\theta_j,\phi_j) = \frac{S_0}{\sqrt{2\pi}\sigma_{\theta_j}} \exp\left[-\frac{1}{2}\frac{(\theta_j-\theta_M)^2}{\sigma_{\theta_j}^2}\right] \varepsilon_D(\theta_j,\phi_j) \tag{3.13}$$

where $\varepsilon_D(\theta_j,\phi_j)$ is the photon probability to reach the detector. According to the Frank-Tamm law, moreover, $S_0 = N_0 \sin^2\theta_M$, being N_0 the number of expected photons at saturation ($\beta \to 1$). The term σ_{θ_j} is the single-photon resolution, calibrated on data.

$\mathscr{L}_M$ is calculated for five mass hypotheses (e, μ, K, π, p) and for the background hypothesis. At first order the maximum of the six $\mathscr{L}_M$ values can be assumed to correspond

to the good hypothesis. More refined procedures requires the comparison between different values, so that a mass hypothesis is accepted when its ratio with the second highest likelihood or with the background is higher than a proper value.

Note that the $\exp(-B)$ term (Eq. 3.11), entering each $\mathscr{L}_M$ value in the same way for each mass hypothesis, is not influential at all.

The PID is performed in CORAL and the relevant information for each track is saved in the mDSTs. The PHAST **GetLike** function returns the six likelihood values for each particle. The rough identification, made assuming that the highest likelihood value corresponds to the correct mass hypothesis, is implemented in the **LikePid** PHAST function that returns the code (*tag*) of the particle with the highest likelihood according to the scheme:

- $0 \rightarrow$ pion;
- $1 \rightarrow$ kaon;
- $2 \rightarrow$ proton;
- $3 \rightarrow$ electron;
- $4 \rightarrow$ muon;
- $5 \rightarrow$ background.

Actually, the tag number 3 (electron) is inhibited for momenta over 8 GeV/c and the muon tag is never used. A tag equal to -1 is set if no RICH information is available or if the momentum is higher than 50 GeV/c because of the bad pion/kaon separation.

To reliably identify a particle (in order to reject it, in our case), a selection must also be performed on the ratio:

$$LH(\textit{particle to be identified})/LH(\textit{background}).$$

So, to attribute a mass hypothesis M to a particle X, two conditions must be verified at the same time:

- among all the six likelihoods calculated for X, the value for M is the highest;
- the ratio $LH(M)/LH(background)$ must be greater than a certain value k.

If one of the two conditions can not be satisfied for any M, the particle is not identified. A correction to this procedure will be explained in the following.

The set of k values, which strictly depend on momentum, has been evaluated for the analogous analysis of Λ and $\bar{\Lambda}$ transverse polarisation performed using COMPASS 2007 data and are given in Tab. 3.1 and Tab. 3.2. The likelihood cuts were tuned searching for the smallest statistical uncertainty on the number of Λ candidates in any momentum region, equivalent to the maximum of the corresponding *Figure of Merits* (FoMs), defined as:

$$FoM = \frac{S^2}{S+B} \tag{3.14}$$

where *S* means *signal* and *B background* as calculated on the Λ invariant mass spectrum. The same *k* values have been used for the 2010 data analysis since the *FoM* has a weak dependence on *k* and the RICH performances in 2007 and 2010 were very much the same.

Table 3.1 Summary of **RICH Λ cuts** to identify positive electrons e^+, pions π^+ and kaons K^+ to be rejected.

Momentum range	**Identification of**	**Likelihood cut**
Thr(π)<p<Thr(K)	e^+	LH(e)/LH(bk)>2.3
	π^+	LH(π)/LH(bk)>2.2
Thr(K)<p<Thr(p)	π^+	LH(π)/LH(bk)>2.5
	K^+	LH(K)/LH(bk)>3.0
p>Thr(p)	π^+	LH(π)/LH(bk)>2.5
	K^+	LH(K)/LH(bk)>2.4

Table 3.2 Summary of **RICH $\bar{\Lambda}$ cuts** to identify negative electrons e^-, pions π^- and kaons K^- to be rejected.

Momentum range	**Identification of**	**Likelihood cut**
Thr(π)<p<Thr(K)	e^-	LH(e)/LH(bk)>1.9
	π^-	LH(π)/LH(bk)>1.9
Thr(K)<p<Thr(p)	π^-	LH(π)/LH(bk)>2.2
	K^-	LH(K)/LH(bk)>3.0
p>Thr(p)	π^-	LH(π)/LH(bk)>2.4
	K^-	LH(K)/LH(bk)>2.2

As already pointed out, if the momenta of the daughter particles are higher than 50 GeV/c, the difference between the Cherenkov angles of pions and kaons is small. To avoid unreliable identifications, the **LikePid** function is automatically inhibited in this region, where anyway a quite large background contamination still persists. Since our aim is solely to reject non-proton particles, the bad pion/kaon separation is not matter of concern.

Our choice for an extension of the RICH rejection region over the 50 GeV/c limit (here referred to as RICH+ cut) is based on the likelihood values of each mass hypothesis calculated by the RICH algorithm: it is sufficient to ask the highest likelihood not to be the one associated to the pion or kaon (or electron) hypotheses to retain only protons and unidentified candidates.

In Fig. 3.13 four Cherenkov angle vs momentum scatter plots are reported for the positive particles are shown, in logic progression, in the $\alpha > 0$ case: after all cuts except for RICH

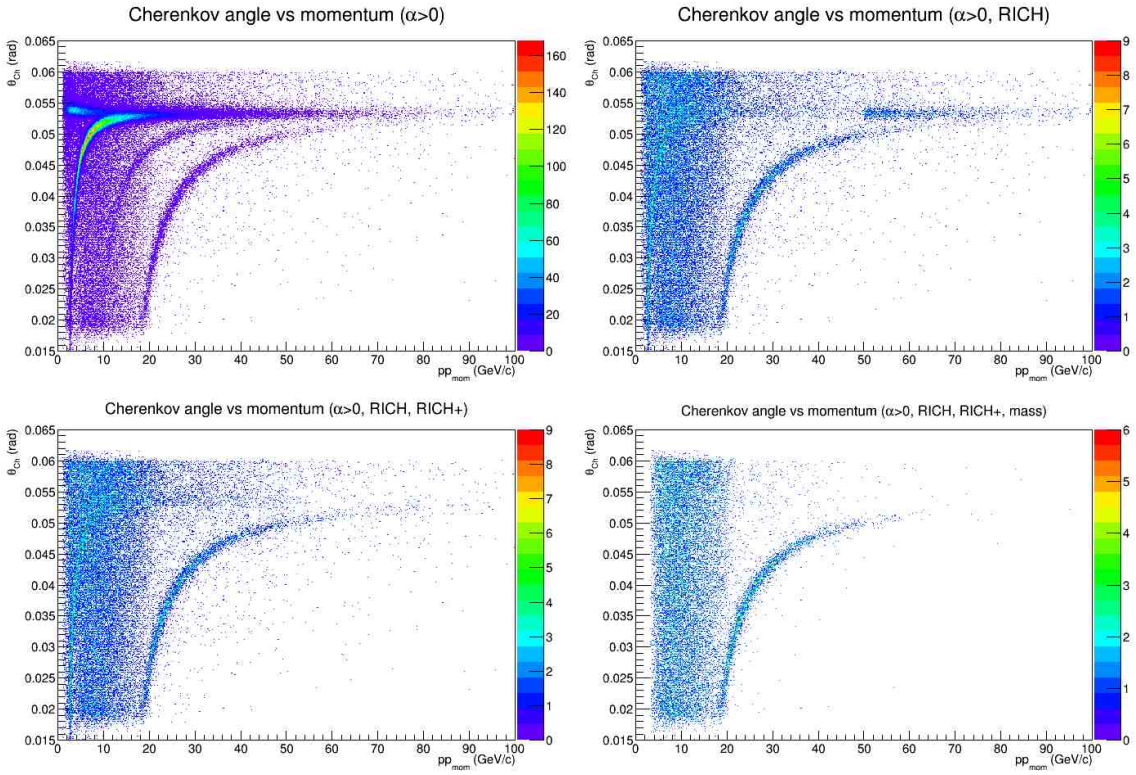

Figure 3.13 Cherenkov angle vs momentum for positive particles ($\alpha > 0$). Top, left: all candidates after all but RICH cut; Top, right: standard RICH cuts applied; Bottom, left: also RICH+ cut applied; Bottom, right: mass cut also applied.

(top left), after RICH cut (top right), after RICH+ cut also (bottom left), after mass cut also (bottom right).

The RICH+ rejection is concentrated on high energy values: for this reason a rejection of kaons in the overlapping region of the Armenteros plot, already provided by the RICH cut, is not expected (Fig. 3.14). The Armenteros plot, as resulting after all the selection procedure (except for the mass cut) can be seen in Fig. 3.15. The K_s^0 contribution, even if strongly reduced in the selection procedure, is still well visible. The final mass cut selects the two elliptic branches corresponding to Λs and $\bar{\Lambda}$s and the only retained background is given by those K_s^0 with a reconstructed mass identical, within three standard deviation, to that of the Λ.

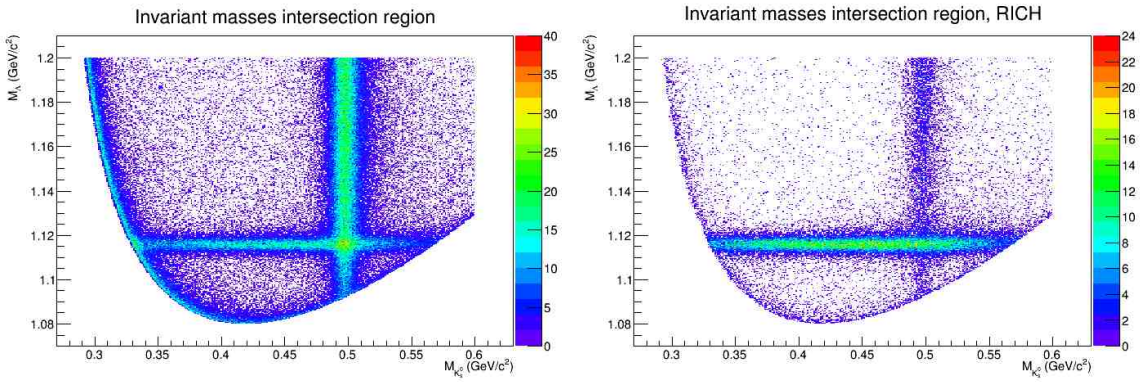

Figure 3.14 Intersection region between the Λ K_s^0 invariant masses. On the left before the RICH cut, on the right after the RICH cut.

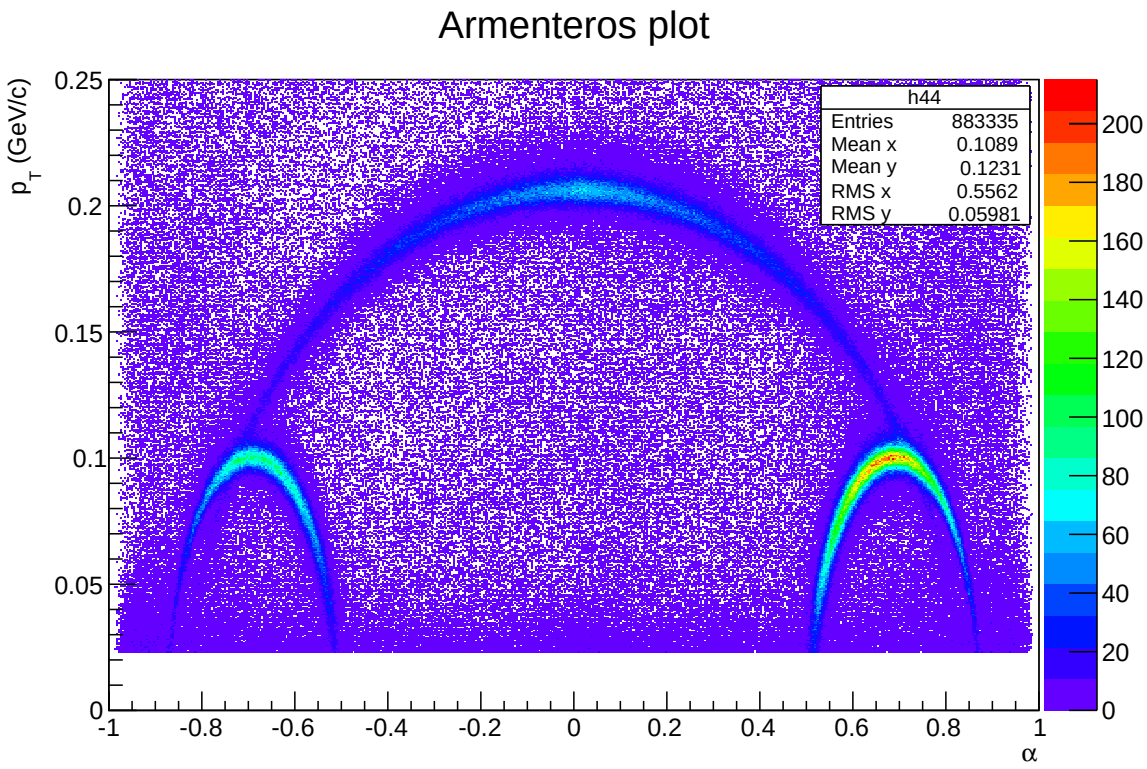

Figure 3.15 Armenteros plot after all selection cuts, except for the mass cut (all 2010 data).

3.3.4 Invariant mass spectra

In Fig. 3.16 the Λ and $\bar{\Lambda}$ invariant mass spectra before the mass cut are given, together with the corresponding section of the Armenteros plot. The invariant mass distributions are fitted with a superposition of a gaussian function and a constant function. The gaussian mean value can be compared to the PDG Λ mass value ($M_\Lambda = 1115.683 \pm 0.006$ MeV/c [18]); a common value for the peak standard deviation σ is chosen as 2.45 MeV/c.

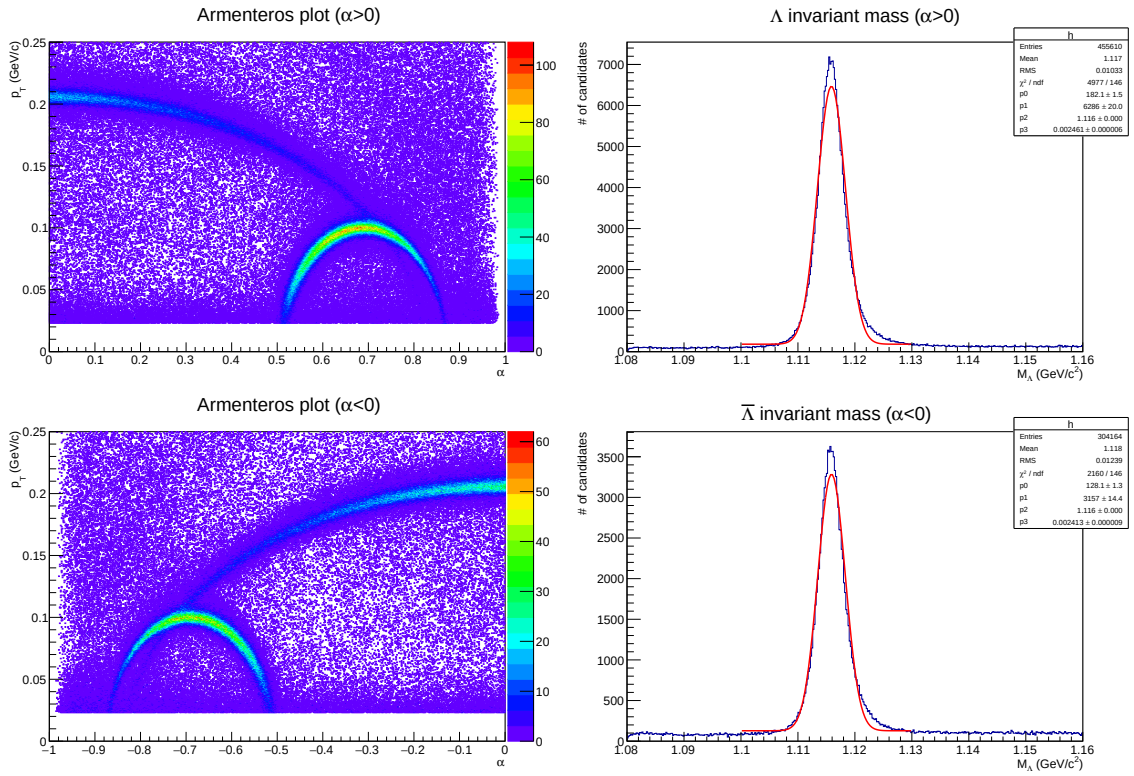

Figure 3.16 Left-up: Armenteros plot after all cuts ($\alpha > 0$ sector). Right-up: invariant mass spectrum for Λ candidates. Left-down: Armenteros plot after all cuts ($\alpha < 0$ sector). Right-down: invariant mass spectrum for $\bar{\Lambda}$ candidates.

An estimate of the background contribution to the mass peak is necessary to calculate the S/B ratio: to do that, the *sideband* method is a possible choice. Applied to our analysis, this method consists in counting the number of events in two proper mass intervals, one on the left and one on the right of the peak: the estimated number of background events under the mass peak is then the sum of background events in the outer intervals, normalised to the peak width. The statistical error on the number of events is taken as poissonian.

The selected sideband intervals are here (in MeV/c^2 units): (-30,-20) and (20,30), where the energy values refer to the shifted invariant mass spectrum. This method will be applied in all the x, z and p_t bins in which the Λ polarisation is extracted.

3.3.5 Further possible cuts

At the end of the selection procedure, after RICH and mass cuts, the distance D between primary and secondary vertex, measured in the laboratory frame, is found to be larger than 10 cm. For this reason, no cut on the distance have been implemented, apart from the necessary condition $D > 0$. In Fig. 3.17, the distance D distribution after applying the different cuts is shown: the highest curve is the one obtained after all cuts up to the collinearity cut (excluded); the second highest after the collinearity cut, the third highest after the p_T cut, the following after the RICH cuts and the lowest one (in yellow) is obtained after the mass cut around the Λ mass peak.

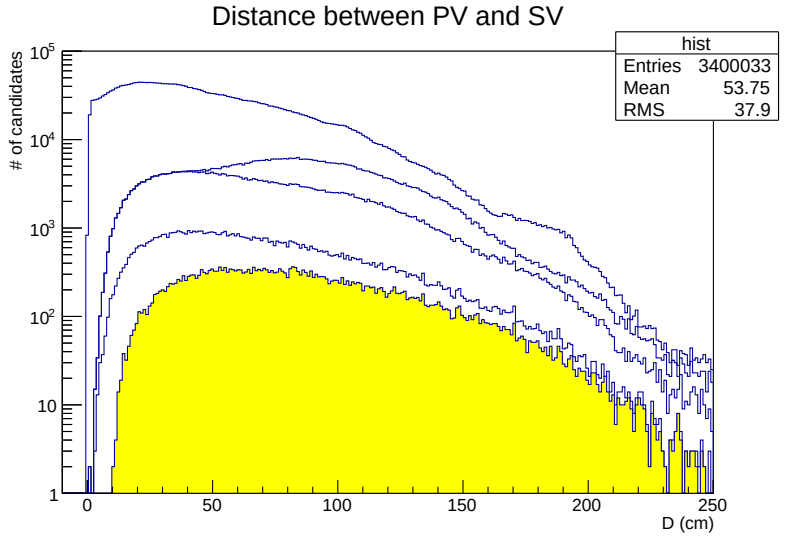

Figure 3.17 Evolution of the distance D distribution with the applied cuts, up to 250 cm.

For completeness, we have also studied the effect of removing the requirement that both decay tracks do not belong to any PV, asking at least one of the two particles to satisfy it. Such cut, which actually rejects particles with high mass and small transverse momentum (calculated with respect to the vector linking primary and secondary vertex), could have an impact on the number of protons in the final sample. Negligible differences have been found between the two different procedures at the end of the selection chain: thus, the usual cut has been maintained.

3.3.6 Kinematic distributions for Λ and $\bar{\Lambda}$

The typical kinematic distributions of the events survived after the selection procedure including the Λ mass cut are discussed here. Necessarily, the distributions contains the contribution given by the background events, lying inside the mass peak region, that can not be further removed but only numerically estimated.

To better appreciate similarities and differences between Λ and $\bar{\Lambda}$ candidates, the respective distributions are put side by side.

The kinematically descriptive quantities studied are:

- the squared momentum transfer Q^2 (Fig. 3.18, first row);
- the Bjorken scaling variable x_{Bj} (Fig. 3.18, second row);
- the fraction y of the incoming lepton energy carried by the photon (Fig. 3.18, third row);
- the mass of the hadronic final state W (Fig. 3.18, fourth row);
- the Feynman variable x_F (Fig. 3.19, first row);
- the fraction z of the photon energy taken by the Λ (Fig. 3.19, second row);
- the transverse momentum p_t of Λ with respect to the photon (Fig. 3.19, third row);
- the x_F-z correlation (Fig. 3.19, fourth row);

The kinematic distributions are obtained from 2010 data and they are in good agreement with those produced for 2007 events, not shown here.

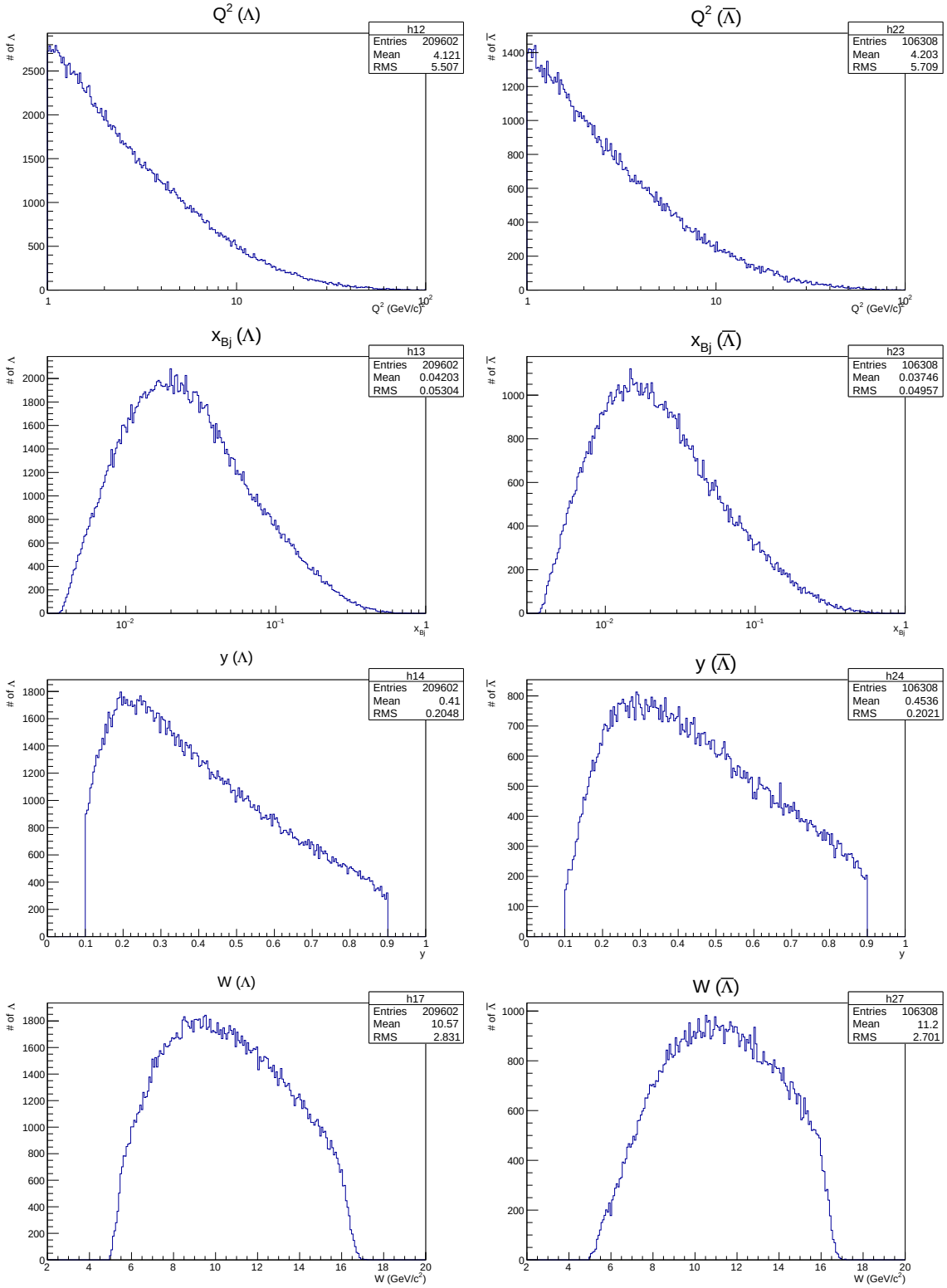

Figure 3.18 Q^2 (squared momentum transfer), x_{Bj} (Bjorken scaling variable), y (energy fraction of the projectile transferred from the incoming muon to the nucleon) and W (mass of the hadronic final state) for Λ candidates on the left and for $\bar{\Lambda}$ candidates on the right.

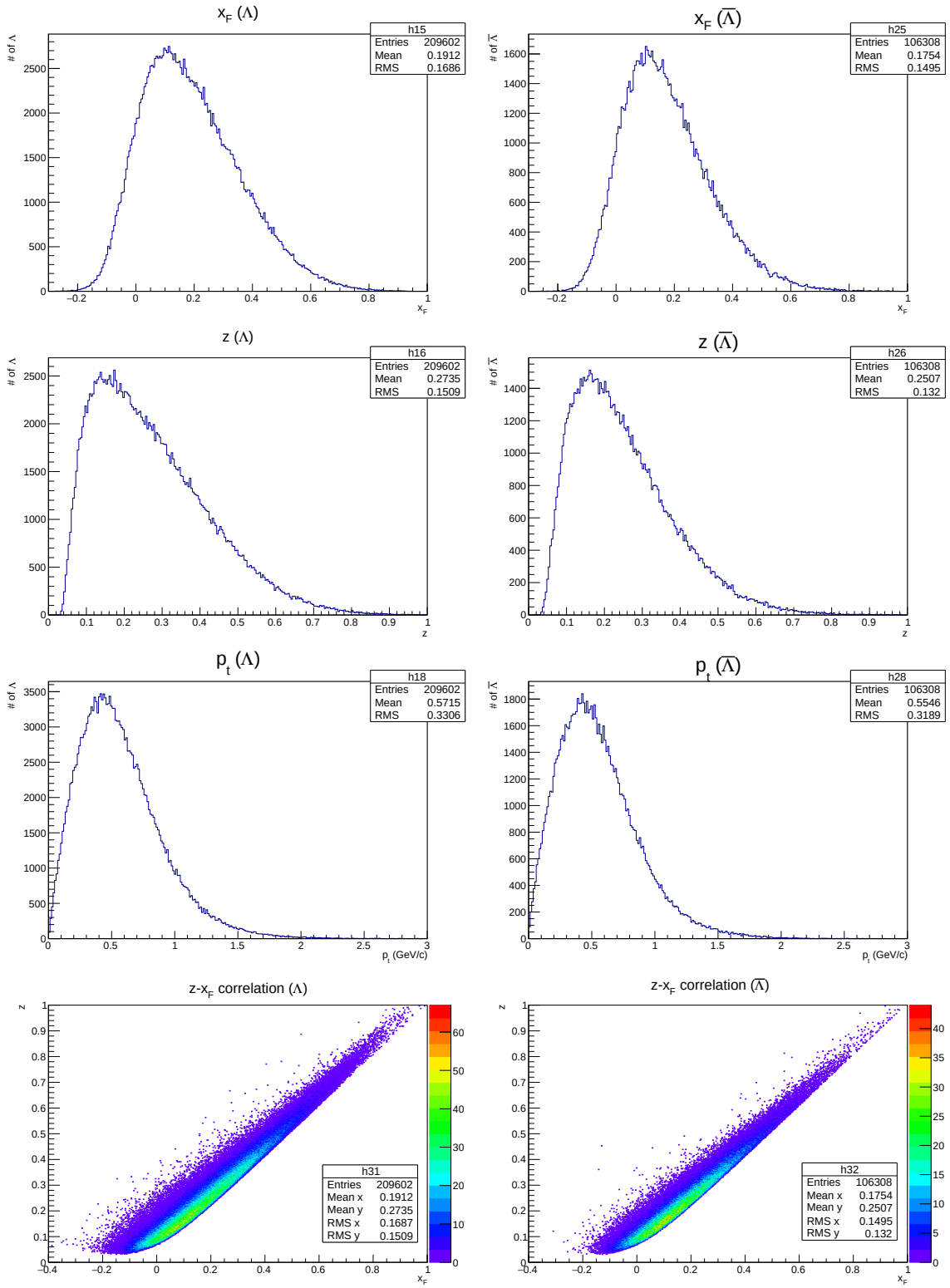

Figure 3.19 x_F (Feynman scaling variable), z (fraction of the virtual photon energy carried by the hadron), p_t (transverse momentum with respect to the virtual photon) and $z - x_F$ correlation for Λ candidates on the left and for $\bar{\Lambda}$ candidates on the right.

3.3.7 Final statistics for the Λ and $\bar{\Lambda}$ samples

In this section the effects of the selection procedure on statistics are analysed for both 2007 and 2010 datasets. The number of events after the DIS cuts in the mDST are 11.175.773 and 24.939.691, for 2007 and 2010 respectively. In Table 3.3 and Table 3.4 there are the description of the cuts, the number of candidates passing each of them and the relative ratio. The relative ratio is referred to the number of V^0 vertices.

It has been checked that the final candidates and their corresponding primary vertices are in a one-to-one correspondence: for any PV only one Λ candidate is reconstructed.

Moreover, the number of candidates after each cut, presented here, has been cross-checked with the analysis currently going on in the Bonn group. Two independent analyses are usually required by the COMPASS collaboration to release results.

Table 3.3 **2007 DATASET** Number of candidates passing each selection cut.

Number of V^0 vertices	86336050	
Cuts on Secondary Vertex and on Tracks	**Candidates**	**Ratio (V^0)**
Exactly two particles out of SV	86294454	1.000
Daughter particles with opposite charge	86288759	0.999
SV downstream of PV	65303432	0.756
Both tracks do not cross SM2 yoke	64958413	0.752
Hadron selection: X/X0<10	62257877	0.721
Quality cut on both tracks: $\chi^2_{red} < 10$	61337316	0.710
Quality cut on both tracks: $p > 1$ GeV/c	55155502	0.639
Both tracks not associated to any PV	20690745	0.240
Optimal position of first and last hits	17017214	0.197
Collinearity angle θ_{coll}< 7 mrad	2660329	0.031
Conversion background removal: p_T>23 MeV/c	1794774	0.021
Cut on energy fraction z<1	1692095	0.020
RICH rejection cuts	361881	0.004
RICH+ rejection cuts	347674	0.004
Invariant mass cut	143253	0.002
Λ candidates ($\alpha > 0$)	95135	0.001
$\bar{\Lambda}$ candidates ($\alpha < 0$)	48118	0.001

Table 3.4 **2010 DATASET** Number of candidates passing each selection cut.

Number of V^0 vertices	192570850	
Cuts on Secondary Vertex and on Tracks	**Candidates**	**Ratio (V^0)**
Exactly two particles out of SV	192559142	1.000
Daughter particles with opposite charge	192556279	1.000
SV downstream of PV	140057844	0.727
Both tracks do not cross SM2 yoke	139293440	0.723
Hadron selection: X/X0<10	132187748	0.686
Quality cut on both tracks: $\chi^2_{red} < 10$	130206056	0.676
Quality cut on both tracks: $p > 1$ GeV/c	118826717	0.617
Both tracks not associated to any PV	40148062	0.208
Optimal position of first and last hits	31288561	0.162
Collinearity angle θ_{coll}< 7 mrad	5656328	0.029
Conversion background removal: p_T>23 MeV/c	3675221	0.019
Cut on energy fraction z<1	3611952	0.019
RICH rejection cuts	787749	0.004
RICH+ rejection cuts	759774	0.004
Invariant mass cut	315910	0.002
Λ candidates ($\alpha > 0$)	209602	0.001
$\bar{\Lambda}$ candidates ($\alpha < 0$)	106308	0.001

3.4 Extraction of Λ polarisation

Following the calculations of Ref. [16] reported in Sect. 1.3.1 we have measured the Λ polarisation with respect to the expected direction of the spin of the fragmenting quark, as described in detail in the following. Eq. 1.42 is then rewritten as:

$$\vec{P}_\Lambda(x,z) = f P_T D_{NN}(y) \frac{\sum_q e_q^2 h_1(x) H_1^{\Lambda/q}(z)}{\sum_q e_q^2 f_1(x) D_1^{\Lambda/q}(z)} \vec{S}'_T. \tag{3.15}$$

With respect to Eq. 1.42, two more factors are present here:

- the *dilution factor* f, corresponding to the fraction of target nucleons effectively polarised, here taken to be the ratio of free protons over the total number of nucleons in the NH_3 target, namely 3/17;
- the *target polarisation* P_T, whose typical value is 85%, continuously monitored during the data taking.

Two ingredients are necessary to define our $\vec{S}'_T$ quantisation axis: the target polarisation vector and the normal to the scattering plane. Of these two, the first is known to be fixed in the laboratory system ($\vec{S}_T = (0,1,0)$) and the second can be calculated event by event as a simple cross product of the incoming and outgoing muon three-vectors.

3.4.1 Construction of the quantisation axis

Here we assume that the quark entering the elementary process $\ell q \to \ell q$ has polarisation parallel to $\vec{S}_T$. After the scattering, the component of the spin transverse to the direction of the virtual photon γ^* is reflected with respect to the normal $\hat{n}$ to the scattering plane. Thus, the construction of the quantisation axis consists of the following steps:

- subtraction of the component of $\vec{S}_T$ along the virtual photon γ. If $\hat{q}$ is the unitary vector indicating the γ^* direction,
$$\vec{S}_{T,\gamma} = \vec{S}_T - (\vec{S}_T \cdot \hat{q})\hat{q} \tag{3.16}$$
- reflection of $\vec{S}_{T,\gamma}$ with respect to the normal to the scattering plane $\hat{n}$:
$$\vec{S}'_T = -\vec{S}_{T,\gamma} + 2(\vec{S}_{T,\gamma} \cdot \hat{n})\hat{n} \tag{3.17}$$

If we choose to work in the GNS, then $\hat{n}$ exactly corresponds to the y-axis and the formula in Eq. 3.17, written for the x and y components, simplifies to:

$$S'_x = -S_x \qquad S'_y = S_y \tag{3.18}$$

Finally, the Λ polarisation P_Λ with respect to $\vec{S}'_T$,

$$P_\Lambda(x,z) = f P_T D_{NN}(y) \frac{\sum_q e_q^2 h_1^q(x) H_1^{\Lambda/q}(z)}{\sum_q e_q^2 f_1^q(x) D_1^{\Lambda/q}(z)}. \tag{3.19}$$

reveals itself in the angular distribution (Sect. 1.3.2):

$$\frac{dN}{d\cos\theta} \propto 1 + \alpha P_\Lambda \cos\theta \tag{3.20}$$

where θ is the proton emission angle, calculated in the Λ rest frame, with respect to S'_T. The proton momentum in the Λ rest frame, namely $\vec{p}_p^{\,\Lambda}$, is calculated as a Lorentz boost of the momentum in the laboratory system $\vec{p}_p^{\,lab}$ along the Λ line of flight [53]:

$$\vec{p}_p^{\,\Lambda} = \vec{p}_p^{\,lab} + \left((\gamma - 1) \frac{\vec{\beta} \cdot \vec{p}_p^{\,lab}}{\beta^2} - \gamma E_p^{lab} \right) \vec{\beta} \tag{3.21}$$

The three components of the $\vec{\beta}$ vector are those of the Λ velocity, along each laboratory axis, in units of the speed of light c; γ, as usual, is equal to $1/\sqrt{1-\vec{\beta}\cdot\vec{\beta}}$.

3.4.2 Λ polarisation extraction

In measuring the transverse polarisation $\vec{P}_\Lambda$ one has to be careful in avoiding possible systematic effects introduced by the apparatus acceptance: the COMPASS spectrometer, in particular, has an asymmetric layout due to the dipole magnets. Such well known effects have been minimised in COMPASS by choosing the particular target configuration, with three cells of opposite polarisations. In addition, the data taking has been divided in periods consisting of two subperiods in which data were taken with two opposite polarisation orientation in each cell. In each period very stable data taking conditions were assured (in particular in the 2010 run) in order to cancel acceptance effects as can be seen in an analytical way when two successive polarisation subperiods are considered.

Let's consider the "-+-" configuration: this means that the *upstream* (U) and *downstream* (D) cells are polarised downward, the *central* (C) upward. It is convenient to indicate with the index "1" the C cell and with the index "2" the U and D cells. Using Eq. 3.4.1, the number of reconstructed Λ particles, emitting a proton in a given range of the angle θ is:

$$\mathscr{N}_1 = \Phi_1 \rho_1 \left(\frac{d\sigma}{d\Omega} \right)^0 (1 + \alpha P_\Lambda \cos\theta) A_1(\cos\theta) \tag{3.22}$$

$$\mathscr{N}_2 = \Phi_2 \rho_2 \left(\frac{d\sigma}{d\Omega} \right)^0 (1 - \alpha P_\Lambda \cos\theta) A_2(\cos\theta) \tag{3.23}$$

where Φ_i is the muon flux, ρ_i is the target cell length, $\left(\frac{d\sigma}{d\Omega}\right)^0$ is the differential cross section for the production of Λs and $A_i(\cos\theta)$ is the acceptance term which includes both geometrical acceptance and spectrometer efficiency. The opposite sign in front of P_Λ is due to the choice of keeping fixed the reference axis for the calculation of $\vec{S}_T'$, always equal to (0,1,0) for both target polarisation orientations.

The reversal of the cells spin configuration to "+-+" in between the two successive data taking subperiods leads to:

$$\mathscr{N}_1' = \Phi_1' \rho_1 \left(\frac{d\sigma}{d\Omega} \right)^0 (1 - \alpha P_\Lambda \cos\theta) A_1'(\cos\theta) \tag{3.24}$$

$$\mathscr{N}_2' = \Phi_2' \rho_2 \left(\frac{d\sigma}{d\Omega}\right)^0 (1 + \alpha P_\Lambda \cos\theta) A_2'(\cos\theta) \tag{3.25}$$

Let's consider now the double ratio:

$$\varepsilon = \frac{\mathscr{N}_1 \mathscr{N}_2'}{\mathscr{N}_1' \mathscr{N}_2}. \tag{3.26}$$

According to Eq. 3.22-3.25, and noticing that $\Phi_1 = \Phi_2$ and $\Phi_1' = \Phi_2'$ because of the requirements in the DIS event reconstruction, it can be rewritten as:

$$\begin{aligned}
\varepsilon &= \frac{\Phi_1 \left(\frac{d\sigma}{d\Omega}\right)^0 (1 + \alpha P_\Lambda \cos\theta) A_1(\cos\theta) \times \Phi_2' \left(\frac{d\sigma}{d\Omega}\right)^0 (1 + \alpha P_\Lambda \cos\theta) A_2'(\cos\theta)}{\Phi_1' \left(\frac{d\sigma}{d\Omega}\right)^0 (1 - \alpha P_\Lambda \cos\theta) A_1'(\cos\theta) \times \Phi_2 \left(\frac{d\sigma}{d\Omega}\right)^0 (1 - \alpha P_\Lambda \cos\theta) A_2(\cos\theta)} \\
&= \frac{(1 + \alpha P_\Lambda \cos\theta) A_1(\cos\theta) \times (1 + \alpha P_\Lambda \cos\theta) A_2'(\cos\theta)}{(1 - \alpha P_\Lambda \cos\theta) A_1'(\cos\theta) \times (1 - \alpha P_\Lambda \cos\theta) A_2(\cos\theta)} \\
&\sim (1 + 4\alpha P_\Lambda \cos\theta) \frac{A_1(\cos\theta) \times A_2'(\cos\theta)}{A_1'(\cos\theta) \times A_2(\cos\theta)}
\end{aligned} \tag{3.27}$$

where the approximation is well justified by the small expected value of P_Λ. The *reasonable assumption* about the performance of the COMPASS spectrometer states that the ratio of acceptance in the upstream and downstream cells on one side, and of the central cell on the other, stays constant between two consecutive data taking subperiods:

$$\frac{A_1(\cos\theta)}{A_1'(\cos\theta)} = \frac{A_2(\cos\theta)}{A_2'(\cos\theta)}. \tag{3.28}$$

Thanks to this assumption, the expression for ε simply becomes:

$$\varepsilon = 1 + 4\alpha P_\Lambda \cos\theta \tag{3.29}$$

and, after dividing data in n bins of $\cos\theta$ (n=8 in our analysis), P_Λ can be extracted with a linear fit of the quantities ε_j with $j = 1, n$.

The variance of ε_j, assuming poissonian statistics on the total number of events, is:

$$\sigma_{\varepsilon_j}^2 = \varepsilon_j^2 \sum_{i=1}^{4} \frac{1}{\mathscr{N}_{ij}} \tag{3.30}$$

It is important to notice that if $\varepsilon_j < 1$ due to statistical fluctuations, then the corresponding variance is artificially lowered. This effect can introduce a bias in particular when the number of events $\mathscr{N}_{ij}$ is small and it has been verified by the Trieste COMPASS group that it is safer

to substitute the expression for $\sigma^2_{\varepsilon_j}$ with the following:

$$\sigma^2_{\varepsilon_j} = 1 \sum_{i=1}^{4} \frac{1}{\mathcal{N}_{ij}} \tag{3.31}$$

where ε^2_j has been replaced by its expectation value in case of zero polarisation.

A further complication is due to the fact that $\mathcal{N}_{ij}$ is the number of produced Λs in that $\cos\theta$ bin. As shown in Sect. 3.3.4, the background in the final candidates sample is much smaller than the signal. Still it has to be taken into account when measuring the Λ polarization. A possible way to do it is to assume a given reasonable polarization for the background events (which could also be zero) and correct for the corresponding contribution to the Λ polarization. Here a different procedure has been followed: $\mathcal{N}_{ij}$ in each $\cos\theta$ bin is the difference between the number of Λ candidates ($\mathcal{N}^{tot}_{ij}$) and the number of background events ($\mathcal{N}^{B}_{ij}$) evaluated with the sideband method described in Sect. 3.3.4. As a result, assuming Poisson distributions, the statistical uncertainty on $\mathcal{N}_{ij}$ is given by: $\sigma^2_{\mathcal{N}_{ij}} = \mathcal{N}^{tot}_{ij} + \mathcal{N}^{B}_{ij}$. Thus Eq. 3.31 becomes:

$$\sigma^2_{\varepsilon_j} = \sum_{i=1}^{4} \frac{\mathcal{N}^{tot}_{ij} + \mathcal{N}^{B}_{ij}}{(\mathcal{N}^{tot}_{ij} - \mathcal{N}^{B}_{ij})^2}. \tag{3.32}$$

In case of small number of events involved (typically smaller than 10), some bias can be introduced and this point has been checked in measuring the polarization.

3.4.3 Data binning and 2007/2010 statistics

The Λ and $\bar{\Lambda}$ polarisation has been measured by dividing the samples into six subsamples of x and five subsamples of z and in five subsamples of the Λ transverse momentum in the GNS p_t. A dependence of the polarisation on x and on z is predicted by theory and the p_t dependence is also of interest. The intervals have been chosen in order to get balanced statistics bin per bin, making also reference to optimised intervals where transversity has been proved to be different from zero.

In Tab. 3.5 and Tab. 3.6, the bin widths for x, z and p_t are reported for 2007 and 2010 data, together with the corresponding mean values, the number of candidates after sideband subtraction, the S/B ratio and the $FoM = S^2/(S+B)$. The S/B ratios are also shown as functions of x, z and p_t in Fig. 3.20 for Λ and $\bar{\Lambda}$ candidates, 2007 and 2010 data samples. Data quality in the two considered years appears compatible.

In each of the aforementioned bins the Λ and $\bar{\Lambda}$ polarisations have been measured for each period of the 2007 and 2010 data taking, for a total of 6+12=18 periods. The results are described in the next chapter.

Table 3.5 **2007 DATASET** Data binning and statistics for the extraction of Λ and $\bar{\Lambda}$ polarisation. Values for p_t are intended in units of GeV/c.

Λ EVENTS				
x **binning**	**mean value**	**candidates**	**S/B ratio**	**FoM**
$x < 0.013$	0.009	23689 ± 166	12.3 ± 0.3	21913.3
$0.013 < x < 0.020$	0.016	16095 ± 132	23.1 ±0.9	15427.8
$0.020 < x < 0.032$	0.025	17051 ± 135	31.2 ±1.4	16521.7
$0.032 < x < 0.060$	0.044	17009 ± 134	36.7 ±1.7	16557.7
$0.060 < x < 0.210$	0.105	15301 ± 127	43.1 ±2.3	14954.0
$x > 0.210$	0.289	1967 ± 45	47.0 ±7.3	1926.1
z **binning**	**mean value**	**candidates**	**S/B ratio**	**FoM**
$z < 0.12$	0.090	13489 ± 124	14.8±0.5	12637.0
$0.12 < z < 0.20$	0.160	21074 ± 152	19.5±0.6	20044.6
$0.20 < z < 0.30$	0.248	22591 ± 156	26.4±0.9	21765.7
$0.30 < z < 0.42$	0.355	18673 ± 141	29.7±1.2	18064.6
$z > 0.42$	0.529	15286 ± 128	28.0± 1.2	14758.6
p_t **binning**	**mean value**	**candidates**	**S/B ratio**	**FoM**
$p_t < 0.30$	0.193	17792 ± 148	8.6±0.2	15931.6
$0.30 < p_t < 0.50$	0.401	23758 ± 160	26.5±0.9	22894.2
$0.50 < p_t < 0.75$	0.616	25676 ± 164	46.0±2.0	25130.1
$0.75 < p_t < 1.10$	0.893	17083 ± 133	50.0±2.7	16748.2
$p_t > 1.10$	1.356	6802 ± 84	45.8±3.8	6657.2

$\bar{\Lambda}$ **EVENTS**				
x **binning**	**mean value**	**candidates**	**S/B ratio**	**FoM**
$x < 0.013$	0.009	13717 ± 130	8.4±0.2	12254.8
$0.013 < x < 0.020$	0.016	8372± 97	15.8±0.7	7874.1
$0.020 < x < 0.032$	0.025	7972 ± 94	18.7±0.9	7566.6
$0.032 < x < 0.060$	0.044	7566 ± 91	23.2±1.3	7254.2
$0.060 < x < 0.210$	0.103	6566 ± 84	26.0±1.7	6323.1
$x > 0.210$	0.291	717 ± 28	19.5±3.3	682.3
z **binning**	**mean value**	**candidates**	**S/B ratio**	**FoM**
$z < 0.12$	0.092	6651 ± 88	11.7±0.5	6127.0
$0.12 < z < 0.20$	0.160	12081 ± 117	14.4±0.5	11295.8
$0.20 < z < 0.30$	0.247	12575 ± 119	16.3±0.6	11848.9
$0.30 < z < 0.42$	0.353	8596± 98	16.5±0.7	8104.6
$z > 0.42$	0.517	5008 ± 78	9.9±0.5	4547.0
p_t **binning**	**mean value**	**candidates**	**S/B ratio**	**FoM**
$p_t < 0.30$	0.189	8764 ± 110	5.1±0.1	7326.1
$0.30 < p_t < 0.50$	0.401	12322 ± 117	19.0±0.8	11705.1
$0.50 < p_t < 0.75$	0.616	12862 ± 117	27.6±1.3	12412.7
$0.75 < p_t < 1.10$	0.890	8188 ± 93	31.7±2.0	7937.9
$p_t > 1.10$	1.336	2774 ± 55	24.4±2.3	2664.6

Table 3.6 **2010 DATASET** Data binning and statistics for the extraction of Λ and $\bar{\Lambda}$ polarisation. Values for p_t are intended in units of GeV/c.

Λ EVENTS				
x **binning**	**mean value**	**candidates**	**S/B ratio**	**FoM**
$x < 0.013$	0.009	51912 ± 243	14.2 ± 0.2	48494.6
$0.013 < x < 0.020$	0.016	34230 ± 192	24.6 ± 0.7	32894.9
$0.020 < x < 0.032$	0.025	37190 ± 199	33.4 ± 1.0	36109.7
$0.032 < x < 0.060$	0.042	38381 ± 201	36.7 ± 1.1	37362.5
$0.060 < x < 0.210$	0.099	35464 ± 193	41.6 ± 1.4	34632.3
$x > 0.210$	0.291	4244 ± 67	34.8 ± 3.2	4125.4
z **binning**	**mean value**	**candidates**	**S/B ratio**	**FoM**
$z < 0.12$	0.089	29363 ± 181	17.0 ± 0.4	27731.1
$0.12 < z < 0.20$	0.160	46427 ± 225	21.3 ± 0.5	44346.6
$0.20 < z < 0.30$	0.248	49779 ± 231	27.2 ± 0.6	48014.0
$0.30 < z < 0.42$	0.355	41539 ± 210	33.0 ± 0.9	40318.8
$z > 0.42$	0.530	34313 ± 192	28.9 ± 0.9	33165.6
p_t **binning**	**mean value**	**candidates**	**S/B ratio**	**FoM**
$p_t < 0.30$	0.192	40109 ± 220	9.7 ± 0.2	36359.9
$0.30 < p_t < 0.50$	0.401	53480 ± 239	29.9 ± 0.7	51749.4
$0.50 < p_t < 0.75$	0.616	56083 ± 242	44.0 ± 1.2	54835.9
$0.75 < p_t < 1.10$	0.893	37606 ± 197	55.0 ± 2.1	36933.7
$p_t > 1.10$	1.358	14144 ± 121	47.6 ± 2.8	13853.2

$\bar{\Lambda}$ EVENTS				
x **binning**	**mean value**	**candidates**	**S/B ratio**	**FoM**
$x < 0.013$	0.009	29891 ± 191	9.2 ± 0.2	26966.4
$0.013 < x < 0.020$	0.016	18019 ± 142	16.1 ± 0.5	16966.4
$0.020 < x < 0.032$	0.025	17924 ± 141	18.7 ± 0.6	17015.6
$0.032 < x < 0.060$	0.042	17062 ± 136	22.4 ± 0.8	16331.8
$0.060 < x < 0.210$	0.098	14938 ± 127	25.4 ± 1.1	14372.3
$x > 0.210$	0.294	1720 ± 44	19.7 ± 2.2	1636.3
z **binning**	**mean value**	**candidates**	**S/B ratio**	**FoM**
$z < 0.12$	0.092	14714 ± 131	12.1 ± 0.4	13586.9
$0.12 < z < 0.20$	0.160	26876 ± 174	15.6 ± 0.4	25252.8
$0.20 < z < 0.30$	0.247	27955 ± 176	18.4 ± 0.5	26516.4
$0.30 < z < 0.42$	0.353	19124 ± 146	16.8 ± 0.5	18052.5
$z > 0.42$	0.515	10884 ± 115	9.4 ± 0.3	9840.4
p_t **binning**	**mean value**	**candidates**	**S/B ratio**	**FoM**
$p_t < 0.30$	0.191	20079 ± 165	5.7 ± 0.1	17082.4
$0.30 < p_t < 0.50$	0.402	27190 ± 173	19.3 ± 0.5	25852.2
$0.50 < p_t < 0.75$	0.615	28357 ± 174	29.1 ± 1.0	27416.0
$0.75 < p_t < 1.10$	0.890	17836 ± 138	30.0 ± 1.2	17259.5
$p_t > 1.10$	1.344	6091 ± 81	23.7 ± 1.5	5845.3

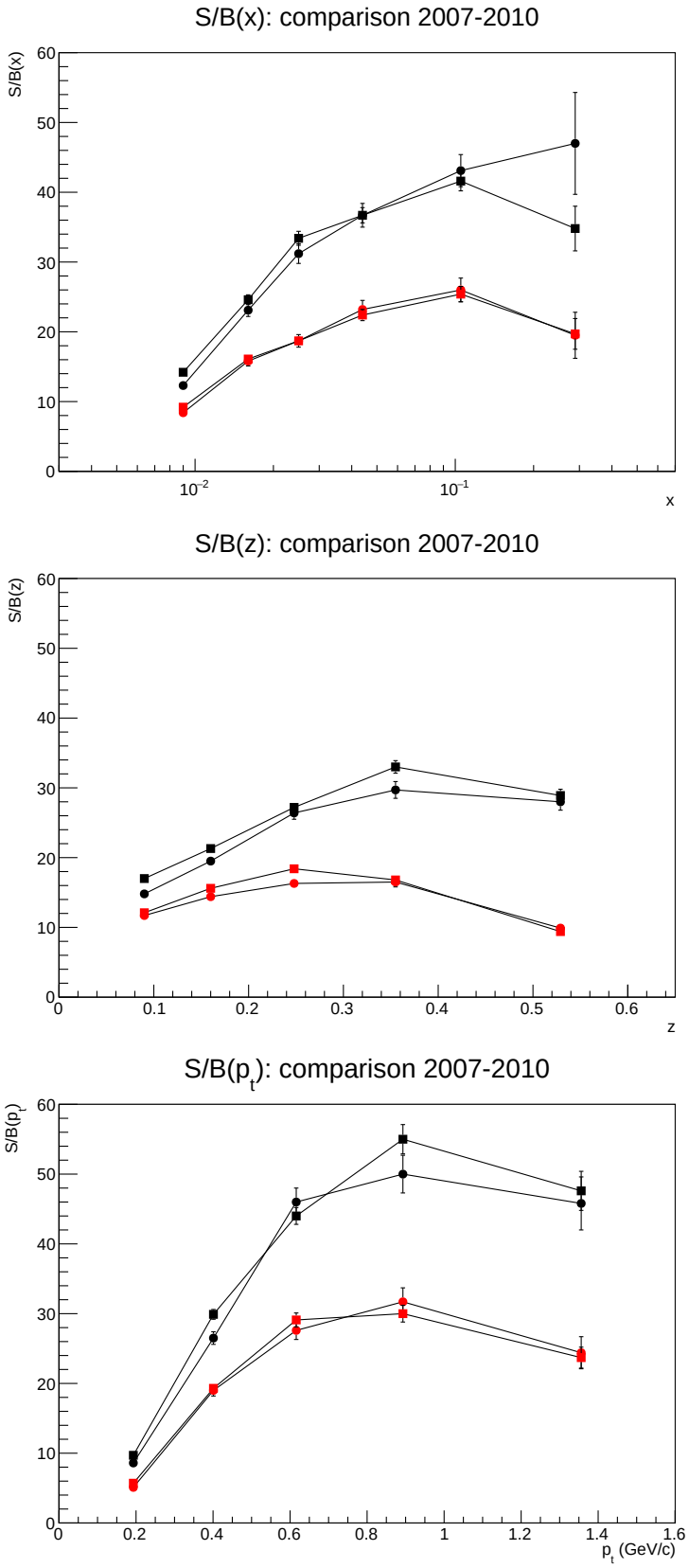

Figure 3.20 S/B ratios as function of x, z and p_t for Λs (black points) and for $\bar{\Lambda}$s (red points) . Full circles correspond to 2007 values, full squares to 2010 ones.

Chapter 4

Results

4.1 Strategies and kinematic regions

The Λ and $\bar{\Lambda}$ polarisation values have been measured in several kinematic regions and with two different strategies, namely:

- extracting the polarisation period by period and then calculating the final polarisation values as weighted means of 18 periods (6 for 2007, 12 for 2010; first strategy);
- summing periods of the same year with the same target configuration, so treating separately 2007 as one period and 2010 as a second period, and then extracting the results as a weighted mean of 2 periods (second strategy). Compatibility between 2007 and 2010 results is reported in Appendix.

Both methods have pros and cons. A period-by-period analysis is preferable to minimise acceptance effects, since the *reasonable assumption* on the COMPASS spectrometer performance is more likely to hold, but it can also lead, in case of poor statistics in some bins, to a bias of the double ratio due to the large statistical fluctuations. On the other hand, the second strategy surely solves for a possible lack of statistics, but some acceptance effects could survive. The difference between the results obtained with the two methods can be used to evaluate the systematic uncertainties.

With these two methods, the Λ and $\bar{\Lambda}$s polarisation has been studied in the following cases and according to the binning introduced in the last chapter:

- all candidates considered;
- high z region, here defined by the condition $z_\Lambda > 0.2$ and $x_F > 0$;
- low z region: $z_\Lambda < 0.2$ or $x_F < 0$ (complementary to high z);

- high x region ($x > 0.032$), where transversity for u and d quarks is known to be different from zero;
- low x region ($x < 0.032$) where instead a signal compatible with zero has been measured;
- high p_t region ($p_t > 0.5$ GeV/c):
- low p_t region ($p_t < 0.5$ GeV/c).

The polarisation values for Λs and $\bar{\Lambda}$s (all candidates) are presented as function of x, z and p_t in Fig. 4.1, where the two described strategies are compared. Full circles correspond to the first strategy (period-by-period analysis), open circles to the analysis of integrated periods. There is a general agreement between the two methods. The bins with low statistics are generally characterised by a period-by-period extracted polarisation that is higher than the one calculated with the second method.

Another possible comparison between the methods comes from the distributions of the χ^2 values obtained from the fits in the eight $\cos\theta$ bins of the double ratios, each calculated in the aforementioned bins of x, z and p_t. In Fig. 4.2 we report the χ^2 distributions, obtained with the two strategies, considering all candidates. The experimental points are plotted on the theoretical curve (χ^2 distribution with six degrees of freedom: eight is the number of bins in $\cos\theta$ where the fit is performed, two is the number of parameters). As expected, the period-by-period method returns a larger number of high χ^2s, indicating a worst convergence of the fit due to a deviation of the double ratio, in some bins, from its expected value. All fits (in x, in z and in p_t) contribute here to the overall χ^2 distributions. The agreement with the expected distributions is good.

Compatibility of the final Λ and $\bar{\Lambda}$ polarisation for each considered bin in x, z and p_t can be studied by constructing the distribution of the quantities

$$\frac{P_i - < P >}{\sqrt{\sigma^2_{P_i} - \sigma^2_{<P>}}} \tag{4.1}$$

known as *pulls*, where P_i is the measured polarisations in each bin, for each period, and $< P >$ the corresponding weighted mean. The expected distribution of the pulls is a gaussian, whose width is an indication of possible systematic errors. The pulls distribution for the two adopted strategies are reported in Fig. 4.3

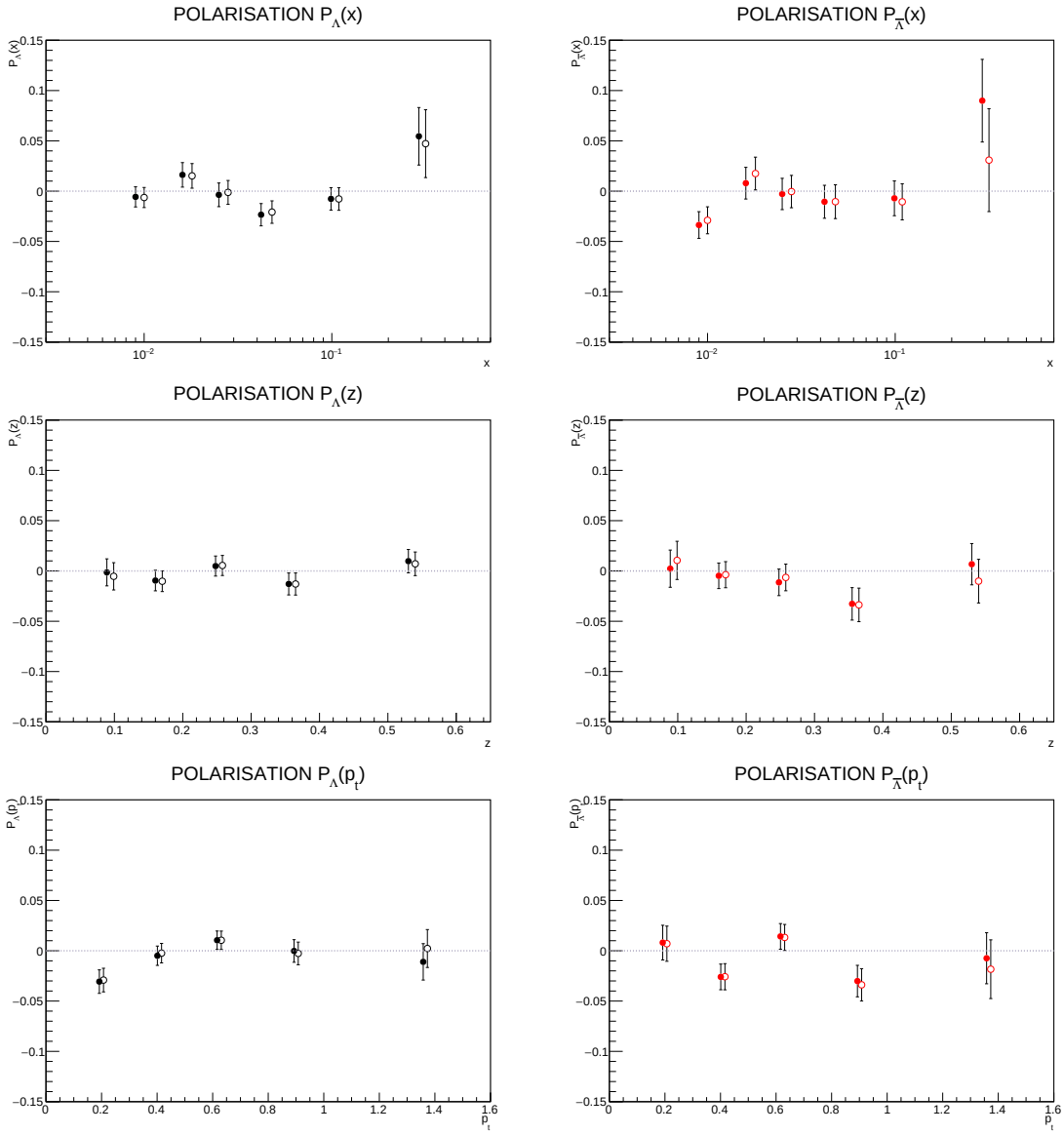

Figure 4.1 Measured polarisations for all Λ (left) and $\bar{\Lambda}$ (right) candidates, as function of x, z and p_t. The two extraction methods are compared: full circles correspond to first strategy, open circles to second strategy.

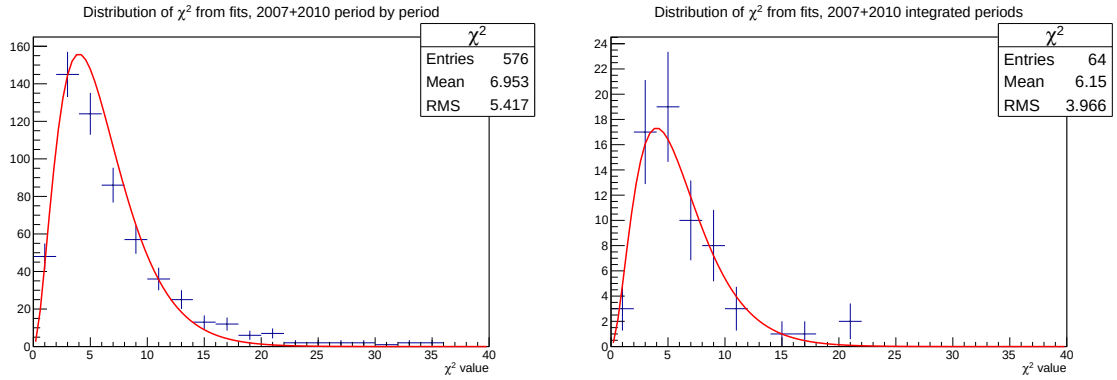

Figure 4.2 Distribution of the χ^2 values obtained with the first (left) and the second (right) methods, compared to the theoretical curve $\chi^2_{ndf=6}$. All candidates considered.

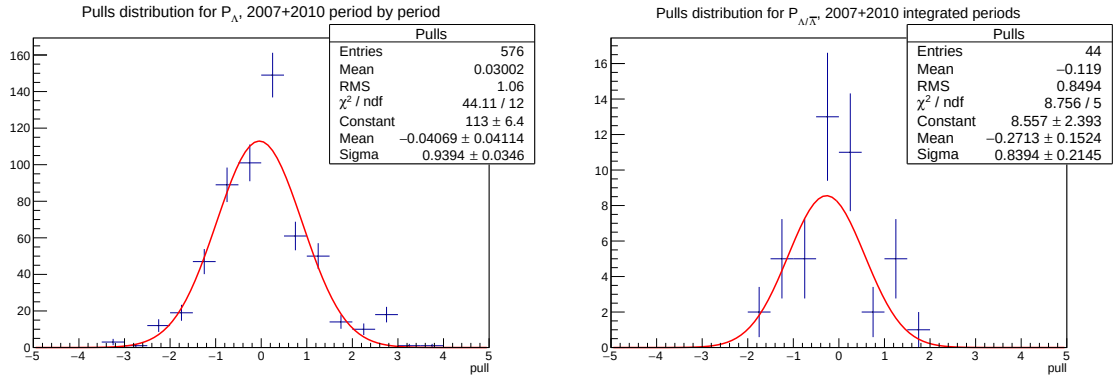

Figure 4.3 Pulls distribution obtained with the first (left) and the second (right) methods, fitted with a gaussian function. All candidates considered.

4.2 Comparison with 2007 released results

In Fig. 4.4 a comparison is presented between the polarisations obtained as a function of x and z, for Λs and $\bar{\Lambda}$s, with the two strategies currently adopted (full and open circles) and the results obtained and released from the 2007 analysis [33], marked with a star.

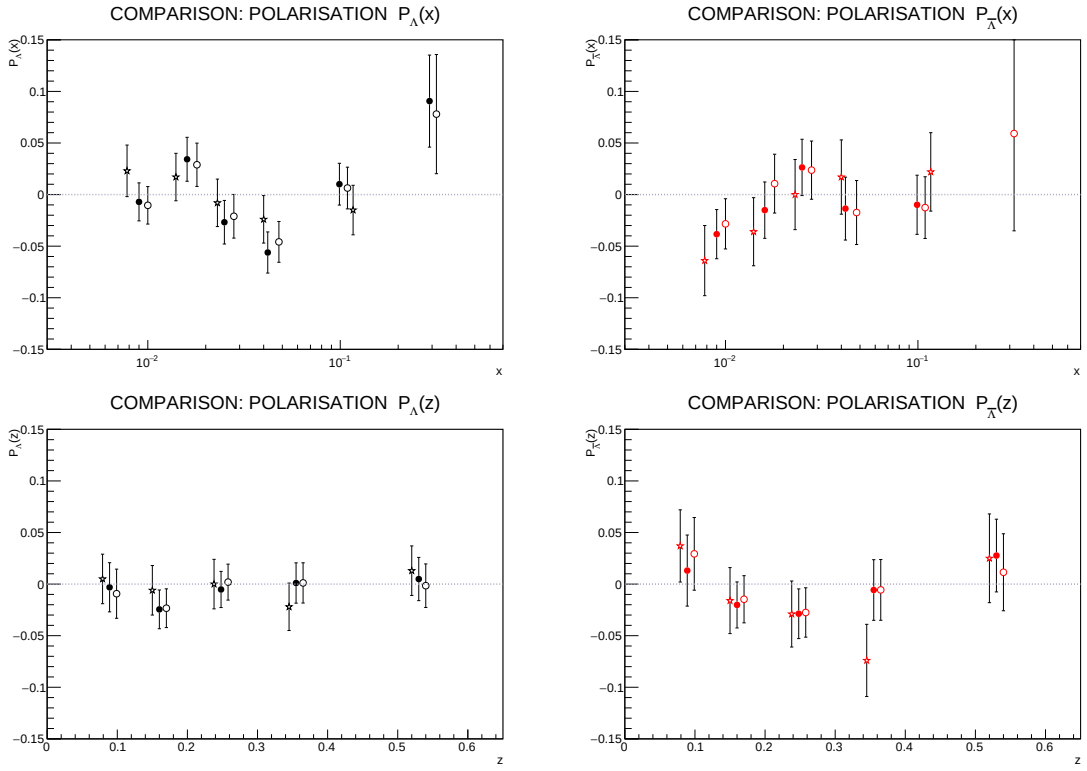

Figure 4.4 Comparison between 2007 results: released (star), period-by-period (full circles) and integrating periods (open circles).

As can be seen, the agreement between the two strategies is very good. The agreement with the already released results is satisfactory, in particular taking into account that our analysis differs from the one performed in the past on 2007 data as for the selection procedure and for the method of polarisation extraction. Some differences are also due to the different binning (6 x bins now, 5 in the past). However, the agreement of the current results with the released ones is good.

As a summary of these tests, is that the new methods give result compatible with the already released ones and that both strategies can be followed in the measurement of the Λ polarisation.

4.3 Measured polarisations

Here we present the extracted values for Λ and $\bar{\Lambda}$ polarisation. The second strategy has been adopted. Results are reported only as function of those kinematic quantities that do not define the considered region. For example, $P_\Lambda(x)$ is not shown in the two kinematic regions $x > 0.032$ and $x < 0.032$, since it would be exactly the same as the $P_\Lambda(x)$ in the "all candidates" case. The error bars represent statistical uncertainties only. For each kinematic region the χ^2 and the pulls distributions are also presented (except for the "all candidates" case, since they have been already shown in Sect. 4.1.)

4.3.1 All candidates

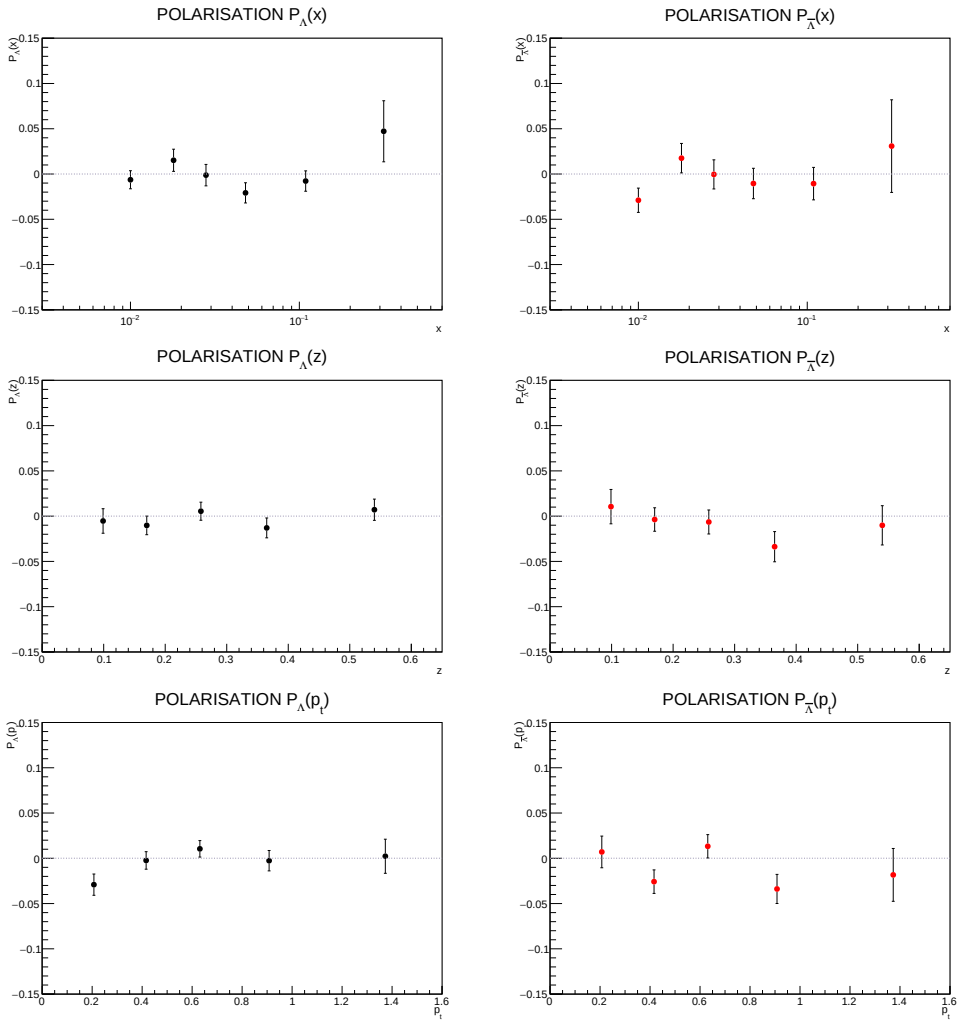

Figure 4.5 Measured polarisations as function of x, z and p_t for Λs (on the left, black points) and for $\bar{\Lambda}$s (on the right, red points). All candidates considered.

As can be seen in Fig. 4.5, the measured polarisations are generally compatible with zero. The two most interesting points are the last value of $P_\Lambda(x)$ and the first of $P_\Lambda(p_t)$. The former, even with a large statistical error, is different from zero and could be a hint of a transversity signal, that is known to differ from zero for u (and d) quarks at large x. The latter point, namely $P_\Lambda(p_t)$ with $p_t \sim 0.2$ GeV/c, is unexpectedly different from zero, even if the expression for P_Λ is not an explicit function of p_t. It is important to stress, however, that the small p_t approximation (collinearity case) is the framework in which the calculations for the Λ transverse polarisation are performed.

The measured polarisations have been then investigated in the high z and low z regions (Fig. 4.6 and Fig. 4.7), trying to separate the different contributions of current and target fragmentation. If the value of $P_\Lambda(x)$, with $x \sim 0.3$ is a transversity signal, then it should be visible also in the region at high z. As a counterpart, however, the selection of a certain kinematic region can enhance the statistical error on the considered quantities.

Also a cut on x has been done (Fig. 4.8 and Fig. 4.9): for $x > 0.032$, if the polarised fragmentation function is different from zero, then a dependence on z of the measured polarisation gives a constraint on the values assumed by the polarised fragmentation function $H_1^{\Lambda/q}$.

Finally, a cut on the low and high p_t regions is appropriate to further investigate possible correlation of the interesting first point in the values of P_Λ vs p_t ($p_t \sim 0.2$ GeV/c) with the other kinematic variables at play.

Unfortunately, when selecting the current fragmentation region the most interesting points turn compatible with zero: the increase of statistical errors is larger than the increase of a (possible) underlying physical signal.

4.3.2 High z region

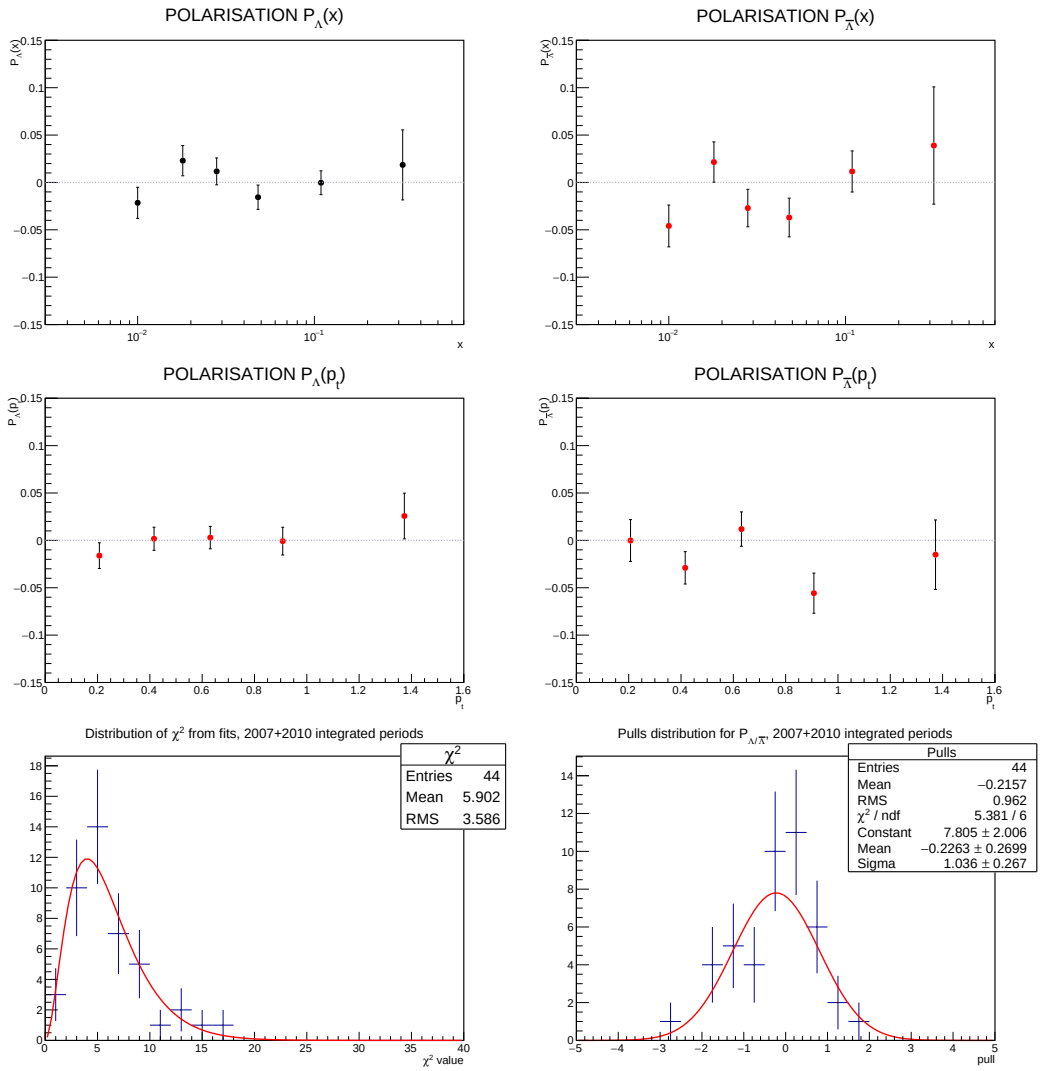

Figure 4.6 Measured polarisations as function of x and p_t for Λs (on the left, black points) and for $\bar{\Lambda}$s (on the right, red points). High z region considered. The distribution of the χ^2 values from fit and the pulls distribution are also reported (bottom row).

4.3.3 Low z region

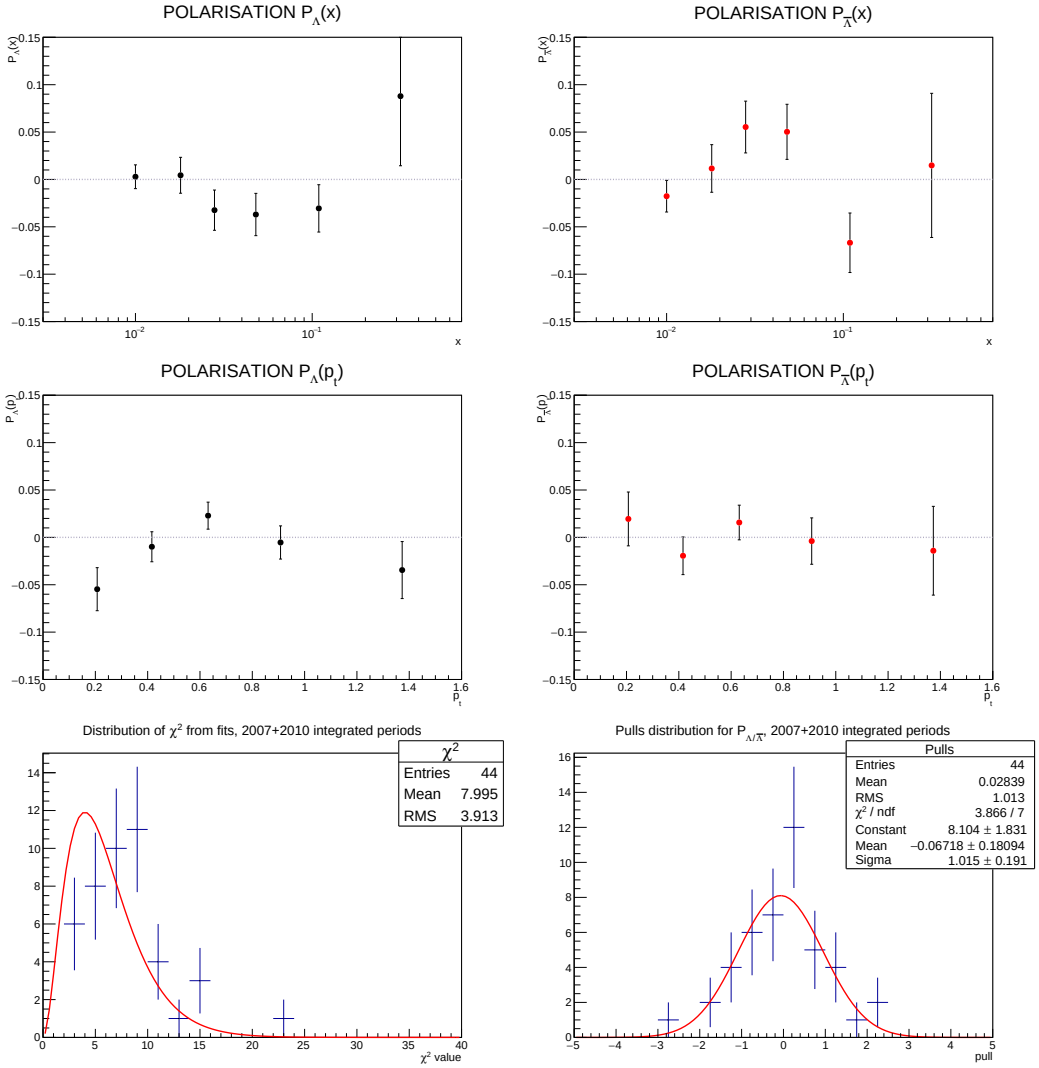

Figure 4.7 Measured polarisations as function of x and p_t for Λs (on the left, black points) and for $\bar{\Lambda}$s (on the right, red points). Low z region considered. The distribution of the χ^2 values from fit and the pulls distribution are also reported (bottom row).

4.3.4 High x region

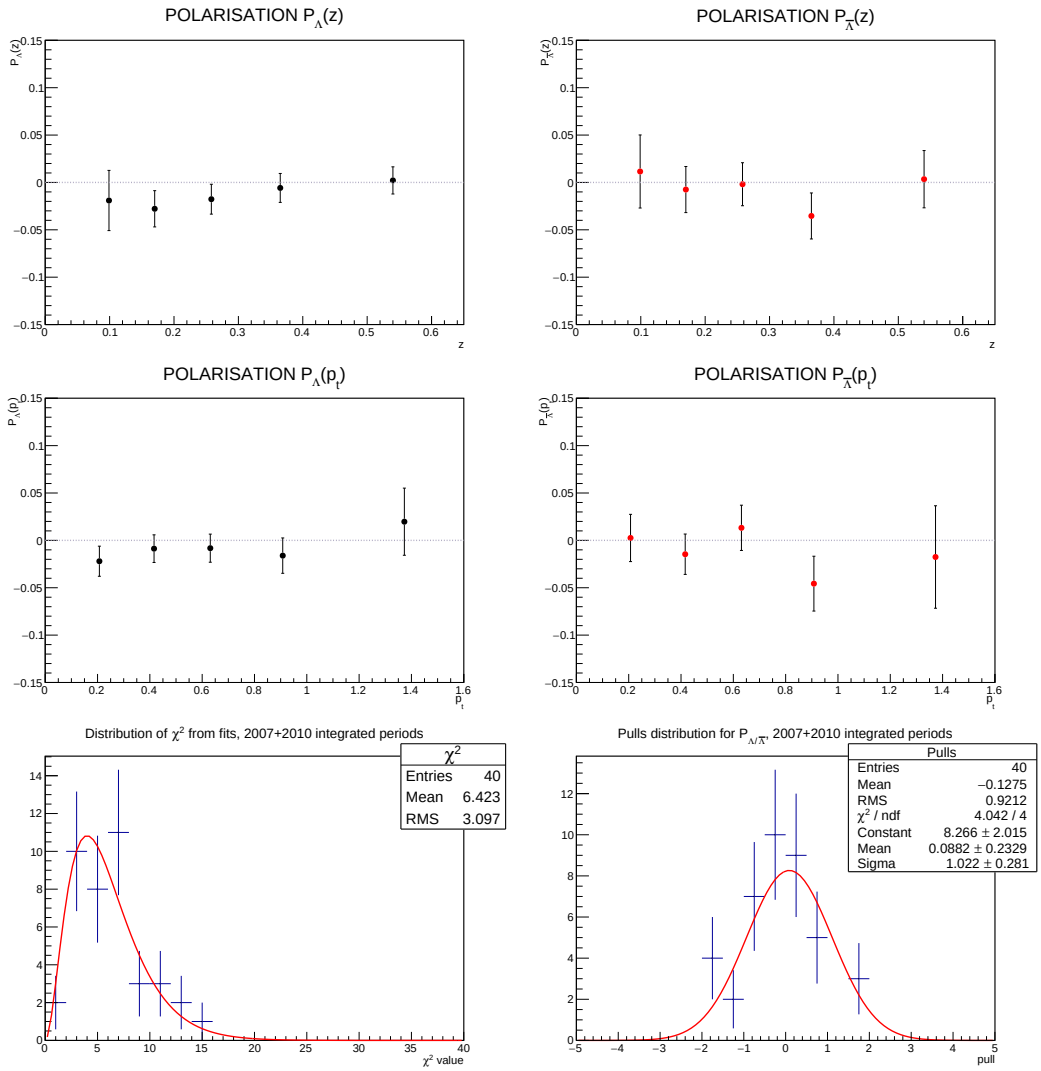

Figure 4.8 Measured polarisations as function of z and p_t for Λs (on the left, black points) and for $\bar{\Lambda}$s (on the right, red points). High x region considered. The distribution of the χ^2 values from fit and the pulls distribution are also reported (bottom row).

4.3.5 Low x region

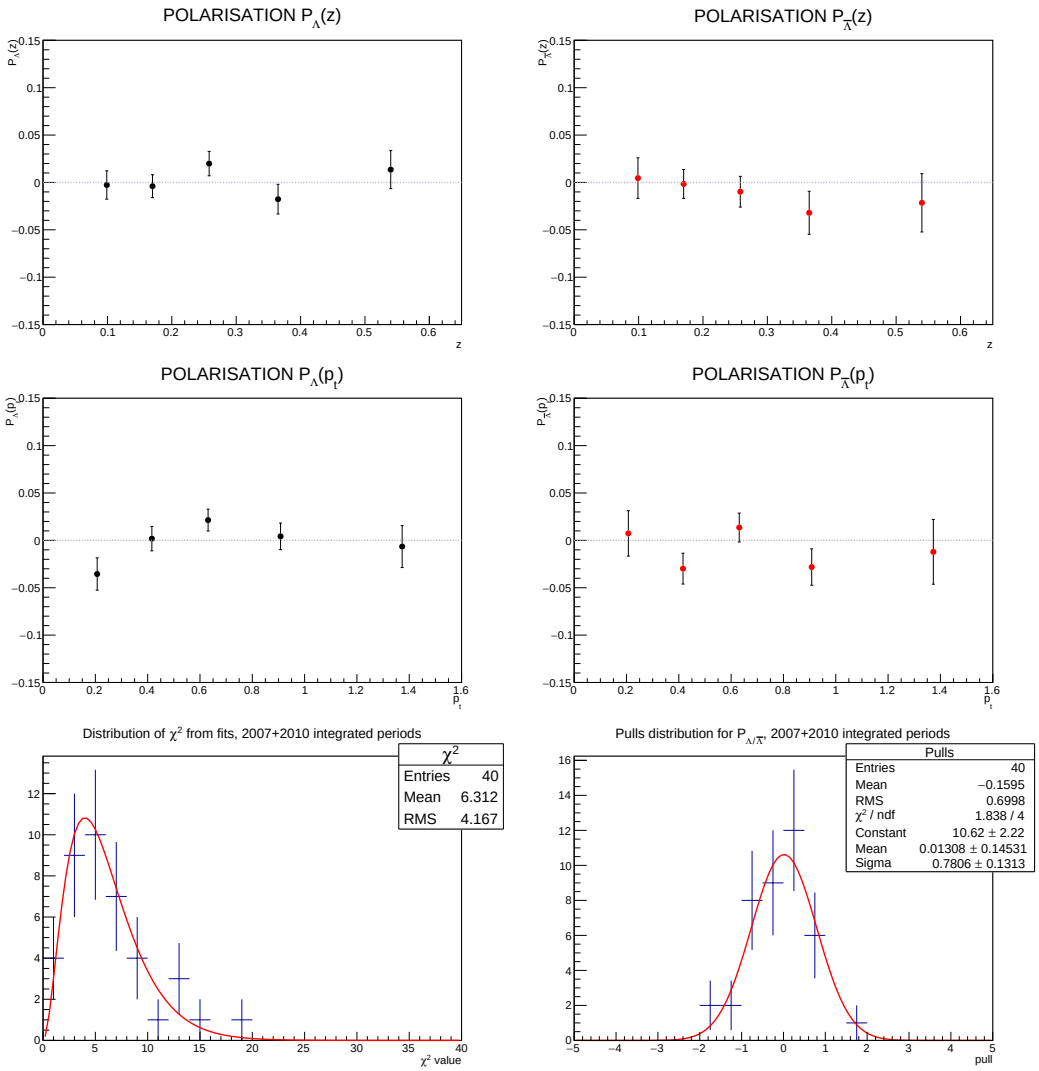

Figure 4.9 Measured polarisations as function of z and p_t for Λs (on the left, black points) and for $\bar{\Lambda}$s (on the right, red points). Low x region considered. The distribution of the χ^2 values from fit and the pulls distribution are also reported (bottom row).

4.3.6 High p_t region

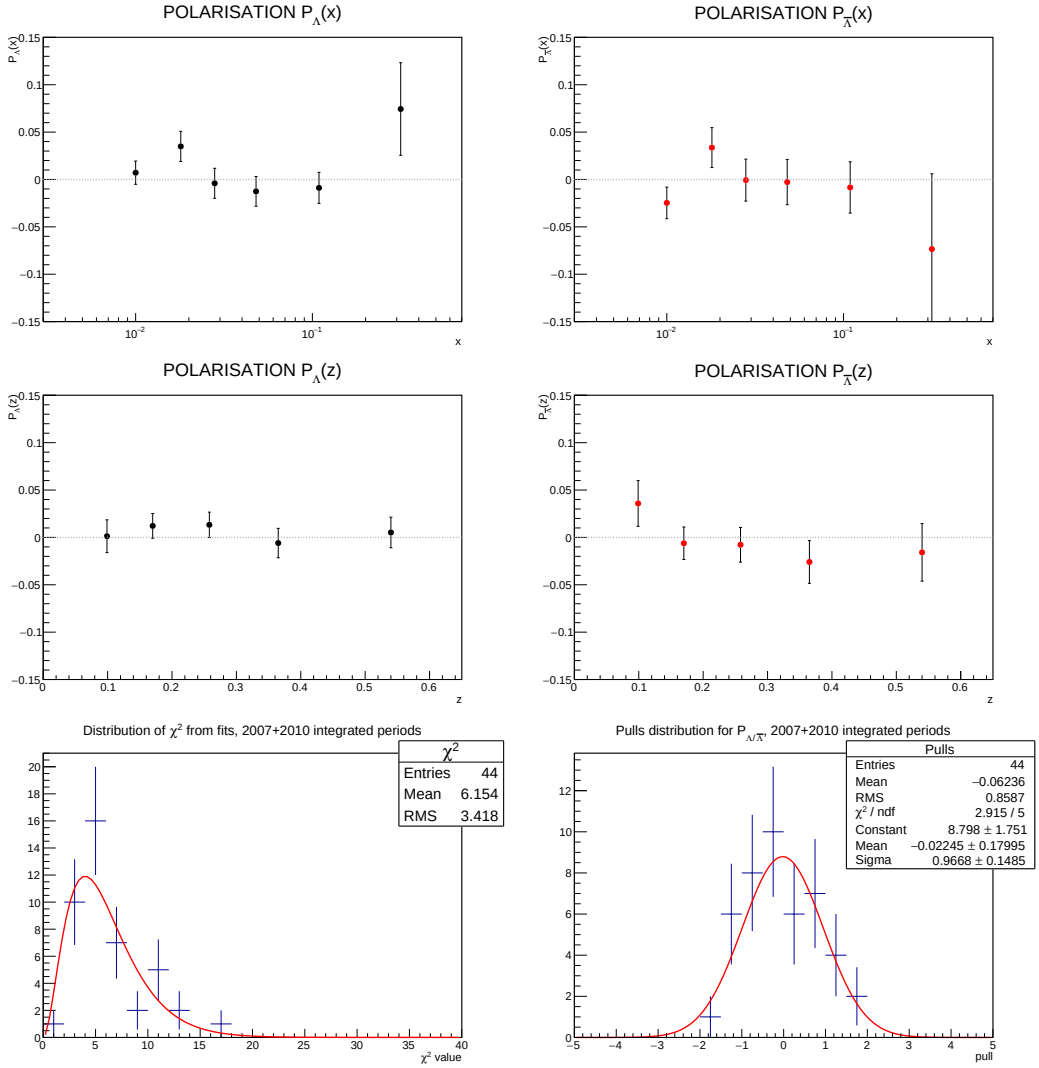

Figure 4.10 Measured polarisations as function of x and z for Λs (on the left, black points) and for $\bar{\Lambda}$s (on the right, red points). High p_t region considered. The distribution of the χ^2 values from fit and the pulls distribution are also reported (bottom row).

4.3.7 Low p_t region

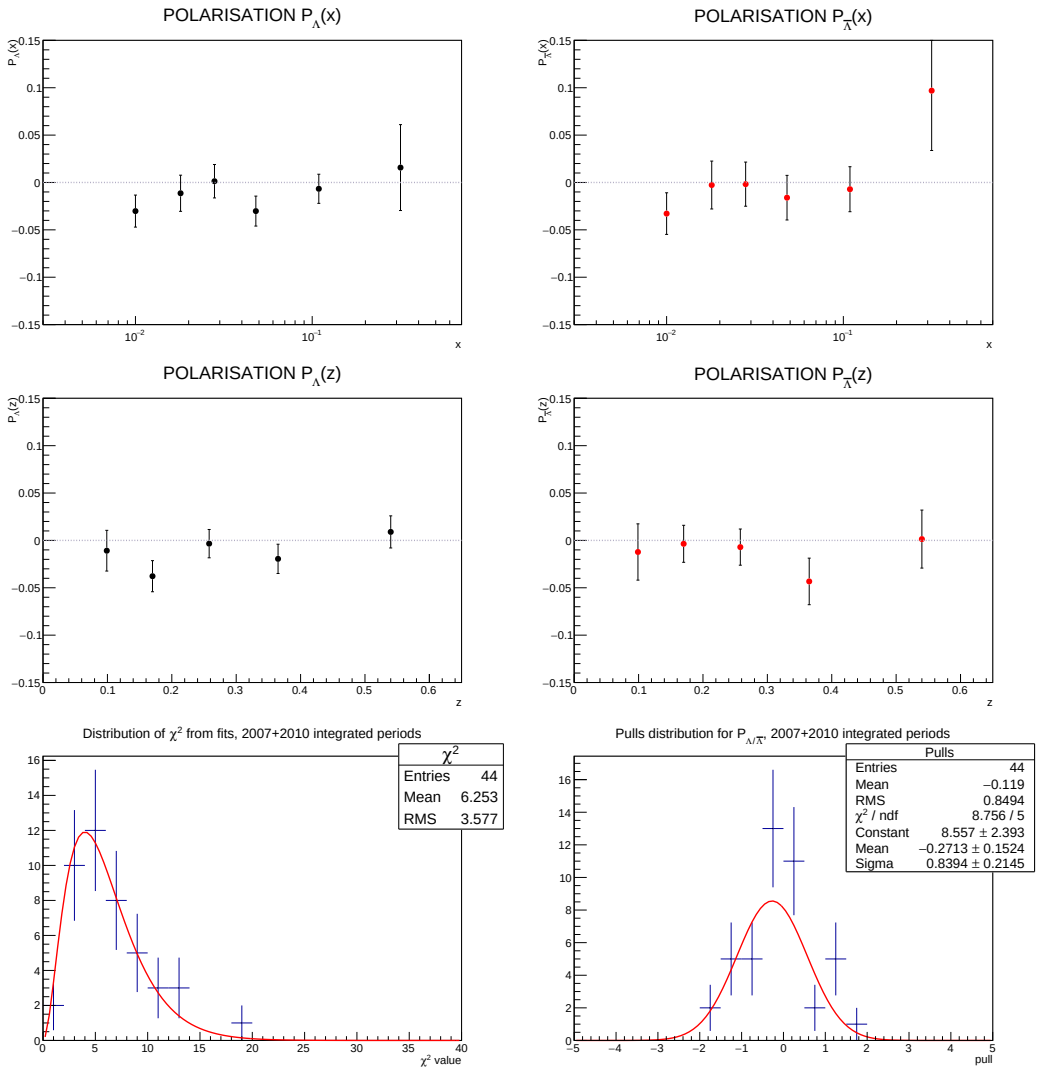

Figure 4.11 Measured polarisations as function of x and z for Λs (on the left, black points) and for $\bar{\Lambda}$s (on the right, red points). Low p_t region considered. The distribution of the χ^2 values from fit and the pulls distribution are also reported (bottom row).

4.4 Extraction of integrated fragmentation functions

The measured polarisations, interesting by themselves, can be corrected to get information on the Λ fragmentation function $H_1^{\Lambda/q}(z)$, so far unknown. Recalling that the expression for the Λ *transversity transmitted* polarisation is:

$$P_\Lambda(x,z) = f P_T D_{NN} \frac{\sum_q e_q^2 h_1^q(x) H_1^{\Lambda/q}(z)}{\sum_q e_q^2 f_1^q(x) D_1^{\Lambda/q}(z)} \tag{4.2}$$

we see that, dividing for the factors f, P_T and D_{NN}, the remaining term only contain distribution and fragmentation functions. Let's indicate with P_Λ^c the corrected Λ polarisation, also called *spin transfer* to transversely polarised Λs:

$$P_\Lambda^c(x,z) = \frac{P_\Lambda(x,z)}{f P_T D_{NN}} = \frac{\sum_q e_q^2 h_1^q(x) H_1^{\Lambda/q}(z)}{\sum_q e_q^2 f_1^q(x) D_1^{\Lambda/q}(z)}. \tag{4.3}$$

Assuming that the distribution functions are dominated by the u quark contribution, then the sum over the quark flavors can be written as :

$$P_\Lambda^c(x,z) = \frac{4h_1^u(x)H_1^{\Lambda/u}(z) + h_1^d(x)H_1^{\Lambda/d}(z)}{4f_1^u(x)D_1^{\Lambda/u}(z) + f_1^d(x)D_1^{\Lambda/d}(z)} \sim \frac{h_1^u(x)}{f_1^u(x)} \frac{H_1^{\Lambda/u}(z)}{D_1^{\Lambda/u}(z)} \tag{4.4}$$

This is an important point, since (as explained in Sect. 1.4) the ratio $h_1^u(x)/f_1^u(x)$ is by now known.

In this framework, the observation of $P_\Lambda^c(x)$, implying an integration over z, gives direct access to the ratio of the z-integrated fragmentation functions:

$$P_\Lambda^c(x) = \frac{h_1^u(x)}{f_1^u(x)} \frac{\int dz H_1^{\Lambda/u}(z)}{\int dz D_1^{\Lambda/u}(z)}. \tag{4.5}$$

The measured values are shown in Fig. 4.12.

We have used the results shown in Fig. 1.7 for $h_1^u(x)$ and the result of the CTEQ5D for the unpolarised PDF $f_1^u(x)$, obtaining the values of $h_1^u(x)/f_1^u(x)$ shown in Fig. 4.13.

By fitting those values with the function $Ax(1-x)^B$ we obtained: $A = 2.52 \pm 0.70$ and $B = 2.5 \pm 1.5$. The values of $P_\Lambda^c(x)$ have been fitted with the function:

$$kAx(1-x)^B \tag{4.6}$$

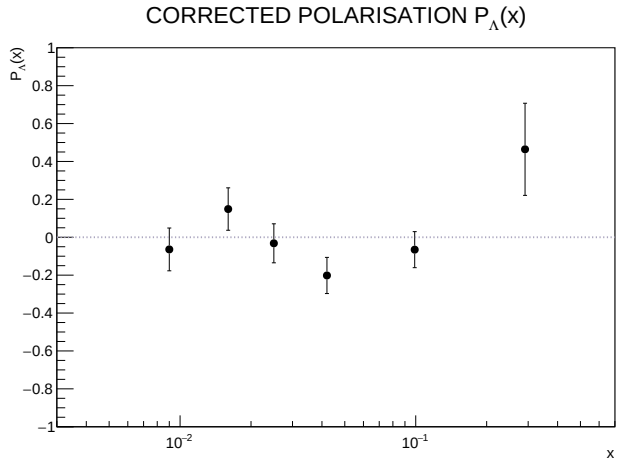

Figure 4.12 Corrected polarisations as function of x for Λs (all candidates)

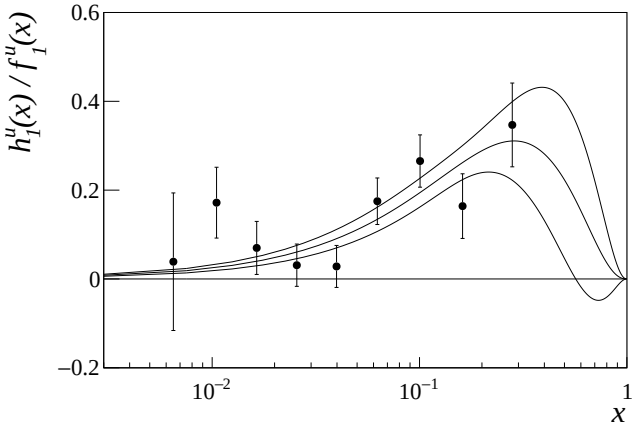

Figure 4.13 The $h_1^u(x)/f_1^u(x)$ ratio, fitted with a function of the form $Ax(1-x)^B$. The central line is the fitted curve, the two lateral ones fix a $\pm 1\sigma$ interval.

with $A = 2.52$, $B = 2.5$ and k free parameter. The result, shown in Fig. 4.14, gives the ratio of the two z-integrated fragmentation functions:

$$\hat{k} = \frac{\int dz H_1^{\Lambda/u}(z)}{\int dz D_1^{\Lambda/u}(z)} = -0.22 \pm 0.38. \tag{4.7}$$

The obtained value is small, in agreement with the predictions quoted in Sect. 4.1. The statistical error is large, as expected. It has to be stressed that this is the first measurement of the unknown fragmentation function $H_1^{\Lambda/q}$ and we consider it an important result which contributes to our knowledge of the Λ structure.

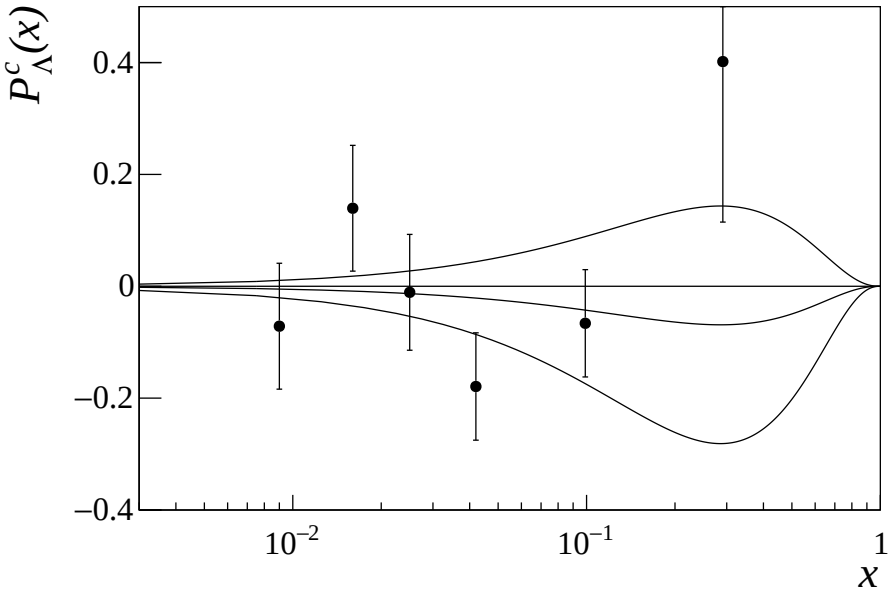

Figure 4.14 Corrected polarisation (all candidates) with the fitted function (see text).

4.5 Conclusions and outlook

In this thesis, the polarisation transfer from a transversely polarised proton target to Λ hyperons in SIDIS has been measured using COMPASS data collected with a muon beam of 160 GeV/c.

The Λ and $\bar{\Lambda}$ transversity transmitted polarisation has been measured along the axis given by the outgoing quark spin vector. This observable gives access to the new transversity parton distribution h_1^q times the still completely unknown fragmentation function $H_1^{\Lambda/q}$.

For the first time, both the 2007 and 2010 COMPASS data, collected with a transversely polarised proton target, have been used. The selection of Λ and $\bar{\Lambda}$ candidates has been performed in a number of steps. First of all, DIS events are selected. Then, background events are removed with suitable kinematic cuts. The RICH detector has been used to reject all the particles falsely assumed to be the Λ ($\bar{\Lambda}$) decay proton (antiproton). The Armenteros plot has allowed to identify the interesting V^0 candidates. A mass cut, to select all the candidates inside the Λ invariant mass peak, has been the last step of the selection procedure. The (small) background contribution has been evaluated with the sideband method.

The angular distribution of the decay p ($\bar{p}$) has been measured in the Λ ($\bar{\Lambda}$) rest frame. The new method for the polarisation extraction has taken care of the possible systematic effects due to spectrometer acceptance introducing a quantity, the *double ratio*, that analytically removes them under minimal and reasonable assumptions on the spectrometer performance.

The polarisations, measured in seven kinematic regions, are generally compatible with zero. Nevertheless, an interesting result has been obtained for the first time for the ratio of the z-integrated fragmentation functions $H_1^{\Lambda/q}$ and $D_1^{\Lambda/q}$, once the measured polarisations had been corrected for the dilution factor, the polarisation of the target and the depolarisation factor.

Despite the fact that all the COMPASS data, namely all the existing data in the world suitable for this measurement, have been used, the statistical uncertainty on the measured polarisations is still large. On the other hand, even if the transverse polarisation transfer from the u-quark to the Λ has been measured to be too small to allow for a study of transversity in this channel, its measurement will give relevant information on the hadron structure.

Acknowledgements

Working on this thesis has been a great experience and a real occasion of personal growth. I would like to thank those people who made this thesis possible and that hanged around with me along this path.

First and foremost I am very grateful to my supervisor, Prof. Anna Martin, for the opportunity she gave me to work on such an interesting subject, doing research at the forefront. She taught me a method and suggested the correct way of looking at things, whilst allowing me the room to work in my own way. Thank you. This work would not have been (literally) possible without the support and encouragement of my co-supervisor, Giulio Sbrizzai. He has been abundantly helpful in many ways, mostly for what concerns programming but not only, and I deeply thank him for his presence during the past months. Special thanks are due to all members of the Trieste COMPASS group: in particular Prof. Franco Bradamante, Prof. Andrea Bressan, Adam, Albi and all the others. Anyone of you, with a simple encouragement, a discussion, a suggestion, a pat on the back, a proposal for a coffee, has contributed to this work. Thank you, you have been precious to me. I would like to show my gratitude to Prof. Rainer Joosten from the Bonn COMPASS group for his contribution to the cross-check. I really appreciated his professionality and his hability in multi-tasking. I am very grateful to my colleagues of the lab group: Elena and Marco, I am very glad to have you as my friends.

More than anything I would like to thank my family and my longtime friends for their constant encouragement and understanding through the years of my studies. You all made it possible to achieve my aim. Thank you for everything.

Appendix A

2007/2010 results compatibility

Λ polarisation has been extracted using both 2007 and 2010 COMPASS proton data. Here we report, for completeness, the comparison between the results obtained for 2007 and 2010 separately considered as a period ("second strategy"), that have been then combined in a weighted mean to give the final results. 2010 results can be recognised by the smaller error bars (only statistical uncertainty reported).

High z region

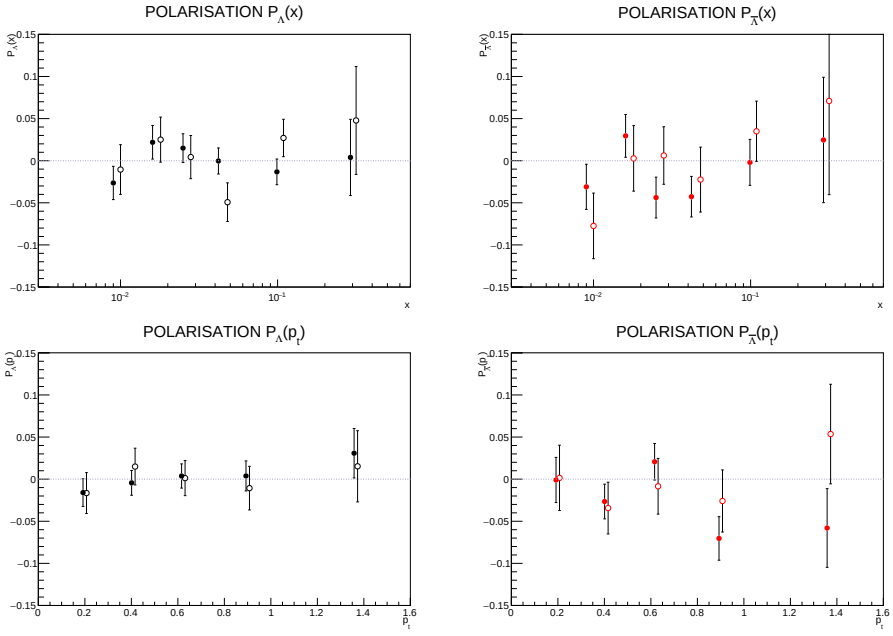

Figure A.1 Comparison between 2007 and 2010 results. High z region considered.

Low z region

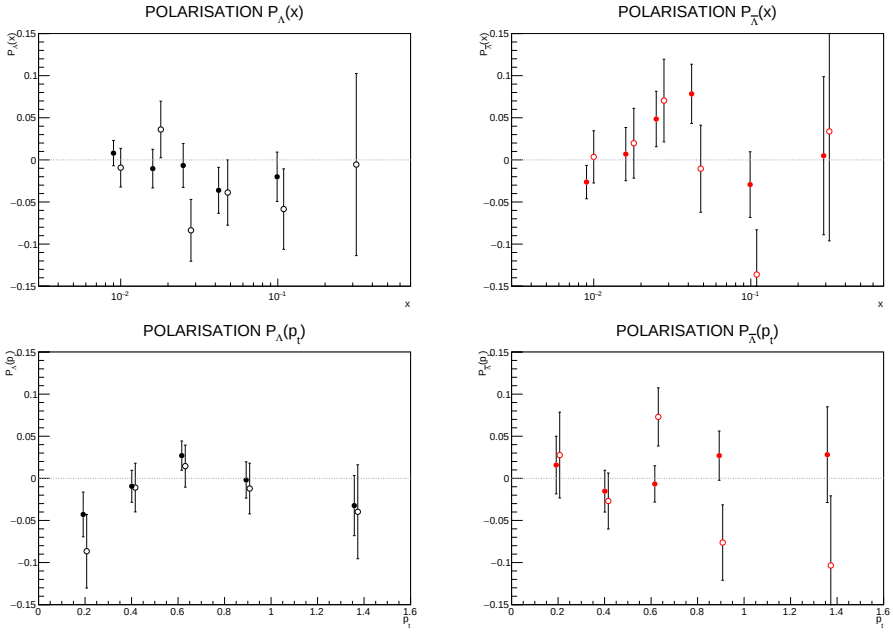

Figure A.2 Comparison between 2007 and 2010 results. Low z region considered.

High x region

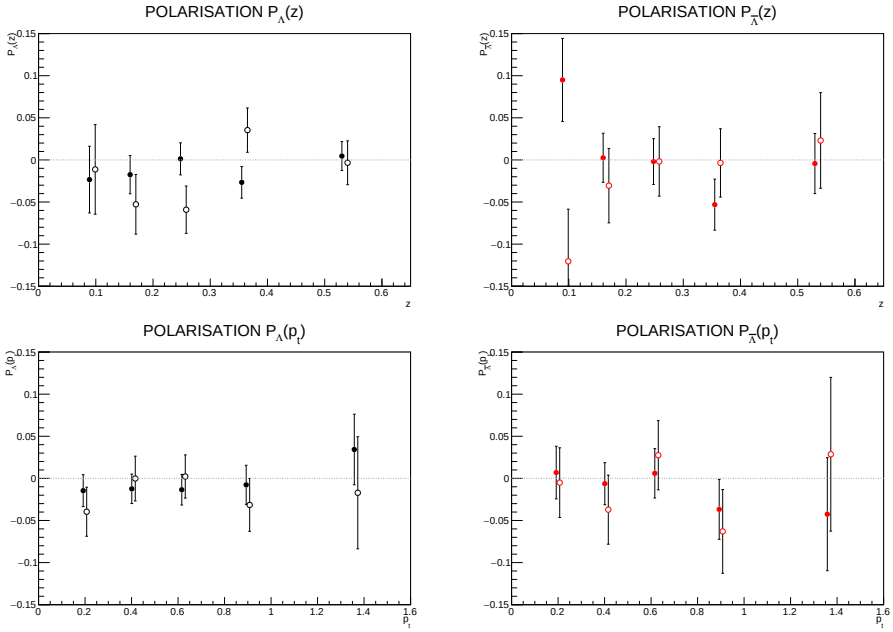

Figure A.3 Comparison between 2007 and 2010 results. High x region considered.

Low x region

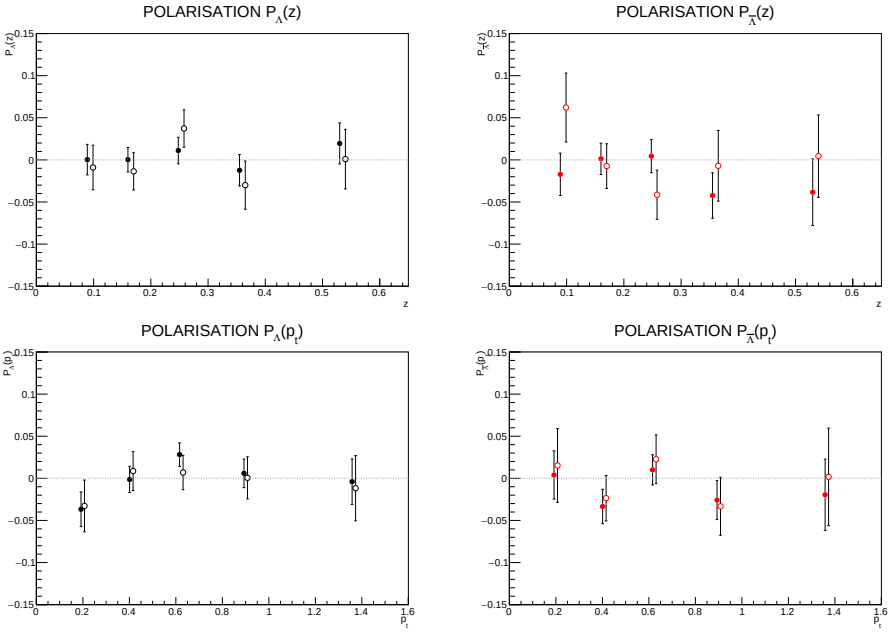

Figure A.4 Comparison between 2007 and 2010 results. Low x region considered.

High p_t region

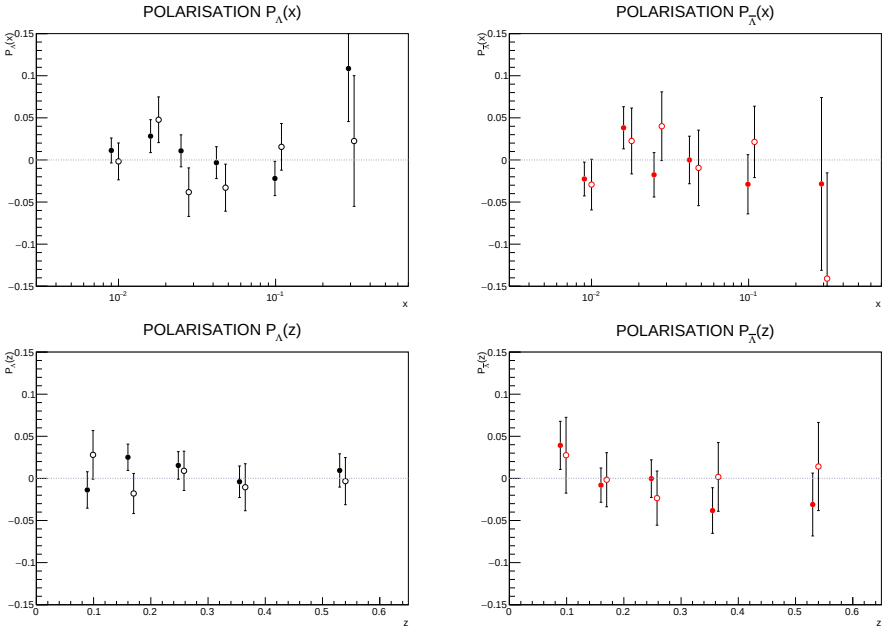

Figure A.5 Comparison between 2007 and 2010 results. High p_t region considered.

Low p_t region

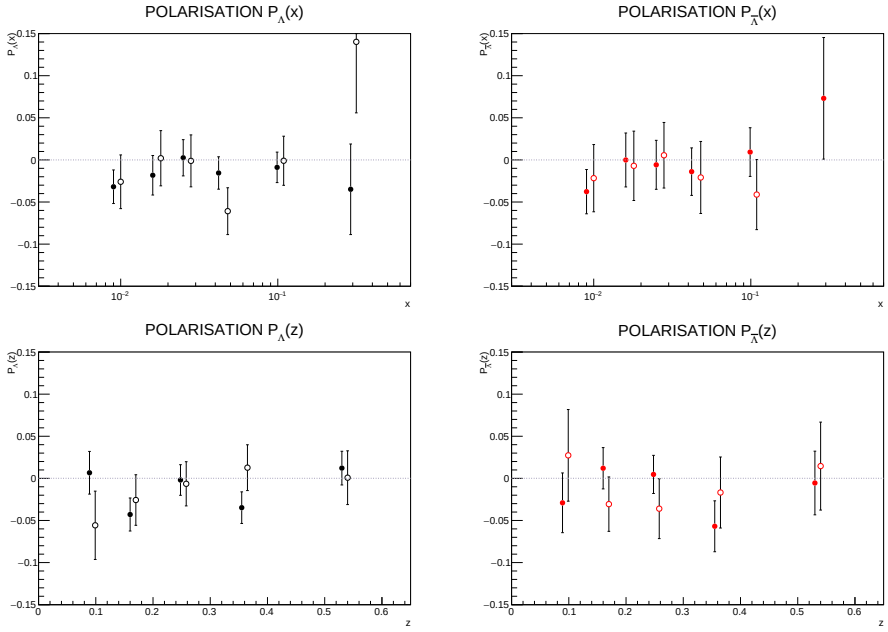

Figure A.6 Comparison between 2007 and 2010 results. High p_t region considered.

All candidates

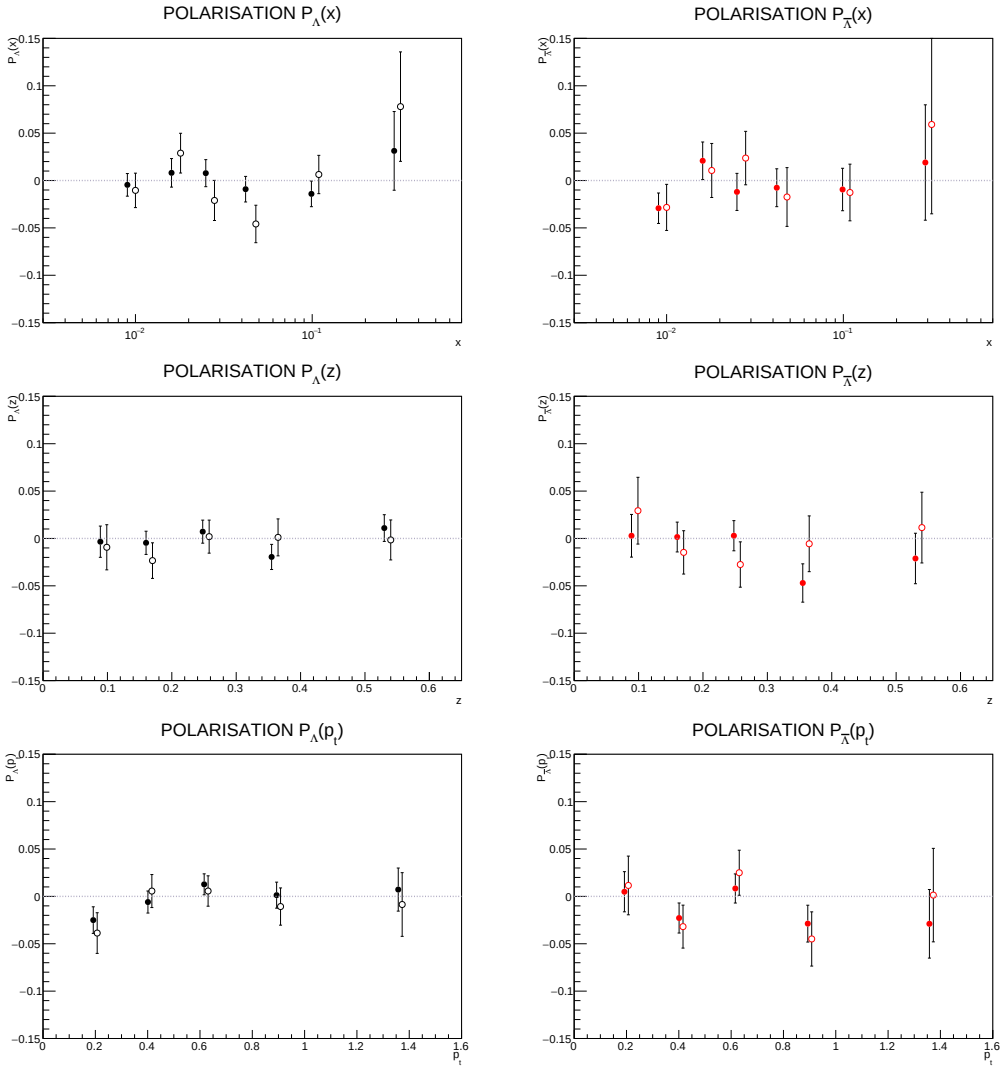

Figure A.7 Comparison between 2007 and 2010 results. All candidates considered.

Bibliography

[1] J. Ashman et al. A Measurement of the Spin Asymmetry and Determination of the Structure Function g(1) in Deep Inelastic Muon-Proton Scattering. *Phys. Lett.*, B206:364, 1988.

[2] J. Ashman et al. An Investigation of the Spin Structure of the Proton in Deep Inelastic Scattering of Polarized Muons on Polarized Protons. *Nucl. Phys.*, B328:1, 1989.

[3] R. L. Jaffe and X. Ji. Chiral odd parton distributions and Drell-Yan processes. *Nucl. Phys.*, B375:527–560, 1992.

[4] G. Bunce et al. Lambda0 Hyperon Polarization in Inclusive Production by 300-GeV Protons on Beryllium. *Phys. Rev. Lett.*, 36:1113–1116, 1976.

[5] G. L. Kane, J. Pumplin, and W. Repko. Transverse quark polarization in large-p_T reactions, e^+e^- jets, and leptoproduction: A test of quantum chromodynamics. *Phys. Rev. Lett.*, 41:1689–1692, Dec 1978.

[6] J. P. Ralston and D. E. Soper. Production of Dimuons from High-Energy Polarized Proton Proton Collisions. *Nucl. Phys.*, B152:109, 1979.

[7] X. Artru and M. Mekhfi. Transversely Polarized Parton Densities, their Evolution and their Measurement. *Z. Phys.*, C45:669, 1990.

[8] J. Soffer. Positivity constraints for spin dependent parton distributions. *Phys. Rev. Lett.*, 74:1292–1294, 1995.

[9] A. Metz and A. Vossen. Parton Fragmentation Functions. *Prog. Part. Nucl. Phys.*, 91:136–202, 2016.

[10] C. Adolph et al. Interplay among transversity induced asymmetries in hadron leptoproduction. *Phys. Lett.*, B753:406–411, 2016.

[11] F. Baldracchini, N. S. Craigie, V. Roberto, and M. Socolovsky. A Survey of Polarization Asymmetries Predicted by QCD. *Fortsch. Phys.*, 30:505–550, 1981.

[12] X. Artru and M. Mekhfi. What can we learn from unpolarized and polarized electroproduction of fast baryons? *Nucl. Phys.*, A532:351–358, 1991.

[13] R. A. Kunne, J. Arvieux, Pierre A. M. Guichon, J. M. Laget, F. Kunne, B. Saghai, X. Artru, R. Frascaria, and M. Morlet. Electroproduction of polarized Lambdas (a proposal for the European Electron Facility). *Italian Phys. Soc. Proc.*, 44:401, 1993.

[14] M. Anselmino. Transversity and Lambda polarization. In *Workshop on Future Physics at COMPASS Geneva, Switzerland, September 26-27, 2002*, 2003.

[15] X. Artru. Short introduction to quark transverse spin. In *QCD and high-energy hadronic interactions. Proceedings, Hadronic Session of the 28th Rencontres de Moriond, Moriond Particle Physics Meeting, Les Arcs, France, March 20-27, 1993*, pages 47–52, 1993.

[16] P. J. Mulders and R. D. Tangerman. The Complete tree level result up to order 1/Q for polarized deep inelastic leptoproduction. *Nucl. Phys.*, B461:197–237, 1996. [Erratum: Nucl. Phys.B484,538(1997)].

[17] E. D. Commins and P. H. Bucksbaum. *Weak interactions of leptons and quarks*. Cambridge University Press, 1983.

[18] K. A. Olive et al. Review of Particle Physics. *Chin. Phys.*, C38:090001, 2014.

[19] D. H. Perkins. *Introduction to high energy physics, 4th ed.* Cambridge University Press, 2000.

[20] V. Abazov et al. A Study of spin-dependent interactions with antiprotons: The Structure of the nucleon. 2004. hep-ex/0507077.

[21] V. Barone et al. Antiproton-proton scattering experiments with polarization. 2005. hep-ex/0505054.

[22] H. Avakian, A. Bressan, and M. Contalbrigo. Experimental results on TMDs. *Eur. Phys. J.*, A52(6):150, 2016. [Erratum: Eur. Phys. J.A52,no.6,165(2016)].

[23] E. S. Ageev et al. A New measurement of the Collins and Sivers asymmetries on a transversely polarised deuteron target. *Nucl. Phys.*, B765:31–70, 2007.

[24] M. Alekseev et al. Collins and Sivers asymmetries for pions and kaons in muon-deuteron DIS. *Phys. Lett.*, B673:127–135, 2009.

[25] C. Adolph et al. Experimental investigation of transverse spin asymmetries in muon-p SIDIS processes: Collins asymmetries. *Phys. Lett.*, B717:376–382, 2012.

[26] C. Adolph et al. Collins and Sivers asymmetries in muonproduction of pions and kaons off transversely polarised protons. *Phys. Lett.*, B744:250–259, 2015.

[27] A. Airapetian et al. Effects of transversity in deep-inelastic scattering by polarized protons. *Phys. Lett.*, B693:11–16, 2010.

[28] Y. Zhang et al. Measurement of pretzelosity asymmetry of charged pion production in Semi-Inclusive Deep Inelastic Scattering on a polarized ^{3}He target. *Phys. Rev.*, C90(5):055209, 2014.

[29] A. Martin, F. Bradamante, and V. Barone. Extracting the transversity distributions from single-hadron and dihadron production. *Phys. Rev.*, D91(1):014034, 2015.

[30] R. Seidl et al. Measurement of Azimuthal Asymmetries in Inclusive Production of Hadron Pairs in e+e- Annihilation at s**(1/2) = 10.58-GeV. *Phys. Rev.*, D78:032011, 2008. [Erratum: Phys. Rev.D86,039905(2012)].

[31] M. Anselmino, M. Boglione, U. D'Alesio, S. Melis, F. Murgia, and A. Prokudin. Simultaneous extraction of transversity and Collins functions from new SIDIS and e+e- data. *Phys. Rev.*, D87:094019, 2013.

[32] A. Ferrero. Measurement of transverse Lambda and Antilambda polarization at COMPASS. *AIP Conf. Proc.*, 915:436–440, 2007.

[33] T. Negrini. Lambda polarization with a transversely polarized proton target at the COMPASS experiment. *AIP Conf. Proc.*, 1149:656–659, 2009.

[34] M. Anselmino, M. Boglione, and F. Murgia. Lambda and anti-Lambda polarization in polarized DIS. *Phys. Lett.*, B481:253–262, 2000.

[35] J.-J. Yang. q —> Lambda fragmentation function and nucleon transversity distribution in a diquark model. *Nucl. Phys.*, A699:562–578, 2002.

[36] P. Abbon et al. The COMPASS experiment at CERN. *Nucl. Instrum. Meth.*, A577:455–518, 2007.

[37] The COMPASS collaboration. A proposal for a common muon and proton apparatus for structure and spectroscopy. *CERN SPSLC-96-14*, 1996.

[38] A. Abragam and M. Goldman. Principles of dynamic nuclear polarisation. *Reports on Progress in Physics*, 41(3):395, 1978.

[39] K. Kondo et al. Polarization measurement in the COMPASS polarized target. *Nucl. Instrum. Meth.*, A526:70–75, 2004.

[40] C. Bernet et al. The 40-cm x 40-cm gaseous microstrip detector Micromegas for the high-luminosity COMPASS experiment at CERN. *Nucl. Instrum. Meth.*, A536:61–69, 2005.

[41] M. C. Altunbas et al. Construction, test and commissioning of the triple-GEM tracking detector for COMPASS. *Nucl. Instrum. Meth.*, A490:177–203, 2002.

[42] S. Panebianco. Performances of drift chambers and micromegas in 2003. *COMPASS Collaboration Meeting*, 2003.

[43] V. N. Bychkov et al. The large size straw drift chambers of the COMPASS experiment. *Nucl. Instrum. Meth.*, A556:66–79, 2006.

[44] A. Amoroso et al. The front-end electronics for the COMPASS MWPCs. *Nucl. Instrum. Meth.*, A518:495–497, 2004.

[45] P. Abbon et al. Particle identification with COMPASS RICH-1. *Nucl. Instrum. Meth.*, A631:26–39, 2011.

[46] P. A. Čerenkov. Visible radiation produced by electrons moving in a medium with velocities exceeding that of light. *Phys. Rev.*, 52:378–379, Aug 1937.

[47] E. Albrecht et al. The radiator gas and the gas system of COMPASS RICH-1. *Nucl. Instrum. Meth.*, A502:266–269, 2003.

[48] J. Barth, J. Bernhard, et al. Trigger Configuration Summary 2002-2012. *COMPASS NOTE 2016-04*, 2016.

[49] H. Fischer et al. The COMPASS data acquisition system. *IEEE Trans. Nucl. Sci.*, 49:443–447, 2002.

[50] C. Adolph and R. Joosten. Collins and Sivers asymmetries for K0 from the 2007 and 2010 transversely polarized proton data. *COMPASS Note Nov. 2013*, 2013.

[51] J. Podolanski and R. Armenteros. III. analysis of V-events. *The London, Edinburgh, and Dublin Philosophical Magazine and Journal of Science*, 45(360):13–30, 1954.

[52] R Armenteros, K.H. Barker, C.C. Butler, A. Cachon, and C.M. York. Lvi. the properties of charged v-particles. *The London, Edinburgh, and Dublin Philosophical Magazine and Journal of Science*, 43(341):597–611, 1952.

[53] V. Barone. *Relatività: principi e applicazioni*. Bollati Boringhieri, 2004.